

Lecture Notes on Multidisciplinary Industrial Engineering
Series Editor: J. Paulo Davim

Inderdeep Singh
Pramendra Kumar Bajpai
Kuldeep Panwar *Editors*


Advances in Materials Engineering and Manufacturing Processes

Select Proceedings of ICFTMM 2019

 Springer

Lecture Notes on Multidisciplinary Industrial Engineering

Series Editor

J. Paulo Davim , Department of Mechanical Engineering, University of Aveiro, Aveiro, Portugal

“Lecture Notes on Multidisciplinary Industrial Engineering” publishes special volumes of conferences, workshops and symposia in interdisciplinary topics of interest. Disciplines such as materials science, nanosciences, sustainability science, management sciences, computational sciences, mechanical engineering, industrial engineering, manufacturing, mechatronics, electrical engineering, environmental and civil engineering, chemical engineering, systems engineering and biomedical engineering are covered. Selected and peer-reviewed papers from events in these fields can be considered for publication in this series.

More information about this series at <http://www.springer.com/series/15734>

Inderdeep Singh · Pramendra Kumar Bajpai ·
Kuldeep Panwar
Editors

Advances in Materials Engineering and Manufacturing Processes

Select Proceedings of ICFTMM 2019

 Springer

Editors

Inderdeep Singh
Department of Mechanical
and Industrial Engineering
Indian Institute of Technology Roorkee
Roorkee, Uttarakhand, India

Pramendra Kumar Bajpai
Department of Manufacturing Processes
and Automation Engineering
Netaji Subhas University of Technology
New Delhi, India

Kuldeep Panwar
Department of Mechanical
and Automation Engineering
Delhi Technical Campus
Greater Noida, India

ISSN 2522-5022

ISSN 2522-5030 (electronic)

Lecture Notes on Multidisciplinary Industrial Engineering

ISBN 978-981-15-4330-2

ISBN 978-981-15-4331-9 (eBook)

<https://doi.org/10.1007/978-981-15-4331-9>

© Springer Nature Singapore Pte Ltd. 2020

This work is subject to copyright. All rights are reserved by the Publisher, whether the whole or part of the material is concerned, specifically the rights of translation, reprinting, reuse of illustrations, recitation, broadcasting, reproduction on microfilms or in any other physical way, and transmission or information storage and retrieval, electronic adaptation, computer software, or by similar or dissimilar methodology now known or hereafter developed.

The use of general descriptive names, registered names, trademarks, service marks, etc. in this publication does not imply, even in the absence of a specific statement, that such names are exempt from the relevant protective laws and regulations and therefore free for general use.

The publisher, the authors and the editors are safe to assume that the advice and information in this book are believed to be true and accurate at the date of publication. Neither the publisher nor the authors or the editors give a warranty, expressed or implied, with respect to the material contained herein or for any errors or omissions that may have been made. The publisher remains neutral with regard to jurisdictional claims in published maps and institutional affiliations.

This Springer imprint is published by the registered company Springer Nature Singapore Pte Ltd. The registered company address is: 152 Beach Road, #21-01/04 Gateway East, Singapore 189721, Singapore

Preface

The book *Advances in Materials Engineering and Manufacturing Processes* covers a variety of topics from diverse fields of material and manufacturing. The content of this edited book is based on the papers presented at the 2nd International Conference on Futuristic Trends in Materials and Manufacturing (ICFTMM 2019) held in Delhi Technical Campus, 28/1, Knowledge Park-III, Greater Noida, Uttar Pradesh-201306, India, on 8–9 November 2019. As a result of economic globalization, manufacturing enterprises face intense competition for market, resource, technology and skilled personnel. The design and manufacturing of the product are becoming more and more complex. In this environment, manufacturing enterprises are seeking various integrated, just-in-time, manufacturing resources to meet the requirement of businesses and develop extensive collaboration among enterprises to cope with the rapidly changing market requirements. There are different kinds of manufacturing resources that belong to various enterprises. These enterprises are geographically distributed, morphologically diverse and autonomous, which make the resource sharing and management more complicated. This book covers in depth the manufacturing and various characterizations of different advanced materials. The domain of this book is suitable for the undergraduate and postgraduate students, academicians, scientists and researchers working in this field.

Roorkee, India
New Delhi, India
Greater Noida, India

Inderdeep Singh
Pramendra Kumar Bajpai
Kuldeep Panwar

Contents

1 FEM Analysis of Journal Bearing Based on Feeding of Lubricant	1
Abhinav Maurya and Aman Dev Punia	
2 Design and Analysis of Composite and Al Alloy Wheel Rim	15
Pankaj Singh Bisht and Ankita Awasthi	
3 A Critical Review of Process Parameters in Laminated Object Manufacturing Process	31
Rishabh Gupta, Manish Dalakoti, and Andriya Narasimhulu	
4 Performance Analysis of CI Engine Powered with <i>Simarouba Glauca</i> L. Biodiesel Fuel	41
A. Verma, K. S. Rawat, M. Saify, A. K. Singh, and P. Maheshwari	
5 Wear Characteristics of Silica-Reinforced Rice Husk-Epoxy Hybrid Bio-composite	51
Neeraj Bisht and P. C. Gope	
6 Numerical Analysis of Thermo-Physical Properties Using Disc Blade Inserts with Al_2O_3/TiO_2 Water-Based Nanofluids	59
Jaspreet Kaur and Satyendra Singh	
7 DC Electrical Conductivity and Magnetic Behaviour of Epoxy Matrix Composites Impregnated with Surface-Modified Ferrite Nanoparticles	69
Ashtosh Kumar Singh, M. G. H. Zaidi, and Rakesh Saxena	
8 A Review on Coating for Hydro-turbine Application by HVOF Process	79
Mohit Vishnoi, Paras Kumar, and Qasim Murtaza	

9	An Investigation of Cutting Parameters and Its Effects on Surface Roughness in High-Speed Turning of 52100 Bearing Steel	105
	Rahul Kshetri, Shivasheesh Kaushik, Vinay Sati, Kuldeep Panwar, and Ajay	
10	Calculation for the Output of Solar Still of an Individual Hour . . .	117
	Mohd Zaheen Khan, Etkaf Hasan Khan, Nitesh Agarhari, Mohd Atif Wahid, and I. Nawaz	
11	Effects of Secondary Parallel Cracks on the Fracture Parameters in a Rectangular Plate Under Static Loading	131
	Gulfam Akhtar Ansari and Neeraj Bisht	
12	Flow Analysis of Flue Gas and Effectiveness of Regenerator Using Simulation in Packed Bed Regenerator	137
	Kuldeep Rawat and Vivek Sachan	

About the Editors

Dr. Inderdeep Singh completed his Bachelor of Technology (Mechanical Engineering) in 1998 from the National Institute of Technology Hamirpur with Honors. He completed his Master's and Ph.D. from the department of Mechanical Engineering, Indian Institute of Technology Delhi in 2000 and 2004, respectively. His doctoral research work was awarded by the Foundation for Innovation and Technology Transfer (FITT) as the 'Best Industry Relevant Ph.D. Project' during the session 2004-05. Dr. Singh is currently an Associate Professor in the Department of Mechanical and Industrial Engineering, Indian Institute of Technology (IIT) Roorkee. He has published more than 180 articles in international and national journals and conferences. He has authored a book titled Primary and Secondary Manufacturing of Polymer Matrix Composites and has also contributed 15 book chapters in the broad area of composite materials. His current research focus is towards developing fully biodegradable green composites.

Dr. Pramendra Kumar Bajpai is an Assistant Professor in the division of Manufacturing Processes and Automation Engineering at Netaji Subhas University of Technology, New Delhi. He completed his Ph.D. from the department of Mechanical and Industrial Engineering, Indian Institute of Technology, Roorkee. His research areas include processing of polymer composites and green composites, machining aspects of composites, and FEM modeling of composites. He has published several research articles in journals of repute. He is currently working as an editor of two contributed volumes on processing of polymer composites.

Dr. Kuldeep Panwar is currently working as an Associate Professor & Head of Mechanical and Automation Engineering at Delhi Technical Campus, Greater Noida. He completed his Bachelor's degree in Engineering from B.T.K.I.T, Dwarahat in 2009 and his Master's in Thermal Engineering in 2012. He completed his Ph.D. in Mechanical Engineering from G. B. Pant University of Agriculture and Technology, Pantnagar in 2016. His doctoral research area was analysis of thermal

and resistance characteristics of fixed-bed regenerator with small D/d_p ratio. He has published more than 30 research articles in peer-reviewed international journals and conferences. He has one design patent to his credit.

Chapter 1

FEM Analysis of Journal Bearing Based on Feeding of Lubricant



Abhinav Maurya and Aman Dev Punia

Abstract This paper aims at the FEM analysis of a hydrodynamic journal bearing for the entry of lubricant from two different interfaces: (i) from the mid-section of bearing and (ii) inlet from one side end and exit from another end. The lubricating fluid regime is solved for the pressure distribution for aforementioned and for various length-to-diameter ratios of the bearing. In first case, mid-section is the fluid inlet, and end walls of bearing were taken as outlet. For second case, one end is the fluid inlet and another end was taken as outlet. In the analysis, results were obtained for pressure distribution (for various L/D ratios), total deformation, strain energy, equivalent (von Mises) stress and equivalent strain for both cases.

Keywords Hydrodynamic journal bearing · FEM analysis · Stribeck curve · Reynolds equation

1.1 Introduction

Bearings are the stationary machine elements which are primarily used for providing support and secondarily used for reducing friction and easing the motion of the moving machine element(s). Bearings are classified into two categories: (i) sliding contact-type and (ii) rolling contact-type bearings. Hydrodynamic journal bearings are the sleeve bearings (sliding contact type) that operate with hydrodynamic lubrication that separates the shaft (or journal) and bearing.

A hydrodynamic journal bearing (Fig. 1.1) is a sophisticated component due to various parameters that allow its proper functioning. It is known that during start-up, metal-to-metal contact is present between bearing and shaft (or journal) [1].

A. Maurya (✉)

Netaji Subhas Institute of Technology, New Delhi 110078, India
e-mail: abhnmry@gmail.com

A. D. Punia

Delhi Technological University, New Delhi 110042, India
e-mail: a.amandev@gmail.com

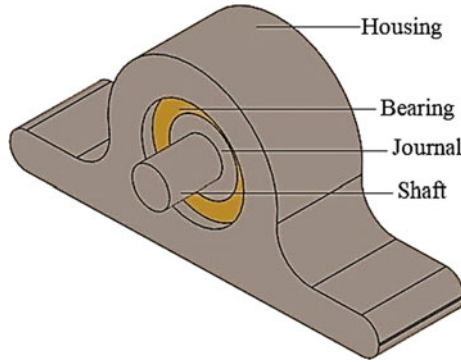


Fig. 1.1 Journal bearing

While during the running condition, fluid film is present between the two moving parts which lifts the shaft by wedging action (Fig. 1.2). To aid calculations and for modelling of hydrodynamic journal bearing, Reynolds equation [2] is generally used.

Reynolds equation:

$$\frac{\partial}{\partial x} \left(\frac{h^3}{\mu} \frac{\partial p}{\partial x} \right) + \frac{\partial}{\partial z} \left(\frac{h^3}{\mu} \frac{\partial p}{\partial z} \right) = 6U \frac{\partial h}{\partial x} \tag{1.1}$$

Since Reynolds equation cannot be solved exactly, finite element method is used as an alternative to solve it [3]. The two solutions obtained, valid only in the positive pressure region, are Sommerfeld’s solutions (for infinitely long bearing) and Ocvirk’s solutions (for infinitely short bearing) [4].

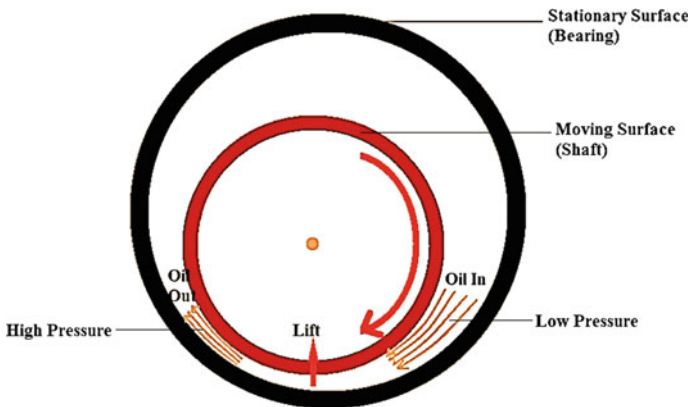


Fig. 1.2 Wedging action

1.2 Methodology

In this paper, lubricating fluid regime is solved for the pressure distribution [5] for different sections of fluid inlet and for various length-to-diameter ratios of the bearing. In one case, mid-section was the fluid inlet, and end walls of bearing were taken as outlet. For second case, one end was taken as the fluid inlet and another end was taken as outlet. Along with these cases, different length-to-diameter ratios are also solved which includes short, square and long bearings.

In this paper, modelling is done for the uniform thickness of the fluid film around the shaft, which is basically the condition at time of steady-state operation where the fluid distribution becomes equal in all directions. It is assumed that the fluid film viscosity remains constant, i.e. it does not vary with the temperature. The bearing load is neglected to calculate the stress, strain and strain energy by applying the effect of fluid pressure contour of bearing. The energy equation is applied, and the regime of flow is assumed to be laminar. ANSYS Fluent was used to obtain the solutions by considering all the assumptions.

1.3 Geometrical Modelling and FEM Analysis

The model constituted an inner cylinder (journal) having radius of 60 mm and another outer cylinder with radius 60.150 (bearing), in between a film thickness of 150 μm . To proceed in the analysis, first a 3D model of bearing was generated in SOLIDWORKS and then imported in ANSYS (Fig. 1.3). It was followed by selection of fluid film to generate mesh on it using the ANSYS 'Fluent' (Fig. 1.4). After geometry, FEM analysis was done by fixing boundary conditions. For first case, the inlet of the lubricant is provided in the mid-section of the bearing, and the outlet is marked at the end of plane surface. For second case, the inlet of the lubricant is provided at one end of the bearing and the outlet at another end of the bearing.

After assignment of the boundary name and types of the flow region, the file is imported to the 'Fluent' software for CFD simulation. In Fluent, the various properties of the lubricating fluid are defined as mentioned in Table 1.1. After running multiple iterations and solving the pressure distribution, the journal bearing is found as pressure contour. These pressure contours are solved for various combinations of length and fluid inlet and are shown in the observations. Similarly, contours were obtained for total deformation, strain energy, equivalent (von Mises) stress and equivalent strain. After the lubricating fluid pressure simulation in the ANSYS 'Fluent', the results and geometry are taken to the static ANSYS analysis for the effect on the bearing. The journal bearing is taken with a thickness of 5 mm. In static analysis, after generating the mesh around the bearing, load was imported from previous contour obtained at the inner surface of cylinder. The solution was then obtained for the equivalent stress, strain, deformation, and strain energy is calculated (Fig. 1.5).

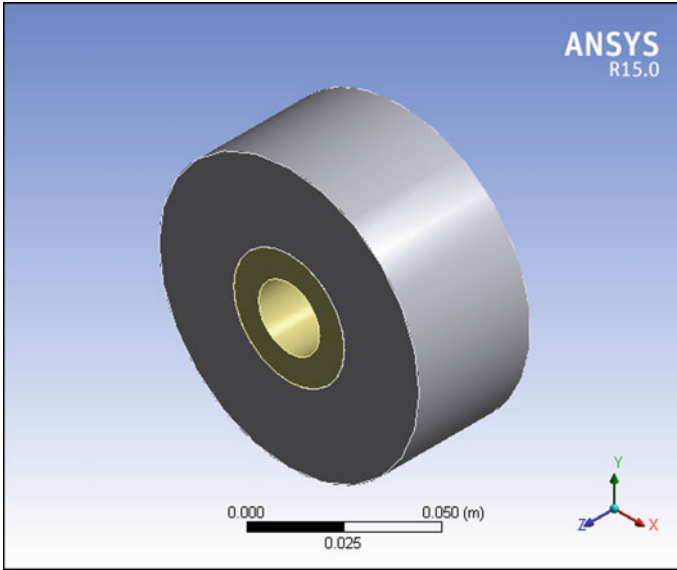


Fig. 1.3 3D model of the journal bearing

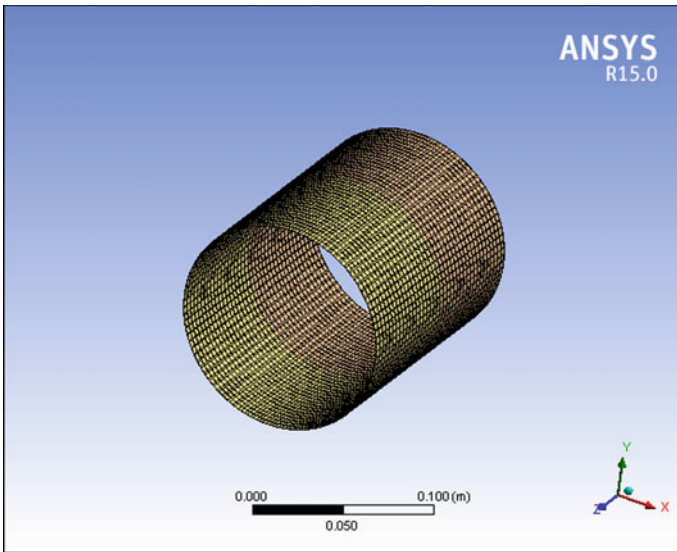


Fig. 1.4 Fluid film lubrication—mesh

Table 1.1 Specification and properties of journal bearing

Parameter	Value
Journal radius R	60 mm
Radial clearance, C	150 μ m
Lubricant viscosity, μ	0.0056 kg/ms
Lubricant density	872 kg/m ³
Lubricant specific heat C_p	1800 J/kgC
Lubricant thermal conductivity	0.135
Bearing thickness, t	5 mm
Lubricant inlet velocity, v	10 m/s
Young's modulus, E	50,000 pa
Poisson's ratio	0.35

1.4 Results and Discussion

After the analysis, results were obtained for various L/D ratios of bearing for mid-section inlet (Case 1) and end-section inlet (Case 2). L/D ratio of 0.75, 1.00 and 1.25 was considered for pressure distribution. However, L/D ratio of 0.75 was considered for total deformation, strain energy, equivalent (von Mises) stress and equivalent strain.

Contours obtained for mid-section inlet (Case 1)

(See Figs. 1.6, 1.7, 1.8, 1.9, 1.10, 1.11 and 1.12).

Contours obtained for end-section inlet (Case 2)

(See Figs. 1.13, 1.14, 1.15, 1.16, 1.17, 1.18 and 1.19).

1.5 Conclusion

1. The maximum pressure was found, as obvious, at the inlet section of the fluid and minimum at the exit section of the fluid.
2. For the same fluid inlet process, the maximum pressure increases as the length of the bearing and by that the length of fluid film increases. In addition, the minimum pressure at the exit of fluid in each case goes on increasing with the increase in length keeping the diameter and other variables constant.
3. For the same conditions in mid-section inlet bearing and end-section inlet bearing, the maximum pressure for each case of various L/D ratios is more in end fluid inlet bearing than the mid-section fluid inlet bearing.
4. The total deformation, strain energy, equivalent (von Mises) stress and equivalent strain in each and every case, irrespective of inlet section, were found to be maximum at the inlet section of the fluid and minimum at the exit section of the bearing.

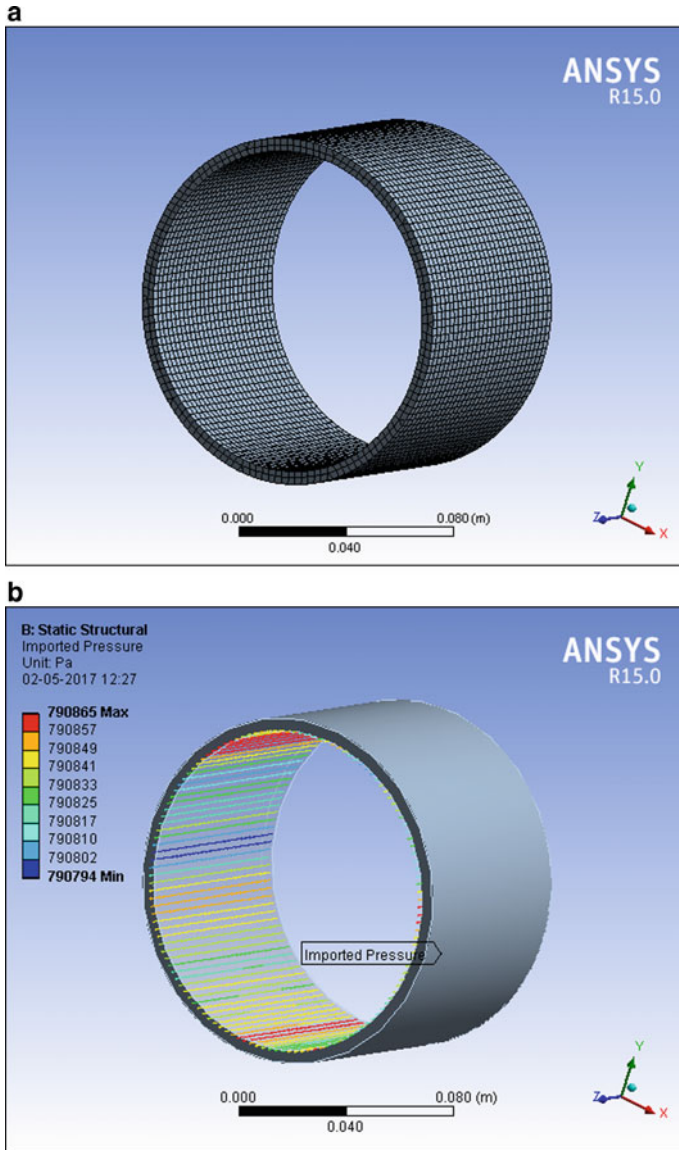


Fig. 1.5 a Bearing mesh. b Imported load on bearing

1.6 Future Scope

It is believed that the experimental analysis can be done based on feeding of lubricant with different groove designs. Additionally, the similar experimental analysis can be performed on bearing with the solid lubrication or nano-lubricant coating.

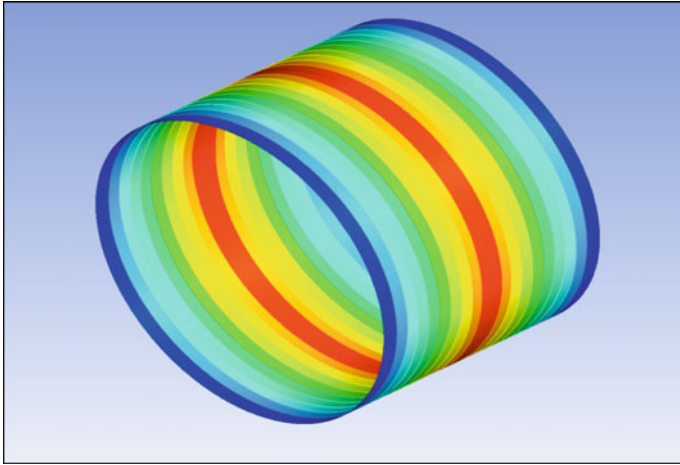


Fig. 1.6 Pressure distribution contour obtained for bearing having $L/D = 0.75$

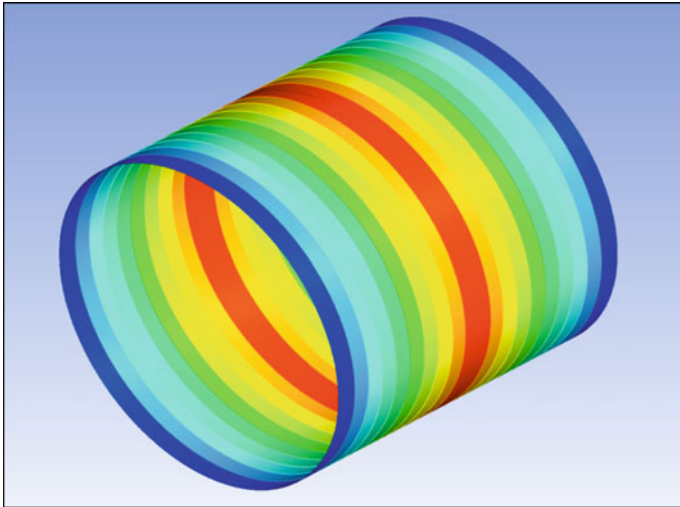


Fig. 1.7 Pressure distribution contour obtained for bearing having $L/D = 1.00$

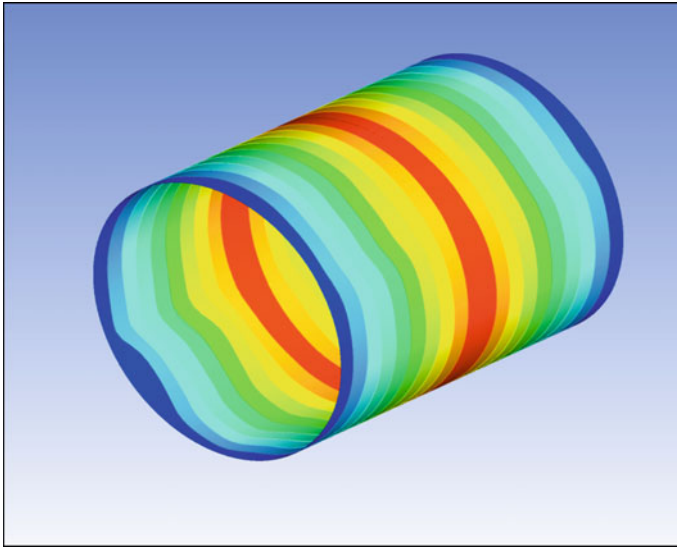


Fig. 1.8 Pressure distribution contour obtained for bearing having $L/D = 1.25$

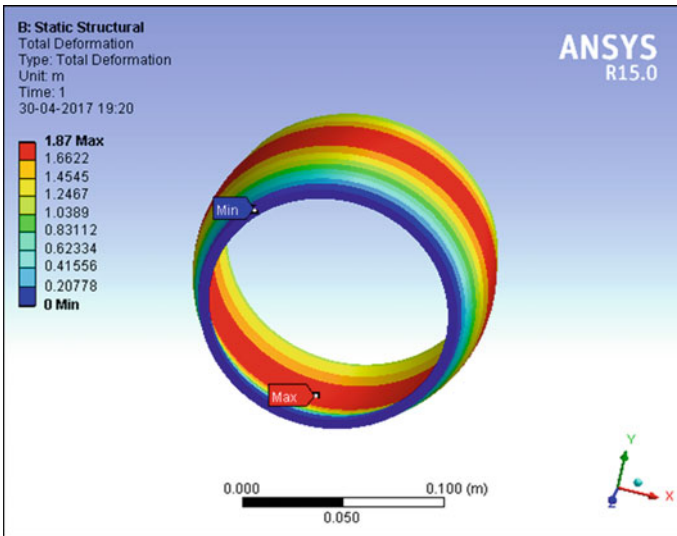


Fig. 1.9 Total deformation contour obtained for bearing having $L/D = 0.75$

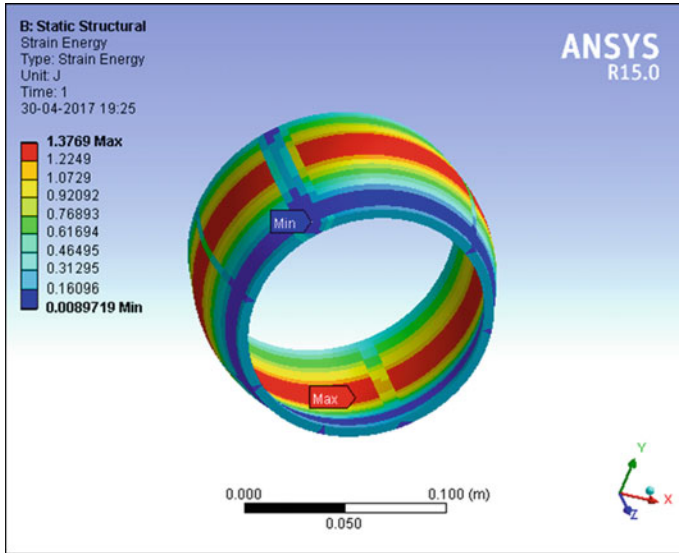


Fig. 1.10 Strain energy contour obtained for bearing having $L/D = 0.75$

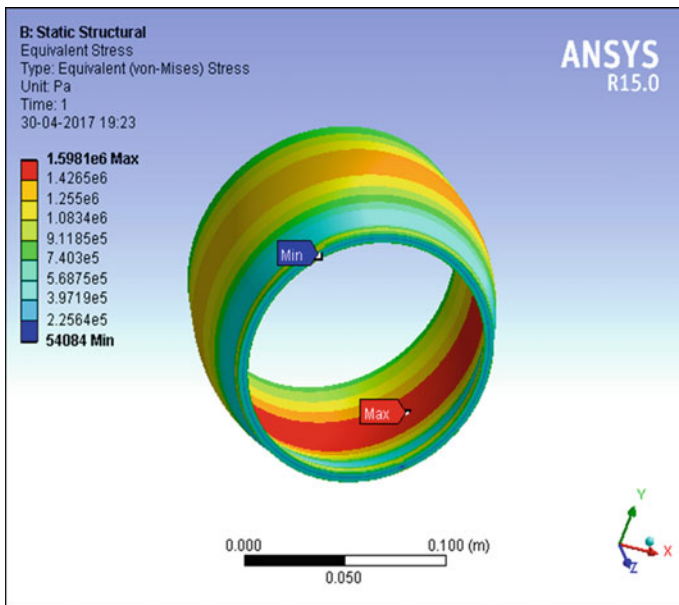


Fig. 1.11 Equivalent (von Mises) stress contour obtained for bearing having $L/D = 0.75$

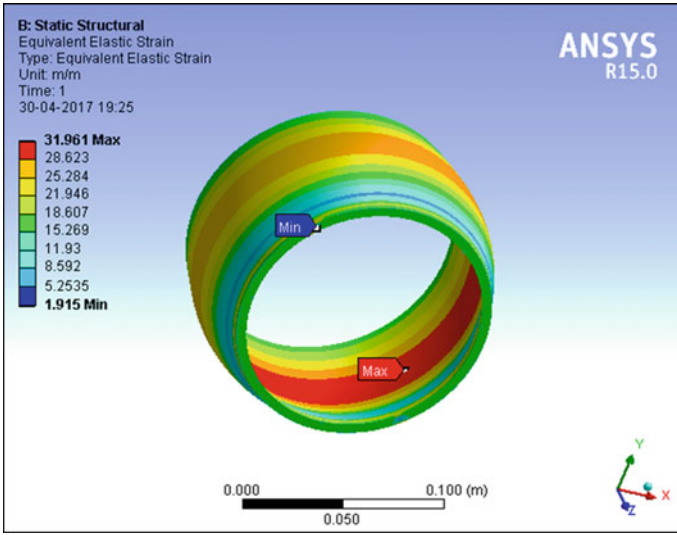


Fig. 1.12 Equivalent elastic strain contour obtained for bearing having $L/D = 0.75$

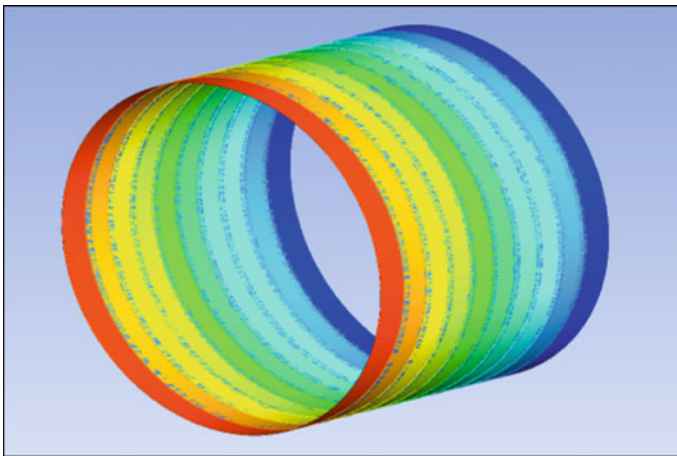


Fig. 1.13 Pressure distribution contour obtained for bearing having $L/D = 0.75$

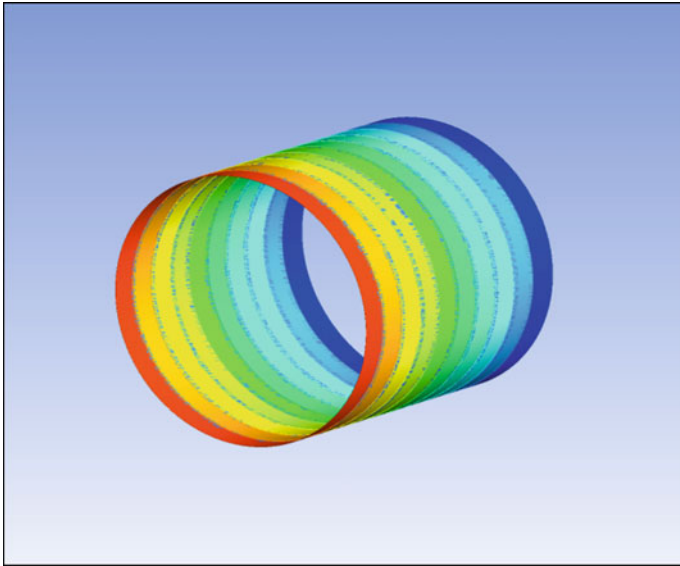


Fig. 1.14 Pressure distribution contour obtained for bearing having $L/D = 1.00$

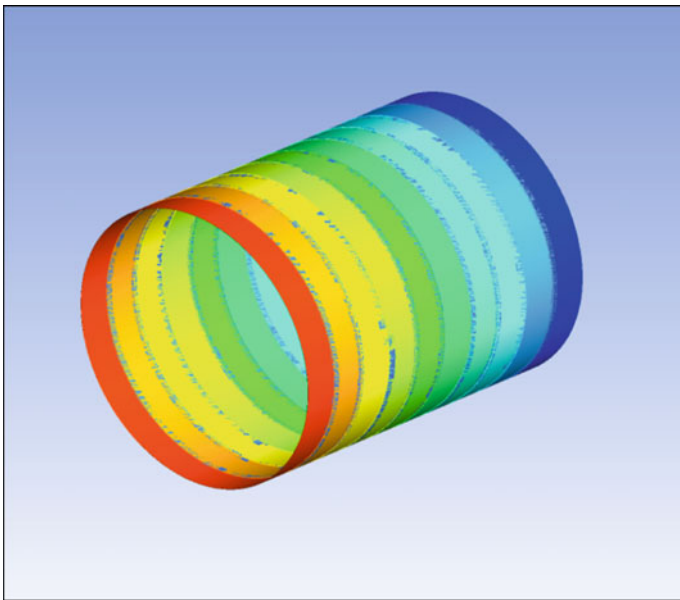


Fig. 1.15 Pressure distribution contour obtained for bearing having $L/D = 1.25$

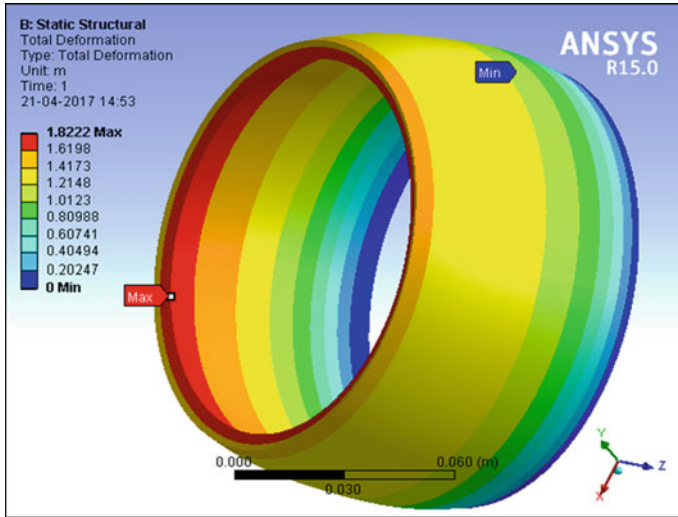


Fig. 1.16 Total deformation contour obtained for bearing having $L/D = 0.75$

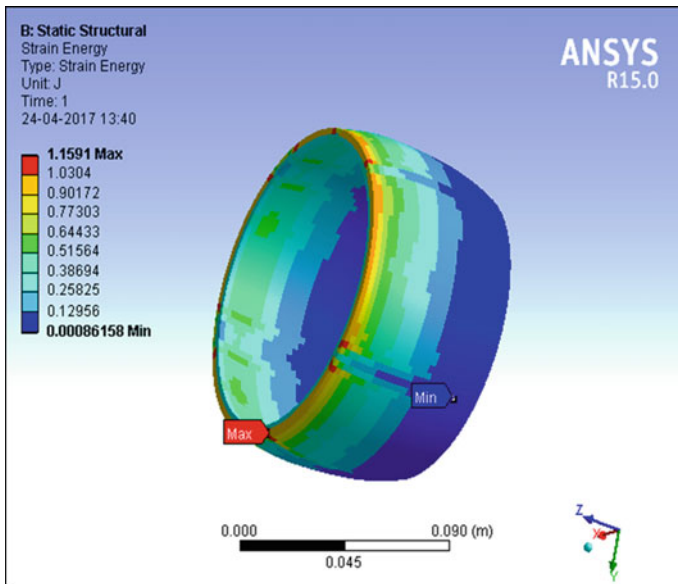


Fig. 1.17 Strain energy contour obtained for bearing having $L/D = 0.75$

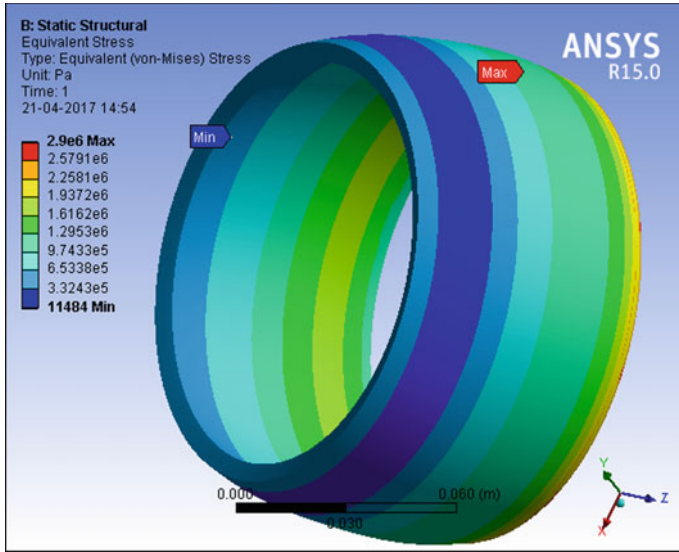


Fig. 1.18 Equivalent (von Mises) stress contour obtained for bearing having $L/D = 0.75$

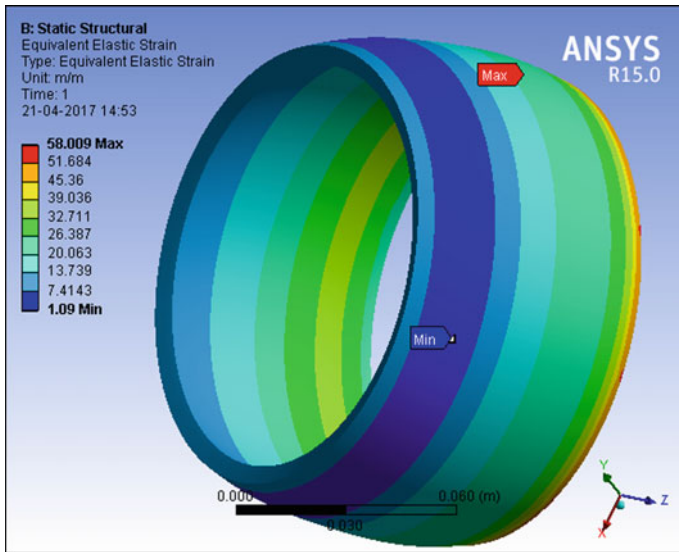


Fig. 1.19 Equivalent strain contour obtained for bearing having $L/D = 0.75$

References

1. Maurya, A., Kumar, A., Punia, A. D.: CFD and frictional torque analysis of hydrodynamic journal bearing. *Int. J. Eng. Res. Technol. (IJERT)* **8**(7) (2019)
2. Mane, R.M., Soni, S.: Analysis of hydrodynamic plain journal bearing. *EJAET* **2**(2), 92–101 (2015)
3. Raghvendra, N., Math, M.C., Sharma, P.R.: Finite element analysis of hydrodynamic journal bearing. *Eur. J. Adv. Eng. Technol.* **2**(2), 92–101 (2015)
4. Hersey, M.D.: *Theory of lubrication*. Wiley, London, New York (1936)
5. Mehra, C., Kokadiya, A.M.: Study of pressure profile in hydrodynamic lubrication journal bearing

Chapter 2

Design and Analysis of Composite and Al Alloy Wheel Rim



Pankaj Singh Bisht and Ankita Awasthi

Abstract This paper shows the comparative study of Al alloy wheel rim and composite wheel rim to analyse the strength and weight of 14 inches wheel under same load conditions by using computational modelling and analysis. For this paper model, the wheel rim is created by using a 3D CAD software Creo 3.0, and analysis is done by using ANSYS. For this paper, we select few selected orientations of the composite materials, such as $[\pm 35^\circ]_{FW}$, $[\pm 45^\circ]_{FW}$, $[\pm 55^\circ]_{FW}$, $[\pm 75^\circ]_{FW}$ and Al alloy of grade Al6061 which is commonly used by wheel manufacturing companies. As we know Al alloy is used nowadays commercially for its good strength and aesthetic look, and composite materials are also used by super car manufacturers wheel manufacturers also making wheel for super cars to make them lighter in weight and good in aesthetic looks. In this present paper, design and analysis of the composite wheel with various fibre orientation angles are done with the help of ANSYS composite pre- & post (ACP)-module in ANSYS Workbench 15.0.

Keywords Design · Analysis · Composite wheel · Al alloy wheel · Al6061 · Creo 3.0 · ACP pre- and post-module of ANSYS workbench 15.0

2.1 Introduction

A wheel is a round-shaped block of a high-strength and toughest material. Its centre is bored of a circular hole through which an axle bearing is tightened about which the wheel rotates when a moment generated by engine is applied to the vehicle axle about its axis, wheel and axle [1]. The wheel is a rotating part of a vehicle, in which rubber tyre is placed in between the flange at a pressure which is different from the ambient pressure. High pressure in between wheel and tyre, tyre must withstand, and there should be no crack at the surface or no leakage. Maximum pressure like a 0.241 MPa, i.e. fatigue load cycle and burst pressure [2, 3]. It occurs during refilling of

P. S. Bisht (✉) · A. Awasthi
IILM-CET-AHL, Greater Noida, Uttar Pradesh 201306, India
e-mail: pankajbish0195@gmail.com

A. Awasthi
e-mail: ankita.awasthi@iilmcet.ac.in

© Springer Nature Singapore Pte Ltd. 2020

I. Singh et al. (eds.), *Advances in Materials Engineering and Manufacturing Processes*,
Lecture Notes on Multidisciplinary Industrial Engineering,
https://doi.org/10.1007/978-981-15-4331-9_2

air. It should maintain high pressure between the tyre and wheel bead seat. Wheels are used in various applications such as automobile and aerospace which are traditionally produced with help of isotropic materials such as aluminium alloy [4]. Steels we are using are composite materials like carbon fibre, Kevlar fibre, glass fibre, etc [4, 5].

2.2 Types of Wheels

The wheel must have enough strength to perform its functions properly, should be balanced statically and dynamically as well, and it should be lightest possible to reduce unsprung weight. It can be internally or externally applied pressure on the wheel [6, 7]. In today's scenario, there are various types of wheels present, but generally steel and wire spokes are used for these purposes all around. Steel wheels are stronger than wire and aluminium alloy wheel, but it is heavier than alloy wheels which increase the unsprung weight of the vehicle. Alloy wheel is preferred for automobile application to reduce unsprung weight of the vehicle [6, 7]. To reduce the unsprung weight of vehicle researchers, design various types of wheels and describe it into five types.

2.2.1 Type 1: Wheel/Rim (On the Basis of Dimension)

Drop centre wheel rim (DC): Its shape is designed in such a way that there should be fine gap between the bead seat parts of the wheel which is placed on both sides of the wheel rim. It is manufactured such that it is easy to mount and dismount the tyre. In most of the cases, there is a draft angle of 5° in the bead seat area [6].

Wide drop centre wheel rim (WDC): It is almost same as drop centre wheel rim. To expand the width of the rim, a slighter increase in well and a lower flange height, this rim is commonly used for tyres of passenger vehicles for which this design is presently used [6].

Wide drop centre wheel rim with hump: In this design, a bump is added on the beginning of the bead seat area. It is used to prevent the bead sliding down and air outflow from the rim due to the horizontal force applied to the tyre when a vehicle tubeless tyres runs at high speed. [6] (Table 2.1; Figs. 2.1 and 2.2).

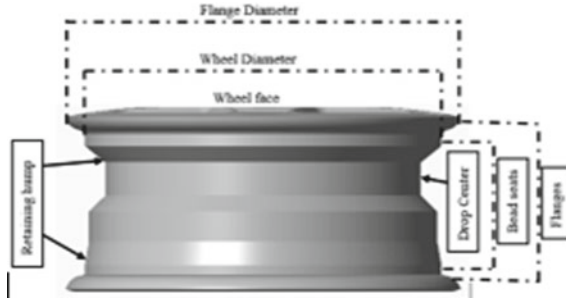


Fig. 2.1 Drop centre (DC) rim

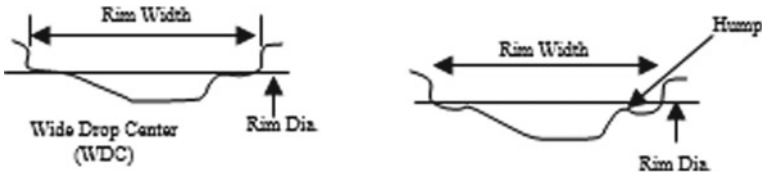


Fig. 2.2 Wide drop centre (WDC) and wide drop centre with hump rim

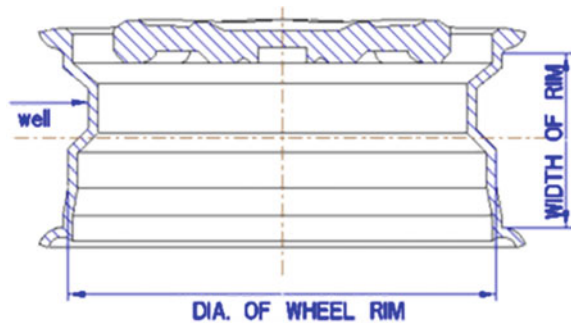
Table 2.1 Comparable table on weight of wheel types

Type of wheels	Weight (%)
Steel wheel	100
Wire wheel	85
Alloy wheel	75
Composite wheel	60

2.3 Basic Structure of Wheel Rim

1. Wheel: Rim and disc forms wheel [8, 9].
2. Rim: The part of wheel where the tyre is installed is known as rim [8, 9].
3. Disc: A part which is fixed with the axle hub of the vehicle is disc [8, 9].
4. Bead seat: A part of rim which holds the tyre in a radial direction and approaches in contact with the bead face [8, 9].
5. Hump: It is a bump which was put on the bead seat for the bead to prevent the tyre from sliding off the rim while the vehicle is moving [8, 9].
6. Well: The depth and width of a rim facilitate tyre mounting and removal from the rim (Fig. 2.3) [8, 9].

Fig. 2.3 Structure of wheel rim



2.4 Objective of Paper

The objective of this paper is as follows:

- To show that multilayer wheel rim is more suitable for high load and forces than Al alloy wheel.
- To show there is reduction in weight of composite wheel over the Al alloy wheel.
- To show the stress in E-glass fibre in different orientations.
- Wheel rim is designed as per JETMA.
- The thickness of rim area of wheel is taken as 1 mm of seven layers.
- The thickness of central part of wheel rim is taken as 1 mm of 14 layers.

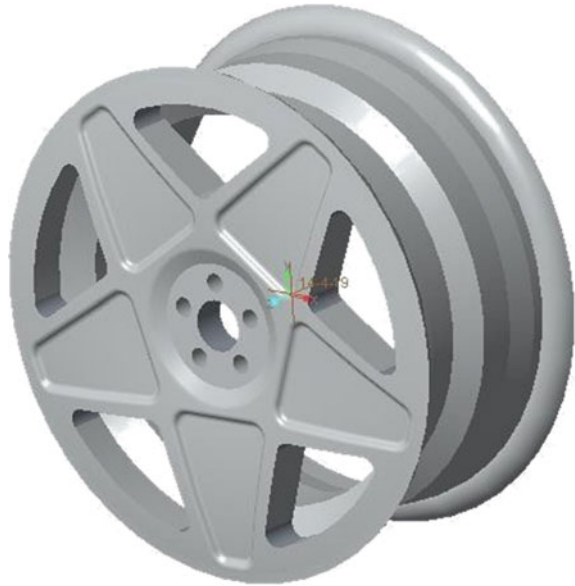
Problem Definition

To optimize the design of wheel rim for safer and lighter than the conventionally used wheel rim of Al alloy and steel by using E-glass fibre (Table 2.2; Fig. 2.4).

Table 2.2 Specification of proposed car wheel rim

S. No.	Specification	Value
1	Width of the rim (mm)	140
2	Diameter of the rim (mm)	355
3	Offset (mm)	57
4	Central hole diameter (mm)	40
5	Thickness of the rim (mm)	7
6	Diameter of stud hole (mm)	15
7	Diameter of stud hole circle (mm)	68
8	Number of stud holes	5 No's

Fig. 2.4 Proposed 3D designed CAD



2.5 Boundary Condition and Drawing

1. Fixed support is given to the five bolt/stud holes because wheel is fixed by the bolt through stud holes in vehicle axle [10].
2. Total bearing load of 7769.5 N is applied at the hub centre in 'Y'-direction because hub is fixed in the central hole of the rim and applies load on the rim like bearing [10].
3. On the tyre allocation area there is pressure of 0.241 Mpa which acts normally on the circumferential tread and flange portion of the wheel [10].
4. By considering the diameter of tyre as 550 mm, velocity of car rim is taken as 100 kmph, i.e. 965 RPM [10].
5. From annexure of AIS-073 (part 2), moment is taken as 5.0969e+5 N-mm [10].
6. Friction force is provided into the inner face of centre hole which comes in action with axle [10].

Mechanical drawing of wheel will help to check the applicability of selected design parameters (Fig. 2.5).

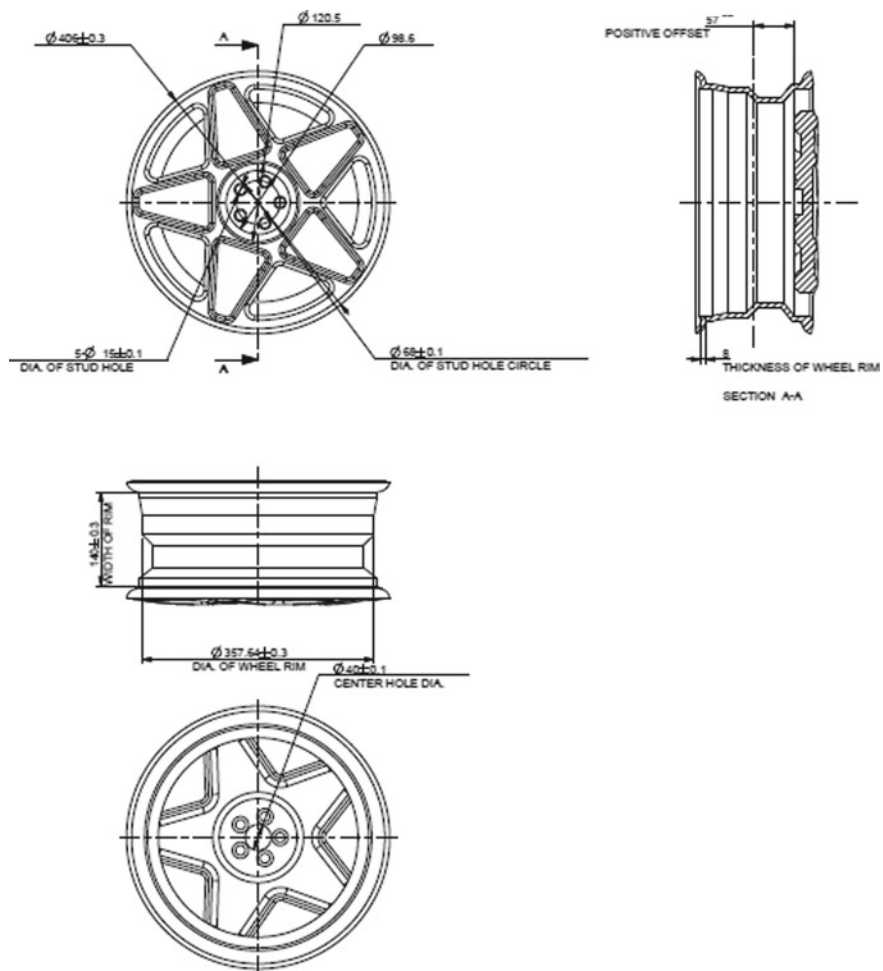


Fig. 2.5 Mechanical drawing

2.6 Analysis Result

In this report, we have analysed various variants of composite wheel rim of 14 inches having same thickness around the flange, width of rim, for hub and spoke area, it has different thickness than the flange, and for each variant, we have taken various orientation angles like $\pm 35^\circ, \dots, \pm 75^\circ$. The modelling of E-glass/resin epoxy is oriented at angles of $\pm 35^\circ, \pm 45^\circ, \pm 55^\circ$ and $\pm 75^\circ$ (Fig. 2.6).

VARIANT-1 ($\pm 35^\circ$)

See Figs. 2.7, 2.8 and 2.9.

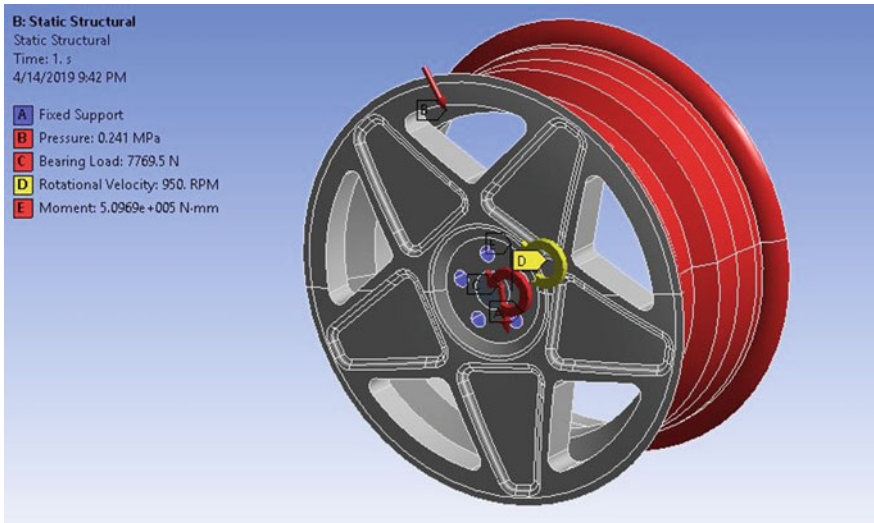


Fig. 2.6 Load condition for proposed wheel

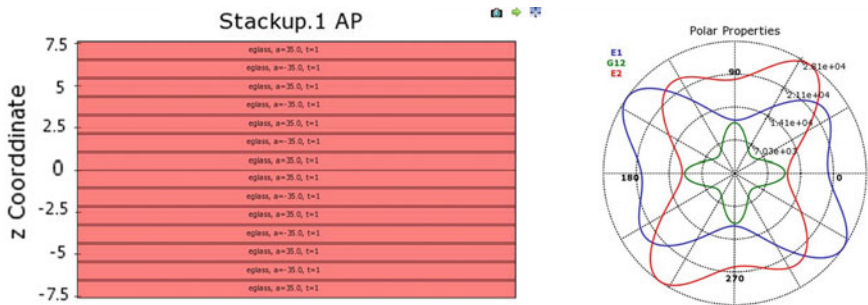


Fig. 2.7 Layer stack up at ($+35^\circ -35^\circ$)

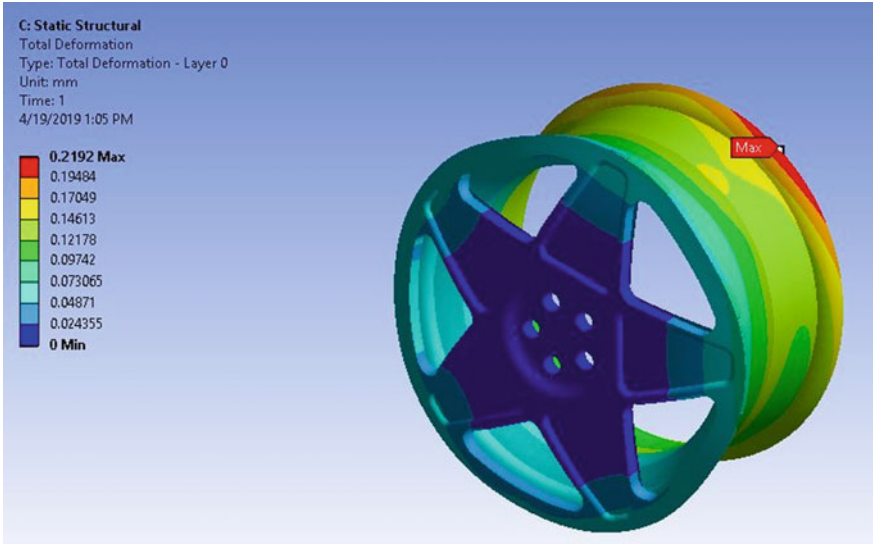


Fig. 2.8 Total deformation of E-glass at $[\pm 25^\circ]$ FW

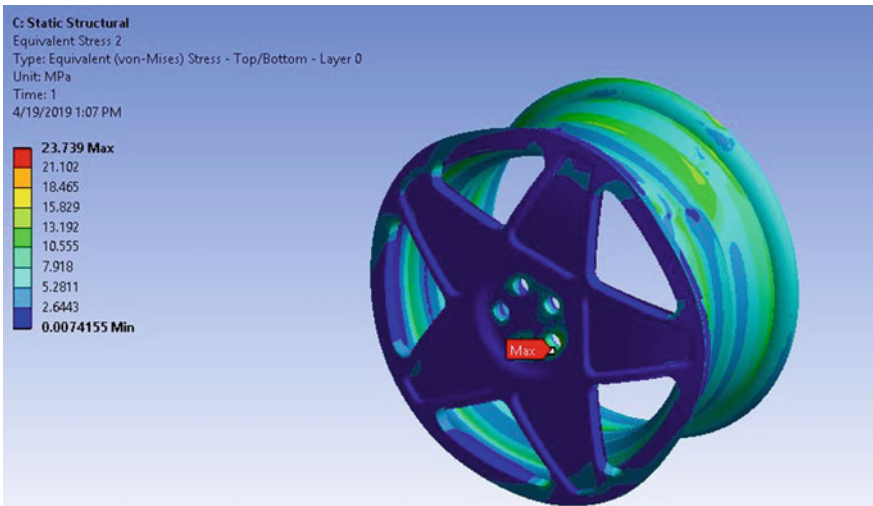


Fig. 2.9 Max. stress is observed at bolt area

VARIANT-2 ($\pm 45^\circ$)

See Figs. 2.10, 2.11 and 2.12.

VARIANT-3 ($\pm 55^\circ$)

See Figs. 2.13, 2.14 and 2.15.

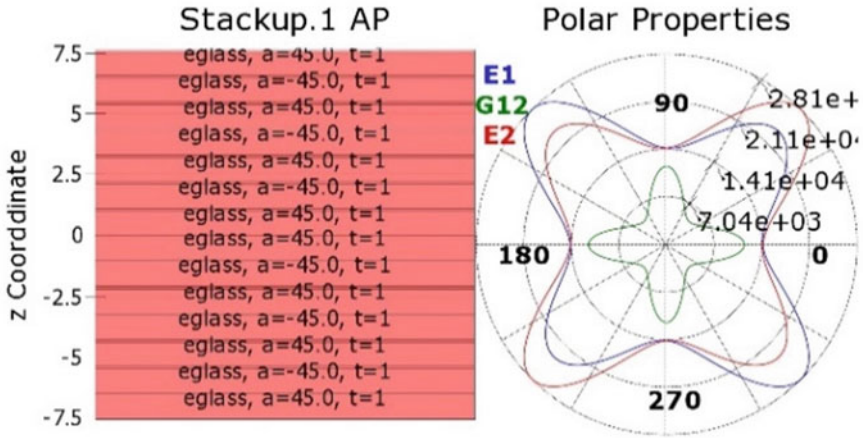


Fig. 2.10 Layer stack up at (+45° -45°)

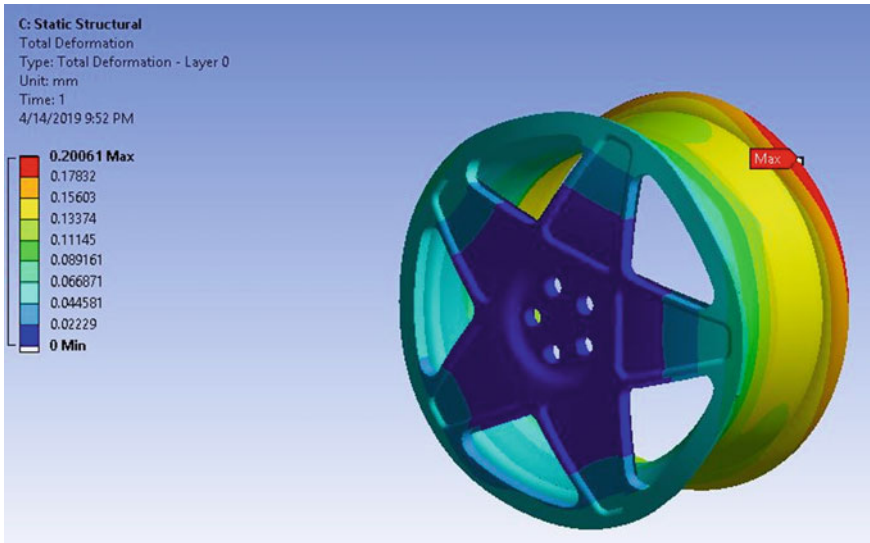


Fig. 2.11 Total deformation at of E-glass at ($\pm 45^\circ$)FW

VARIANT 4 ($\pm 75^\circ$)

See Figs. 2.16, 2.17, 2.18.

VARIANT-5 Al alloy

See Figs. 2.19 and 2.20.

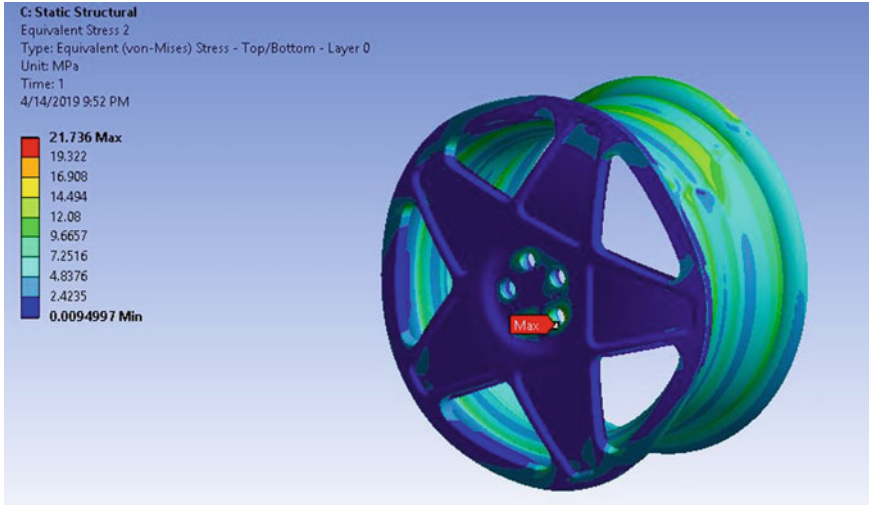


Fig. 2.12 Max. stress observed at bolt area

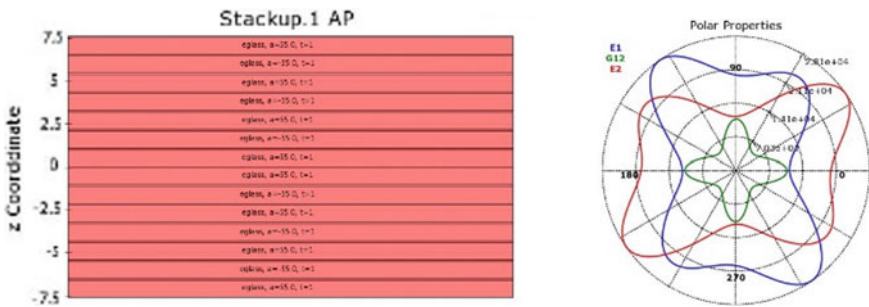


Fig. 2.13 Layer stack up at (+55° –55°)

2.6.1 Result Table

Variants	Orientation	Total deformation (mm)	Equivalent stress (Mpa)
1	±35°	0.2192	23.739
2	±45°	0.20061	21.736
3	±55°	0.19384	18.687
4	±75°	0.22755	20.541
5	Al6061	0.00839	21.239

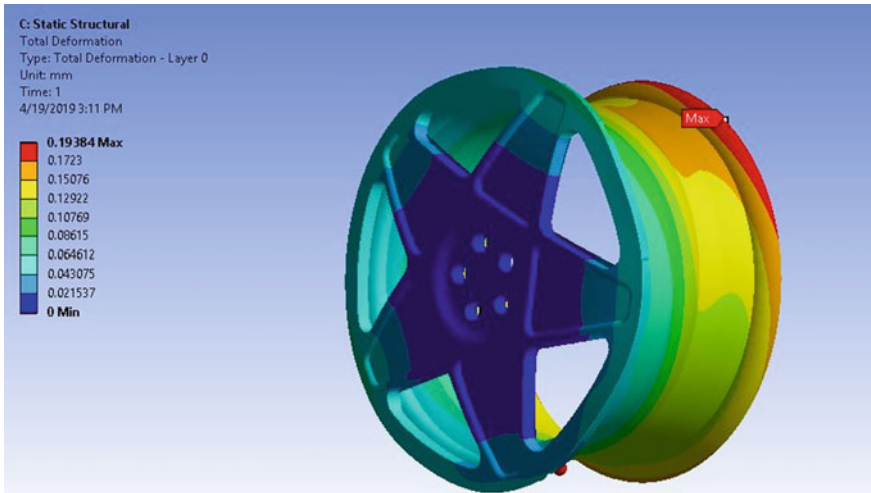


Fig. 2.14 Total deformation of E-glass at ($\pm 55^\circ$)FW

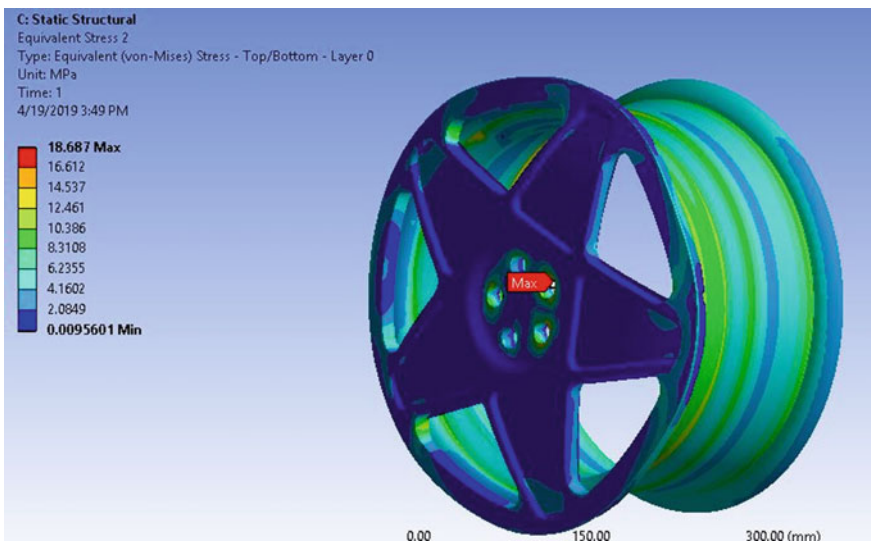


Fig. 2.15 Max. stress observed at bolt area

2.7 Conclusion

From this work, following conclusions are drawn:

1. From above results, it is clear that aluminium has less deformation at applied boundary condition but for the successful design, stress of the particular geometry

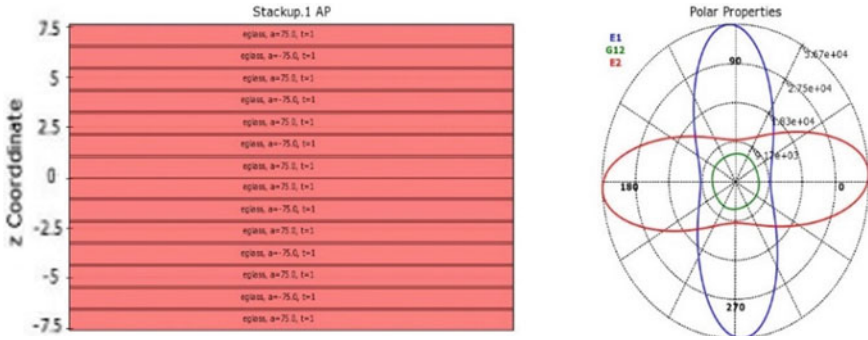


Fig. 2.16 Layer stack up at (+75° -75°)

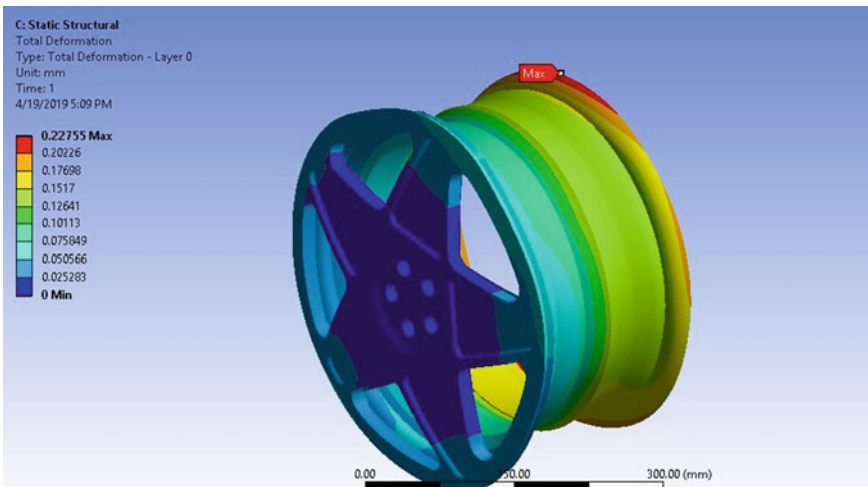


Fig. 2.17 Total deformation of E-glass at (± 75°)FW

plays an important role because 5% of total length deformation cannot be seen by naked eyes and up to yield strength, it can regain its position.

- From above result, it is clear that determined stress is less than allowable stress, so design is safe, as Al6061 has less equivalent stress than allowable stress and E-glass fibre having orientation [-55, +55] FW has less equivalent stress than Al6061 but greater deformation, which is allowed for safer design of particular geometry.
- E-glass gave good aesthetic view, it has greater tensile strength, and no corrosive effect can be seen.
- E-glass has good strength than Al6061. For same design, Al6061 has 10.56 kg of weight, while E-glass has 7.8 kg.
- We conclude that E-glass is 25% lesser in weight, and proposed design is safer.

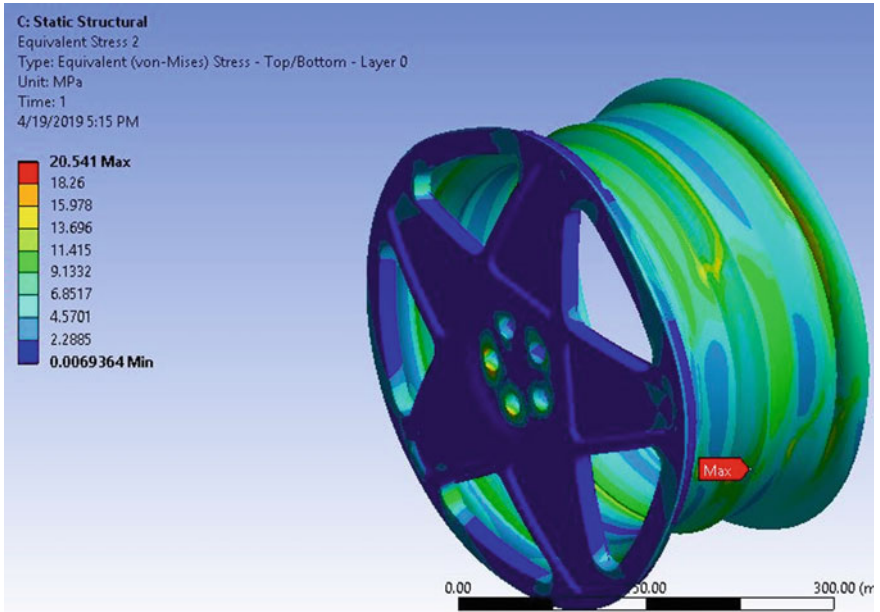


Fig. 2.18 Max. stress observed at inner flange

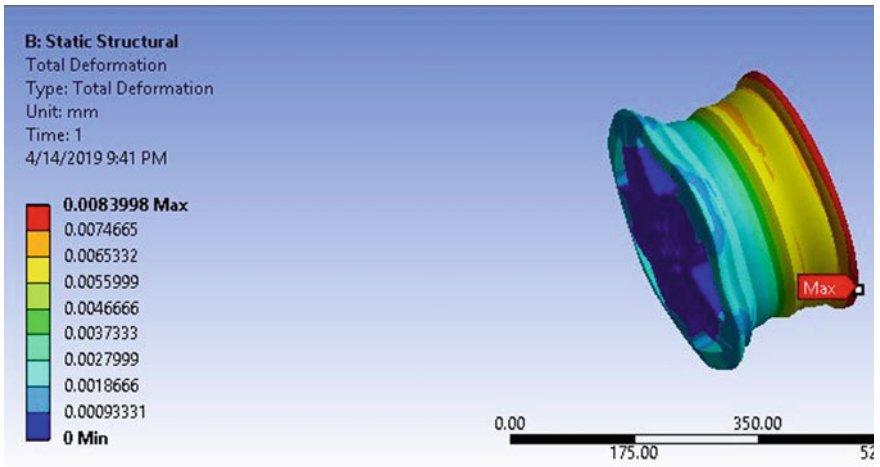


Fig. 2.19 Total deformation of Al6061 Al alloy

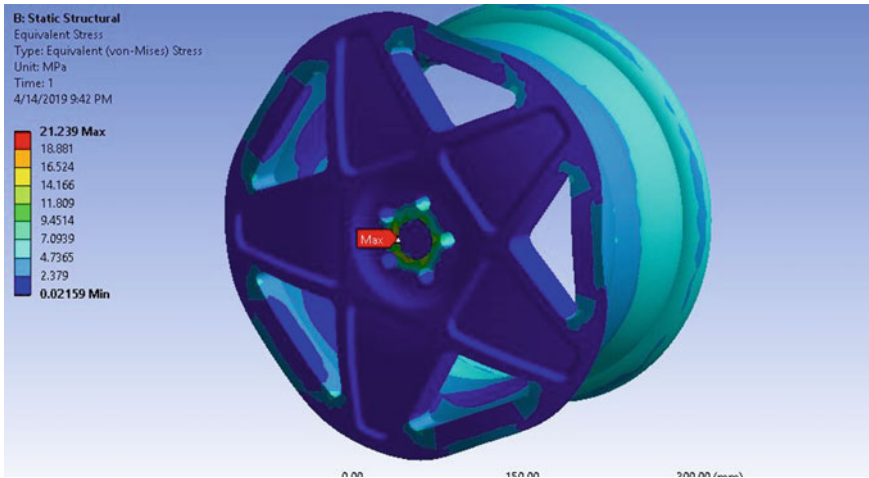


Fig. 2.20 Max. stress observed at bolt area

2.8 Future Scope

In this paper, we solely dedicated our focus to static stress analysis and to optimize the design of composite wheel rim and reduce the weight of the wheel. We selected a common material for all the variants having different orientation angle, but we did not focus our attention on fatigue life of wheel rim and dynamic analysis of wheel rim. So, there should be scope which remains.

References

1. Thakare, R.B.: Stress analysis in wheel rim by using dynamic cornering fatigue test under different conditions. *IJARIE- ISSN(O)-2395-4396* 3(2) (2017)
2. Nirala, S.K., Shankar, S. Sathishkumar, D., Kavivalluvan, V., Sivakumar, P.: Carbon fiber composites: a solution for light weight dynamic components of AFVs” *Ref. Sci. J.* **67**(4) (2017)
3. Chopade, R.B., Pateriya, A., Shirbhate, A.D.: Review of design, analysis of four wheeler alloy material rim using FEA method under cornering fatigue test. *IJIIRD* **02**(02). ISSN: 2456-236X (2018)
4. Tsai, S.W., Wu, E.M.: A general theory of strength for anisotropic materials. *J. Compos. Mater.* **5**, 58– 80 (1971)
5. Schweizer, N., Giessl, A., Schwarzhaupt, O., Büter, A.: Development of a composite wheel with integrated hub motor. In: *15th European Conference On Composite Materials (ECCM15)*, Venice, Italy (24–28 June 2012)
6. Dinesh Kumar, M., Narendra Mohan, P., Purna Chandra Sekar, B., Touseef Ahamad, Md.: Static analysis of wheel rim using catia and ansys16.0. *IRJET* **3**(7) (2016)
7. Bao, Y., Zhao, X.: Research of lightweight composite automobile wheel. *World J. Eng. Technol.* **2017**(5), 675–683 (2017)

8. Babu, M., Hariharan, V.S.: Modelling and analysis of automotive wheel rim. *IJIRSET* **5**(4) (2016)
9. Blasco, J., Valero, F., Besa, A., Rubio, F.: Design of a Dynamometric Wheel Rim. Springer Science + Business Media Dordrecht (2014)
10. Gondhali, S.L., Dhale, AD., Pagare, S.: Static Structural Analysis of Car Rim by Finite Element Method. Springer Nature Singapore Pvt Ltd. (2019)

Chapter 3

A Critical Review of Process Parameters in Laminated Object Manufacturing Process



Rishabh Gupta, Manish Dalakoti, and Andriya Narasimhulu

Abstract Laminated object manufacturing (LOM) is one of the sheet lamination additive manufacturing processes used to manufacture 3D solid object with the help of sheet lamination process. A formerly developed and verified model of LOM was used to study and find out the effects of various process parameters on the temperature profile in the part during the build cycle in this process. The process parameters, i.e., roller speed, roller temperature, cutting time of laser, air temperature of the chamber and the base plate temperature, were varied independently, and their response on the LOM process is noted. This study also presents an analysis of one of the major problems occurred in LOM process, i.e., warping and an optimal combination of these process parameters to reduce this warping effect.

Keywords Additive manufacturing · LOM · Process parameters · Warping

3.1 Introduction

Laminated object manufacturing is an additive manufacturing process developed by California-based company—Helisys Inc. in which the sheets of material are bonded to form an object. Electric energy, chemical adhesive or ultrasonic energy is used as an energy source in this process. Materials used in this process are plastic, metal tapes or foils and paper. Interaction between energy source and material becomes possible by means of adhesive, bonding or welding [1]. Laminated objects are commonly utilized for stylish and visual models and are not suitable for auxiliary utilization. The understanding of the thermal behavior of a part build during the LOM process is very important in the part fabrication with better lamination characteristics. The top

R. Gupta (✉) · M. Dalakoti · A. Narasimhulu
Department of Mechanical Engineering, Netaji Subhas University of Technology, New Delhi,
India
e-mail: rishabh3008@gmail.com

M. Dalakoti
e-mail: manishdalakoti05@gmail.com

A. Narasimhulu
e-mail: andriya@nsut.ac.in

© Springer Nature Singapore Pte Ltd. 2020

I. Singh et al. (eds.), *Advances in Materials Engineering and Manufacturing Processes*,
Lecture Notes on Multidisciplinary Industrial Engineering,
https://doi.org/10.1007/978-981-15-4331-9_3

layer with low temperature may result in the poor adhesion of the individual layer which results into delamination of the completed part, while the more temperature results in the structural rigidity loss during the part build which leads to excessive compression or shearing during the pressure application by the heated roller. In order to understand better, the transient behavior (thermal) of the part, a verified mathematical model, was developed [1]. So it was decided to study and find out the effects of certain parameters with the help of this model by varying their values. A number of experiments were conducted in a relatively shorter time to study their effects on the part build with the help of this model, and this also eliminates the use of high-cost actual LOM machine. Also analysis of base plate and chamber air temperature with the help of this model can be done that is not implemented on LOM machine.

3.2 Background

The full details of the mathematical model have been formerly given by Flach et al. [1]—that’s why only a brief description of the capabilities of this model will be described here.

A mechanical sub-model does not included in this model, and thus, the coupling of mechanical and thermal behavior cannot be fully simulated. However, by adjusting one of the parameters of the model (roller to part heat transfer coefficient), we can get effective results between the actual temperature and the predicted temperature with in a part. Thus, this model is fully able to measure and analyze the thermal behavior of the LOM process.

3.3 Experiments

The pattern of experiments was designed for a work. This work involved a layup of 260- μ m-thick silicon carbide ceramic tapes, and a twenty-layer 12.20 cm \times 5.35 cm block of “green” ceramic material was produced. Data of material property and parameters for this base case is summarized in Table 3.1. All the parameters were measured experimentally except the roller to part heat transfer coefficient which was used as an adjusting or tuning parameter.

The parameters selected for analysis were as follows: roller speed, roller temperature, cutting time of laser, chamber air or surrounding temperature and the base plate temperature. The roller temperature and the speed have an impact on the amount of transfer of heat from roller to part, while chamber air temperature and base plate temperature have an impact on the rate of loss of heat of the part block. The amount of cooling between the successive layers is affected by the laser cutting time. All of these parameters influence the short-term as well as the long-term thermal behavior of the part. The values of these parameters used in this experiment and changes

Table 3.1 Machine parameters and material properties for base simulation [1]

Material	Silicon carbide ceramic tapes
Thermal conductivity	$1.25 \text{ Wm}^{-1} \text{ K}^{-1}$
Density	1.98 g cm^{-3}
Heat capacity	$1.05 \text{ Jg}^{-1} \text{ K}^{-1}$
Part dimensions	$121.9 \text{ mm} \times 53.3 \text{ mm}$
Layer thickness	0.25 mm
Number of layers	20
Heat transfer coefficient (part to air)	$18 \text{ Wm}^{-2} \text{ K}^{-1}$
Heat transfer coefficient (part to base)	$14 \text{ Wm}^{-2} \text{ K}^{-1}$
Air temperature	22 °C
Base plate temperature	22 °C
Initial temperature of material	22 °C
Roller velocity	25.4 mm s^{-1}
Roller contact strip width	9 mm
Roller temperature	91 °C
Heat transfer coefficient (roller to part)	$3300 \text{ Wm}^{-2} \text{ K}^{-1}$
Build cycle time	120 s

made to them are summarized in Table 3.2. The complete experiment and its results are given there [3]. In trials 15–18 in order to observe the dynamic response of the process to the variable change, the parameter values were changed. In the table ‘a’ signifies that the parameter value had changed midway through the run from first value to the second.

3.4 Results and Discussion

The temperature below the bottom most (first) layer was indicative of the part body temperature. So, in order to compare the response of the part when undergone through different parameters, it was determined to notice the first-layer temperature only (Fig. 3.1).

The first parameter studied was roller temperature. The roller temperature was deviated in the range between 91 and 150 °C, and all the other parameters were kept constant and same as in the base trial (Trial 1). The temperature of the surface layer (in contact with the roller) is most significantly affected. From Fig. 3.2, mean part body temperature increased about 10 °C for every 50 °C rise in the temperature of the roller.

Table 3.2 Schedule of LOM parameters [2]

Trial	Roller temperature (°C)	Roller speed (cm/s)	Base plate temperature (°C)	Chamber air temperature (°C)	Laser cutting time (s)
1	91	2.54	22	22	77
2	150	2.54	22	22	77
3	200	2.54	22	22	77
4	250	2.54	22	22	77
3	200	2.54	22	22	77
5	200	2.54	50	22	77
6	200	2.54	75	22	77
7	200	2.54	100	22	77
3	200	2.54	22	22	77
8	200	2.54	50	50	77
9	200	2.54	75	75	77
3	200	2.54	22	22	77
10	200	3.81	22	22	77
11	200	5.08	22	22	77
12	200	2.54	22	22	57
3	200	2.54	22	22	77
13	200	2.54	22	22	97
14	200	2.54	22	22	117
15	91	2.54	22/50 ^a	22	77
16	91	2.54	22/100 ^a	22	77
17	91/150 ^a	2.54	22	22	77
18	91/200 ^a	2.54	22	22	77

The roller speed was studied next because the time of the contact of the roller with the part surface also influences the amount of heat transferred to the part. So, the overall build time of the part can be changed and affected by changing the roller speed. It was observed that for a 50% increase in the roller speed, the mean part body temperature decreased by about 7 °C and by about 23 °C for a 100% increase [3]. Again the top surface or layer in direct contact with the roller was the most affected one.

The next study involved the difference of the base plate temperature only. Increasing the base plate temperature gives the higher temperature to the work part being built. The mean part body temperature rises from 9 to 25 °C in base plate temperature. The results for the variation in this parameter are shown in Fig. 3.3. The impact of the variation in this process parameter on the process was taken as more efficient than the impact of roller temperature.

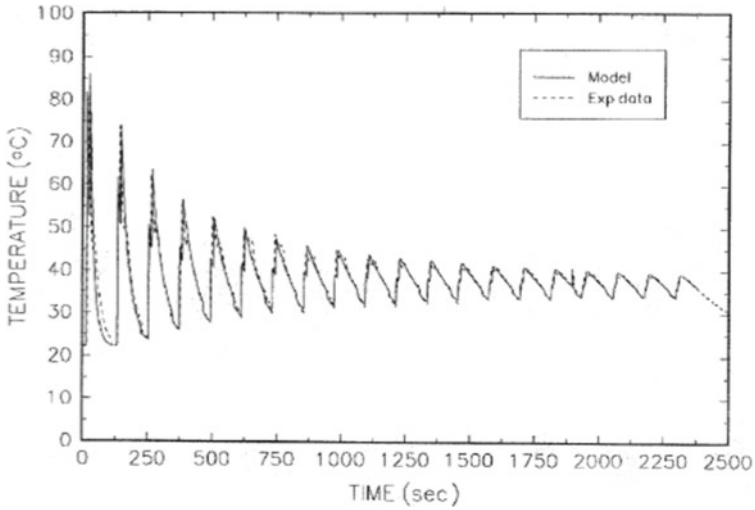


Fig. 3.1 Simulation and temperature profile (experimentally measured) for a 20-layered SiC part estimated by thermocouple above the 0th layer by using the experimental conditions from Tables 3.1 and 3.2 (Trial 1). Build time of cycle is 120 sec per layer during the build process

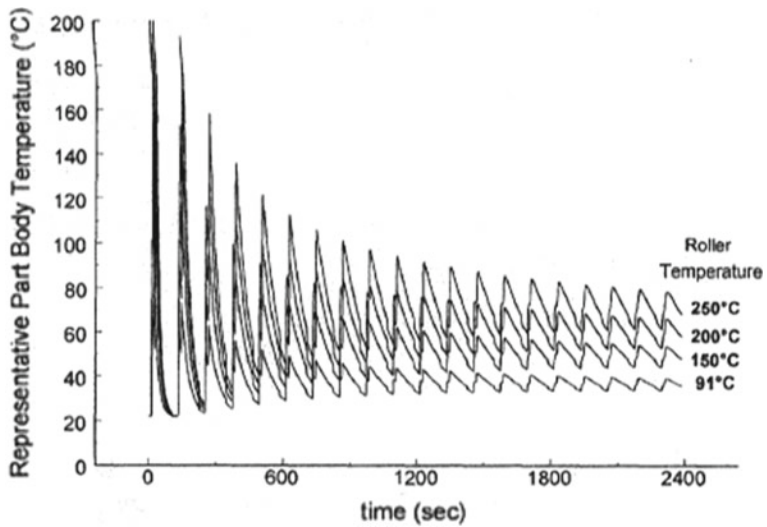


Fig. 3.2 Variation (parametric) of roller temperature: active, simulated temperature profiles of SiC part by using the given parameters in Table 3.2 (Trials 1–4)

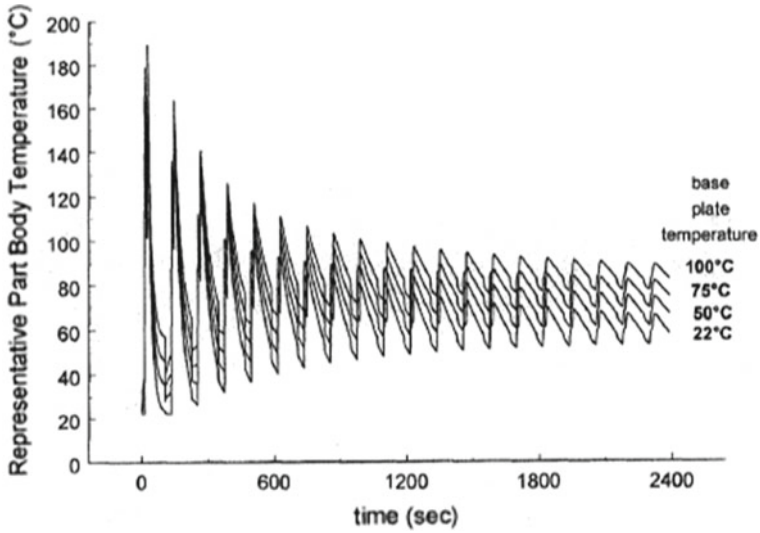


Fig. 3.3 Variation (parametric) of temperature of base plate using the given parameters from Table 3.2 (Trials 3, 5, 6, 7)

The next study involved the effect of changes in the chamber air temperature. The transient variation of the part body temperature with the varying base plate and chamber air temperature is shown in Fig. 3.4. The mean part body temperature rises

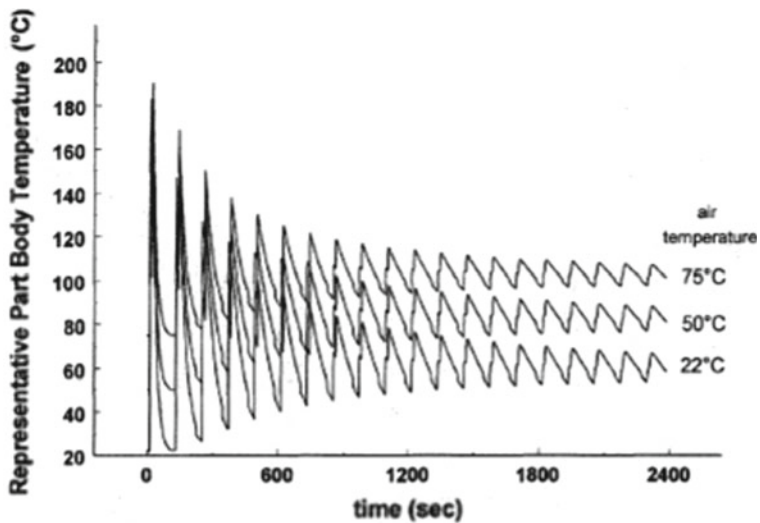


Fig. 3.4 Variation (parametric) of chamber air temperature using the given parameters in Table 3.2 (Trials 3, 8, 9)

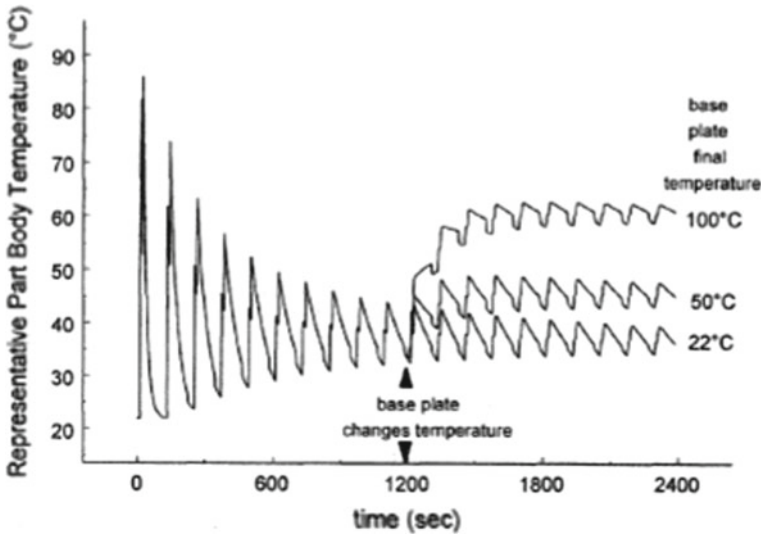


Fig. 3.5 Effect of varying base plate temperature midway through a run using the given parameters in Table 3.2 (Trials 15, 16)

from 20 °C approx to 25 °C in the chamber air and the base plate temperature. So, this effect was considered as the most efficient till now.

The value for laser cutting time is taken as 77 s for the experiment. Since the cycle time varies throughout the part build because of the changes in the cutting by laser from layer to layer, that's why this effect is needed to be investigated. Varying cutting time of laser applied between the layers successive to each other of build material affects the temperature of the part because of the reason that rising this time allows the extra time for the part to cool by heat transfer to the surroundings and the base plate. Though this effect was rather little, in most of the cases, for a 20 s increase in the laser cutting time, about 3 °C falls in the body temperature of the part occurred [3].

Some active tests were also performed where the base plate and roller temperature were varied through the build process to find out how many layers (or cycles) were needed for the work part to answer to the variation in these values. From Fig. 3.5, it can be concluded that the part body temperature consistently reaches its new mean temperature within 3–4 cycles. Also we got similar results for the variation in the temperature of the roller (Fig. 3.6).

3.5 Warping

Warping is the important type of problem in the laminated object manufacturing process. It frequently happens at the starting of the fabrication of part in the process,

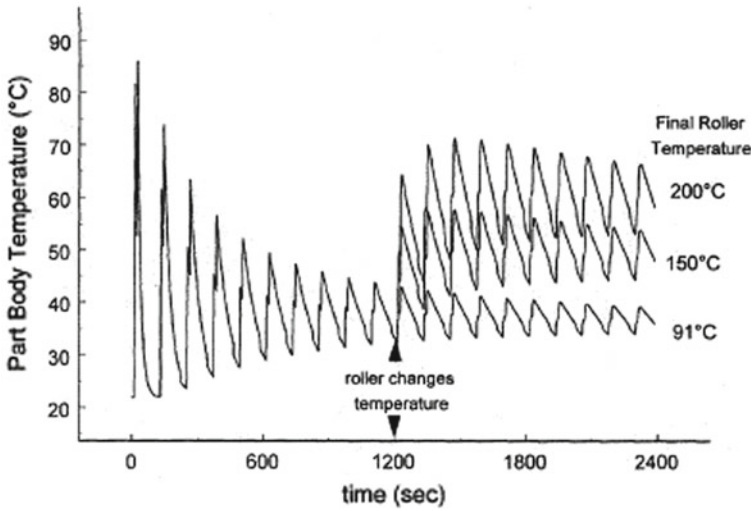


Fig. 3.6 Effect of varying the temperature of roller (from 91 °C) midway through a run using the given parameters in Table 3.2 (Trials 17, 18)

especially when the laminated part is cold, temperature of the heating is low or the size of the prototype is large. Warping generally begins at the end corners and curves of the part upward as shown in Fig. 3.7 [4].

Intra-laminar thermal forces produced by the non-uniform distribution of temperature at the interfaces of layer of the part also play a major role in causing the warping. When the hot roller is pressed onto the laminated layer of the part, the temperature at that layer rises and falls when it is removed during the laser cutting. During this process, the laminated layer extends or contracts with the variation of temperature during the operation resulting in the deformation between the layers due to the thermal force. This thermal force is considered as one of the most significant factors for warping. So, the analysis and simulation of this intra-laminar thermal force were conducted [5].

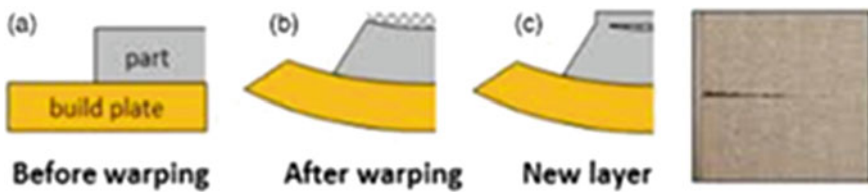


Fig. 3.7 Schematic of build plate warping effect during processing (a–c) and resultant damage

3.6 Conclusion

The analysis has shown that the process parameter studied above has an influence over the performance of the process. Mainly, the combination of base plate and chamber air temperature would appear to be the most sensitive for control of the overall part temperature, but practically using the base plate temperature could also be done to achieve the finite control. The roller temperature found to be the most effective parameter in influencing the temperature of the layer of the surface of the part. Thus if we require the high range of temperature at the surface of layers and lower temperature range all through the rest of the part, the control of this parameter would assign a mean to achieve this.

The main cause of warping is found to be intra-laminar thermal forces of compressive nature produced by the uneven thermal deformation between the layer interfaces. The process parameters like roller or flat speed, roller heating temperature and the contact pressure applied between the layers will affect the workability and warping of the part laminated. If the roller or flat is hotter and moves slower, the predicted intra-laminar thermal force will be smaller and the prototype will not appear to warp. So an optimum combination of the process parameter may be used to reduce the unwanted warping effect.

References

1. Flach, L., Klosterman, D., Chartoff, R.: A thermal model for laminated object manufacturing process. In: Proceedings of the Solid Freeform Fabrication Symposium, Austin, TX, Aug 1997, pp. 677–688
2. Flach, L., Jacobs, M.A., Klosterman, D.A., Chartoff, R.P.: Simulation of Laminated Object Manufacturing (LOM) With Variation of Process Parameters. Department of Chemical and Materials Engineering and Rapid Prototype Development Laboratory and Ohio Rapid Prototype Process Development Consortium, University of Dayton, USA, pp. 407–416
3. Jacobs, M.A.: Thermal Modeling and Control of the LOM Process. Undergraduate Honors Thesis, Chemical Engineering, University of Dayton, Apr 1998
4. Sames, W.J., List, F.A., Pannala, S., Dehoff, R.R., Babu, S.S.: The metallurgy and processing science of metal additive manufacturing. *Int. Mater. Rev.* **61**(5) (2016)
5. Lin, F., Sun, W.: Warping analysis in laminated object manufacturing process. *J. Manuf. Sci. Eng.* **123** (2001). <https://doi.org/10.1115/1.1403447>

Chapter 4

Performance Analysis of CI Engine Powered with *Simarouba Glauca* L. Biodiesel Fuel



A. Verma, K. S. Rawat, M. Saify, A. K. Singh, and P. Maheshwari

Abstract In the present work, the performance characteristics of CI engine, powered with *Simarouba Glauca* L. biodiesel blended fuel, have been analyzed at different load conditions. The CI engine test rig has been operated with fuel having different %, viz. 0%, 5%, 10%, 15%, and 20% of *S. Glauca* L. biodiesel. The performance parameters, namely brake thermal efficiency, brake specific fuel consumption, and volumetric efficiency, and emission characteristics such as NO_x, UBHC, and CO₂ have been analyzed. The experimental results revealed that the use of *S. Glauca* L. biodiesel in different % composition significantly affects the engine's performance. An improvement in brake thermal efficiency of the engine was observed when operated with blended fuel as compared to the conventional fuel. The diesel fuel blended with 15% *S. Glauca* L. biodiesel showed better results among all the % compositions studied in the current work.

Keywords Biodiesel · *Simarouba Glauca* L. · Engine performance analysis · Emission control

4.1 Introduction

Due to the global air pollution, the quality of air is continuously decreasing from required standards and the main source of air pollution in cities is motor vehicle, especially diesel [1]. The continuous use of fossil fuel for powering the automobiles exacerbated the environmental condition, and day-to-day depletion of oil reserve causes grave necessity to find alternative fuel. Due to the rising environmental pollution problems and depleting oil reserve, it has become the need of time to make research work more directed toward the development of alternative fuels [2]. Numerous studies have been conducted to explore different renewable fuel to replenish the

A. Verma (✉) · K. S. Rawat · M. Saify
Department of Mechanical Engineering, MIET, Meerut 250001, India
e-mail: ankur.verma@miet.ac.in

A. K. Singh · P. Maheshwari
Department of Mechanical Engineering, G.B. Pant University of Agriculture and Technology,
Pantnagar 263145, India

© Springer Nature Singapore Pte Ltd. 2020

I. Singh et al. (eds.), *Advances in Materials Engineering and Manufacturing Processes*,
Lecture Notes on Multidisciplinary Industrial Engineering,
https://doi.org/10.1007/978-981-15-4331-9_4

incessant demand of diesel [3–6]. Biodiesel has shown a positive impact in resolving these issues. Biodiesel as fuel received more attention from last two decades.

India stands first in global pollution death, with 9 million a year, so there is a great need to curb the pollution level. Today, complete transition from diesel to biodiesel engine seems implausible because many problems oriented with biodiesel. The atomization and combustion characteristics of biodiesel are notably different from diesel fuel as high viscosity of biodiesel interferes with injection process and leads to poor atomization [7]. The amalgamation of oil with air contributes to incomplete combustion, leading to heavy smoke emission. Both pour point and cloud point are notably higher than diesel fuel [8]. This high value may cause problem in cold weather. Coming to NO_x emission result showed that in most of cases, NO_x emission increases [9–11]. However, their different blends with diesel can be used result in low CO, PM, and sulfur [12, 13].

India's economy has been experiencing some of the greatest structural changes from 2000 to 2015. India imports approx. 81% of its oil need resulting in high cost of the fuel. Hence, biodiesel seems the most promising alternative of diesel fuel. Biodiesel can be derived from edible and non-edible feedstock [14, 15]. Previous research revealed that production of biodiesel was more focused on edible oil sources [16]. If this trend continues, then incessant production of biodiesel in future may lead to the depravity of edible oil. Production of biodiesel on commence of insecurity of food does not seem a good idea. Biodiesel used in this paper is *Simarouba Glauca* L. which is non-edible seed oil; however, there are many other non-edible seed oils like *Jatropha* and *Mahua*, but very few researches have been done on *S. Glauca*. This work explores the use of non-edible feedstock-based biodiesel which is cheap and eco-friendly than conventional diesel fuel. Moreover, the need of importing conventional fuel can be controlled up to some extent as biodiesel can be easily produced in India [17].

Simarouba Glauca L. most commonly known as laxmitaru, samba, or maruba supposed to be originated from America, especially from Amazon rainforest and tropical region of Mexico, Cuba, Haiti, and Central America. Biologically, it is categorized as the family of simaroubaceae quassia. It grows well in the wasteland of Orissa, Karnataka, and Gujarat along with Maharashtra and Tamil Nadu. It is non-edible and has great potential to diminish the import demand [18]. Oil content in *S. Glauca* L. compared to that of *Jatropha* is of approximate equal amount which makes it more vulnerable to use as biodiesel.

According to the laboratory reports of National Oilseeds and Vegetable Oil Development Board, *S. Glauca* L. in its pure form contains 0.06% of free fatty acid and remains in quality for an average of six months, with melting point of 27 °C. Biodiesel production from *S. Glauca* L. was started from the conversion of seed into oil follow by transesterification. Transesterification has been proven as most efficient and easiest method as compared to the other production techniques [19]. The crude *S. Glauca* L. oil was transesterified using KOH as catalyst and methanol to form biodiesel. The oil so obtained is green colored, relatively lighter, and less viscous than crude oil found by mechanical expression with odor of sweat. Table 4.1 shows the different properties of *S. Glauca* L. biodiesel and baseline diesel [20].

Table 4.1 Fuel properties of *Simarouba Glauca* L. and baseline diesel [20]

S. No.	Properties	Standard	Range	Simarouba biodiesel	Baseline diesel
1	Kinematic viscosity (Cst) at 40 °C	ASTMD445	1.9–6.0	4.7	1.3–2.4
2	Flash point (°C)	ASTM D93	>130	151	52–96
3	Density (kg/m)	ASTM D4062	870–900	865	832–850
4	Calorific value (MJ/kg)	ASTM D240	–	37.93	45.5
5	Cloud point (°C)	IS:1448	–3 to 12	25	–40
6	Pour point (°C)	IS:1448	–5 to 0	13	–40

4.2 Experiment Methodology

The main objective of the current research work is to analyze the performance parameters of CI engine powered with blended biodiesel fuel at different load conditions. An experimental test rig is developed to undertake the thermal performance evaluation and emission characteristic evaluation, at injection pressure 220 bar, using 5%, 10%, 15%, and 20% biodiesel blends under different load conditions. Figure 4.1 shows the engine test rig (actual and schematic diagram) used in the current research work. The engine specification and operating conditions are presented in Table 4.2.

4.3 Results and Discussion

Figure 4.2 presents the variation of BTE of the engine as a function of load % for different blend % of *S. Glauca* L. oil in the diesel. The BTE of the engine increases with increase in load, and this trend was common for all % of blending. The net heat loss reduces as the engine runs at higher loads, resulting in increase in BTE. At 25% load condition, the highest BTE of 21% was observed for the fuel with 5% blending of *S. Glauca* L. oil in diesel. At 50% load condition, the BTE increases with augment in blend %, reaching maximum 32% at 15% blend condition and then drops slightly to 31% for further increase in blend % of *S. Glauca* L. oil. When load increases to 70%, B15 gets highest BTE of over 37.8%, and B20 has least of 37.3%; however, all these blends have greater BTE than diesel, which means on part load condition biodiesel has better performance than diesel. Now for full load condition, B15 has 40% efficiency compared to diesel BTE of 38%.

Figure 4.3 presents the effect of blend % and load % on the BSFC of the engine. The BSFC of the engine running at diesel fuel was observed to be more as compared to the blended fuel for all load conditions, except at full load. At full load condition, the maximum BSFC was observed for the diesel fuel blended with 5% *S. Glauca* L.

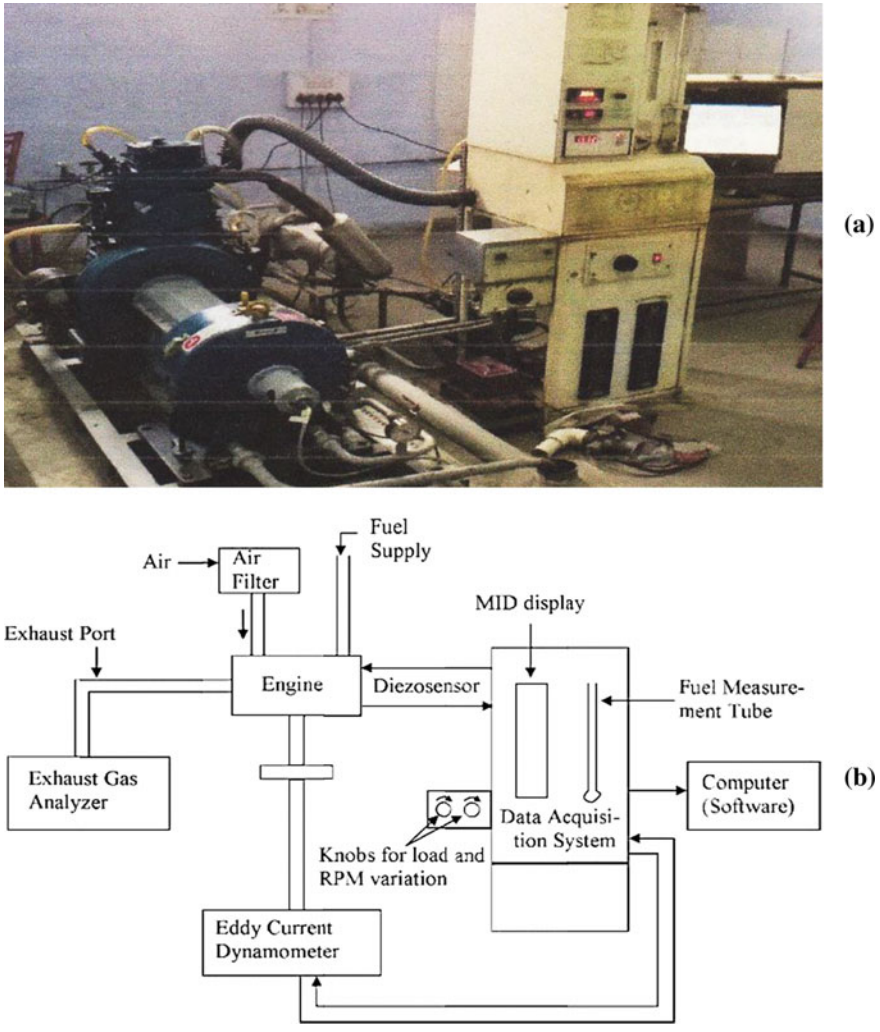


Fig. 4.1 Experimental test rig

oil. It can be clearly seen from the figure that the BSFC decreases with increase in load % of the engine, irrespective of the blend condition of the fuel. At 25% load condition, diesel has highest BSFC and B15 blend has BSFC less than diesel, i.e., 17.62 MJ/kWh, but the highest among all blend strength. Increasing load to 50% shows entirely different readings, as B10 has highest BSFC of 11.91 MJ/kWh which is less as comparative to diesel's 12.48 MJ/kWh. Further, increasing the load to 75% shows comparative values of BSFC for each blend %; however, B15 has least value of 9.5 MJ/kWh, which proves to be most economical.

Table 4.2 Engine specification

Model	Kirloskar oil engines
Engine	Single-cylinder four-stroke naturally aspirated diesel engine
Bore/stroke/compression ratio	87.5 mm/110 mm/VCR
Rated power	3.5 kW at 1500 rpm
Dynamometer	Eddy current, water cooled
Load sensor	Load cell, type strain gauge, range 0–50 kg
Injection pressure	220 bar
Exhaust gas analyzer	Make-Indus Scientific Pvt. Ltd.
Software	ICEnginesoftV8.5 engine performance analysis software

Fig. 4.2 BTE versus load

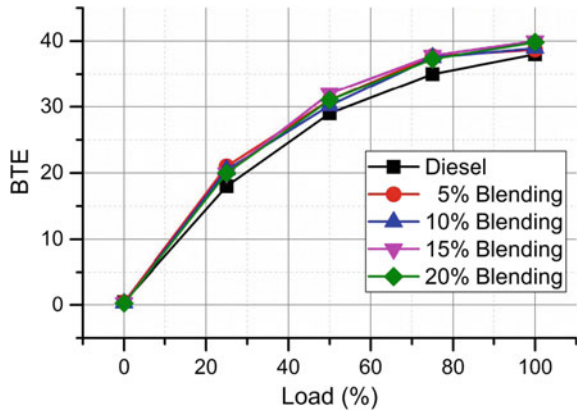
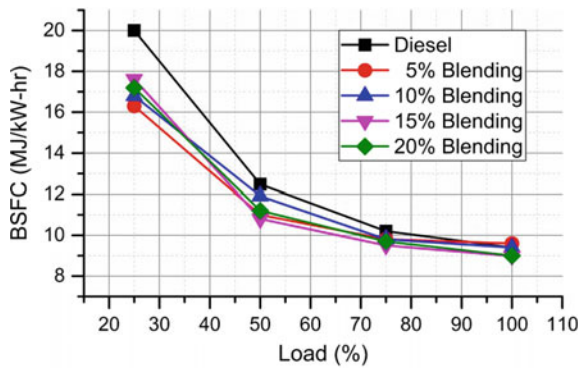


Fig. 4.3 BSFC versus load



The effect of blending % in the diesel fuel on the volumetric efficiency of the engine running at different load conditions is depicted in Fig. 4.4. At no load condition, the volumetric efficiency is almost similar for each blend %, and B05 has recorded maximum of 86.55%, while B20 has minimum volumetric efficiency of 83.3%. When 25% load is applied, slight decrease in volumetric efficiency was observed, where B05 has 85.48% compared to previous 86.55%. Further, for half load condition, B05 showed volumetric efficiency of 83.7% and almost same as B10 and B15, and B20 has least volumetric efficiency of 82.6% almost equal to diesel value, but when load increased to 75% B05 and B15 have almost same volumetric efficiency of 82.3% which was more than diesel value, and B10 and B20 have same volumetric efficiency of 81%, which is also greater than diesel value. On full load condition, slightly noticeable decrement exists for every blend strength except B05, which has maximum volumetric efficiency of 81.2% for B15—it is almost 80% while other blends have less volumetric efficiency. From above discussion, it is clear that there is no considerable effect of load variation on volumetric efficiency and no considerable effect of blend strength too. However, B05 and B15 have throughout better volumetric efficiency at different load conditions.

Along with performance, data emission analysis is also important, of which NO_x emission is one of the key constituents. Figure 4.5 shows variation of NO_x emission as a function of load and blend strength. Minimum NO_x emission was observed at no load condition for all blend strengths. The NO_x emission increases with augment in the % load. At 25% load condition, the diesel fuel has least NO_x emission of 126 ppm and B20 has maximum of 142 ppm NO_x emission among all blend strengths. At each load condition, diesel fuel is having least NO_x emission among their counterparts. It was also observed that the NO_x emission increases as the blend % of *S. Glauca* L. oil is increased, and this trend was common at all load conditions. The highest NO_x emission of 613 ppm was observed for 20% blended fuel when the engine runs at full load, i.e., 100% load condition. NO_x emission cannot be directly related to blend strength. It completely depends upon residual gases present and exhaust gas temperature.

Fig. 4.4 Volumetric efficiency versus load

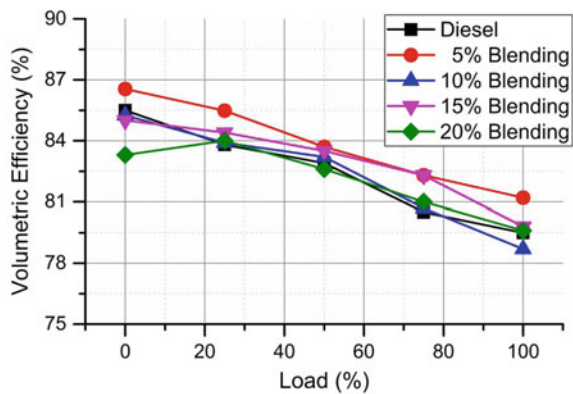


Fig. 4.5 NO_x emission versus load

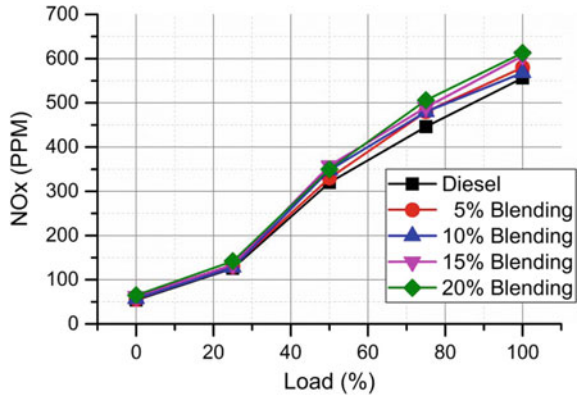


Fig. 4.6 CO₂ emission versus load

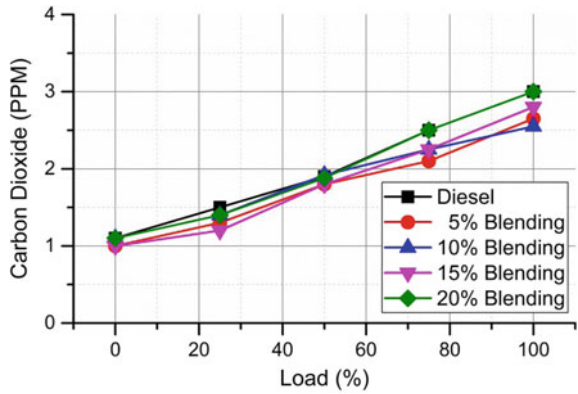
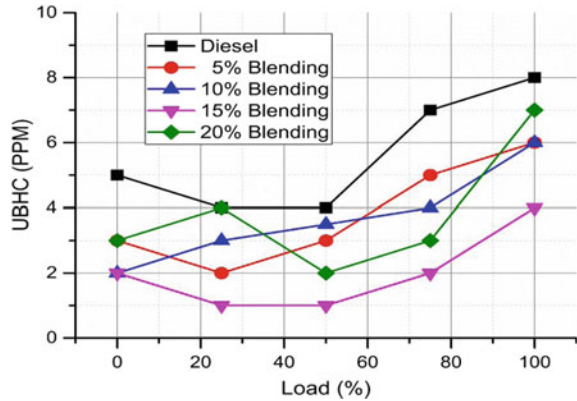


Figure 4.6 presents the variation in CO₂ emission with the load and blend strength of the fuel. It is well known that amount of CO₂ in exhaust gases increases with load increments which is actually a direct reconciliation of increased fuel consumption which can be easily compared with Fig. 4.3. Emission of CO₂ can be controlled by amount of fuel injected. At no load condition, each fuel has almost same CO₂ emission of approx. 1 ppm. The CO₂ emission increases with increase in load irrespective of the blend strength of the biodiesel fuel. The CO₂ emission was observed to have slight decrease as the blend strength increases up to 15%, followed by a slight increase for further increase in blend strength, i.e., for 20% blended fuel. B15 fuel was observed to have least emission of 1, 1.2, 1.8, 2.25, and 2.8 ppm at 0, 25%, 50%, 75%, and 100% load conditions, respectively.

UBHC is the indication of direct wastage of energy. Figure 4.7 presents the effects of load and blend strength of fuel on the UBHC in the exhaust of the engine. A general trend of increasing the UBHC was observed as the load increases from 0 to 100%. At no load condition, diesel fuel showed highest UBHC in the exhaust gases. For diesel fuel, the UBHC quantity decreases as the load was increased from 0 to 25%

Fig. 4.7 UBHC emission versus load



and then became stable up to 50% of the load followed by an increase in UBHC emission with further increase in load. The fuel with 15% blend of *S. Glauca* L. oil showed better result as compared to the counterparts, where the least quantity of UBHC was observed for all load conditions. The best combination of load and blend strength was observed as 25–50% load with 15% blend strength, respectively, to get minimum UBHC.

The results obtained in the study clearly revealed that the load and blend strength significantly affect the performance and exhaust emission of the CI engine. The *S. Glauca* L. oil is having all the potential to serve as an alternate to conventional diesel fuel. High amount of oxygen present in the biodiesel leads to the improvement in the performance characteristics of the engine. Moreover, the amount of carbon dioxides, UBHC, etc., in the exhaust gas emission can be controlled up to a considerable amount using *S. Glauca* L. oil. The oxygen which presents in *S. Glauca* L. oil helps in complete combustion of fuel, resulting in higher thermal efficiency of the engine. The density of *S. Glauca* L. oil is higher than the diesel fuel, due to which a comparatively lower BSFC is obtained using blended fuel.

4.4 Conclusion

The result obtained through analysis of CI engine fueled with different blends of *S. Glauca* L. at different load conditions showed that these factors have considerable impact on the engine performance and exhaust emission. The CO₂ emission first decreased with increase in blend strength and then increased on an average but never gets higher than that of diesel. BTE for blend strength was always higher than diesel fuel. B5 and B15 had similar and highest BTE among all blend strengths. There was significant decrease in BSFC among biodiesel blend as compared to the diesel fuel. B15 had shown minimum BSFC among all fuels including diesel. Similar result was seen in case of volumetric efficiency. Use of biodiesel reduced the HC emission by

26% at full load, but diesel had recorded least emission at part load. Low BSFC and high BTE are key indication of good engine fuel which is recorded in case of B15 biodiesel blend, consequently having lower emission as compared to diesel were observed for same blend strength. On a single platform, the best overall performance and emission characteristic were observed for B15 blend fuel.

References

1. Anenberg, S.C., Miller, J., Minjares, R., Du, L., Henze, D.K., Lacey, F., Malley, C.S., et al.: Impacts and mitigation of excess diesel-related NO_x emissions in 11 major vehicle markets. *Nature* **545**(7655), 467 (2017)
2. Singh, D., Sharma, D., Soni, S.L., Sharma, S., Kumari, D.: Chemical compositions, properties, and standards for different generation biodiesels: a review. *Fuel* **253**, 60–71 (2019)
3. Keera, S.T., El Sabagh, S.M., Taman, A.R.: Castor oil biodiesel production and optimization. *Egypt. J. Petrol.* **27**(4), 979–984 (2018)
4. Samad, A.T.P., Putri, D.N., Perdani, M.S., Utami, T.S., Arbianti, R., Hermansyah, H.: Design of portable biodiesel plant from waste cooking oil. *Energy Procedia* **153**, 263–268 (2018)
5. Hasan, M.M., Rahman, M.M.: Performance and emission characteristics of biodiesel–diesel blend and environmental and economic impacts of biodiesel production: a review. *Renew. Sustain. Energy Rev.* **74**, 938–948 (2017)
6. Ghazali, W.N.M.W., Mamat, R., Masjuki, H.H., Najafi, G.: Effects of biodiesel from different feedstocks on engine performance and emissions: a review. *Renew. Sustain. Energy Rev.* **51**, 585–602 (2015)
7. Hoekman, S.K., Broch, A., Robbins, C., Ceniceros, E., Natarajan, M.: Review of biodiesel composition, properties, and specifications. *Renew. Sustain. Energy Rev.* **16**(1), 143–169 (2012)
8. Gumus, M.: A comprehensive experimental investigation of combustion and heat release characteristics of a biodiesel (hazelnut kernel oil methyl ester) fueled direct injection compression ignition engine. *Fuel* **89**(10), 2802–2814 (2010)
9. Ruhul, A.M., Kalam, M.A., Masjuki, H.H., Alabdulkarem, A., Atabani, A.E., Rizwanul Fattah, I.M., Abedin, M.J.: Production, characterization, engine performance and emission characteristics of *Croton megalocarpus* and *Ceiba pentandra* complementary blends in a single-cylinder diesel engine. *RSC Adv.* **6**(29), 24584–24595 (2016)
10. Monirul, I.M., Masjuki, H.H., Kalam, M.A., Mosarof, M.H., Zulkifli, N.W.M., Teoh, Y.H., How, H.G.: Assessment of performance, emission and combustion characteristics of palm, jatropha and *Calophyllum inophyllum* biodiesel blends. *Fuel* **181**, 985–995 (2016)
11. Sahoo, P.K., Das, L.M.: Combustion analysis of Jatropha, Karanja and Polanga based biodiesel as fuel in a diesel engine. *Fuel* **88**(6), 994–999 (2009)
12. Basha, S.A., Raja Gopal, K., Jebaraj, S.: A review on biodiesel production, combustion, emissions and performance. *Renew. Sustain. Energy Rev.* **13**(6–7), 1628–1634 (2009)
13. Tarabet, L., Loubar, K., Lounici, M.S., Khiari, K., Belmrabet, T., Tazerout, M.: Experimental investigation of DI diesel engine operating with eucalyptus biodiesel/natural gas under dual fuel mode. *Fuel* **133**, 129–138 (2014)
14. Adewale, P., Dumont, M.-J., Ngadi, M.: Recent trends of biodiesel production from animal fat wastes and associated production techniques. *Renew. Sustain. Energy Rev.* **45**, 574–588 (2015)
15. Bhuiya, M.M.K., Rasul, M.G., Khan, M.M.K., Ashwath, N., Azad, A.K.: Prospects of 2nd generation biodiesel as a sustainable fuel—part: 1 selection of feedstocks, oil extraction techniques and conversion technologies. *Renew. Sustain. Energy Rev.* **55**, 1109–1128 (2016)
16. Fadhil, A.B., Al-Tikrity, E.T.B., Albadree, M.A.: Biodiesel production from mixed non-edible oils, castor seed oil and waste fish oil. *Fuel* **210**, 721–728 (2017)

17. Yunus, S., Rashid, A.A., Abdullah, N.R., Mamat, R., Latip, S.A.: Emissions of transesterification Jatropha-palm blended biodiesel. *Procedia Eng.* **68**, 265–270 (2013)
18. Jena, P.C., Raheman, H., Kumar, G.V.P., Machavaram, R.: Biodiesel production from mixture of mahua and simarouba oils with high free fatty acids. *Biomass Bioenergy* **34**(8), 1108–1116 (2010)
19. Mishra, S.R., Chaterjee, S., Mohanty, M.K., Senapati, M.R., Panigrahi, N.: Biodiesel production from *Simarouba glauca* oil using CaO and KOH catalysts: a comparative study. *Int. J. Sci. Eng. Res.* **4**(12), 147–151 (2013)
20. Dash, A.K., Pradhan, R.C., Das, L.M., Naik, S.N.: Some physical properties of simarouba fruit and kernel. *Int. Agrophysics* **22**(2), 111 (2008)

Chapter 5

Wear Characteristics of Silica-Reinforced Rice Husk-Epoxy Hybrid Bio-composite



Neeraj Bisht and P. C. Gope

Abstract This paper studies the effect of addition of rice husk ash on the wear characteristic of rice husk-reinforced epoxy-based composites. Rice husk ash is the product of thermal degradation of rice husk. The rice husk ash is 90% silica, a hard material. In a previous paper, the rice husk was optimized for mechanical properties. The effect of pre-treatment with NaOH was also studied. In continuation of the previous work, rice husk ash was added as a second reinforcement. Tribological studies are important as there is excessive waste of material due to wear and tear. Silica being a hard material can improve the wear characteristics, and so silica derived from natural resource was used for the purpose. It was observed that the wear characteristics improved due to rice husk ash addition; however, for low level of filling at higher filling level, the wear life started deteriorating. From the SEM micrographs, it is seen that at higher filler level, the adhesion between different constituents was improper resulting in decreased wear characteristics. However, rice husk ash is a viable option for improving wear performance.

Keywords Rice husk ash · Epoxy · Wear rate

5.1 Introduction

The worldwide production of rice husk is approximately 700 million tonnes [1], 22% of it is husk [2], making it an abundant natural resource. The rice husk has no appreciable use. However, it can be a cheap source of fibre in raw form (chopped or grounded) [3] or by-products obtained by its thermal degradation. Natural fibres are lighter, have higher filling level and economical, are bio-degradable, corrosive resistant, among others (sometimes free) [3, 4]. Rice husk in its various forms has been extensively used by scientists in development of bio-composites in the past few years.

Rice husk has been used extensively with almost all the polymers like polypropylene, polyethylene, polyurethane epoxy to name a few. There was an improvement

N. Bisht (✉) · P. C. Gope

Department of Mechanical Engineering, College of Technology, GBPUAT, Pantnagar, India
e-mail: neerajbisht30@gmail.com

© Springer Nature Singapore Pte Ltd. 2020

I. Singh et al. (eds.), *Advances in Materials Engineering and Manufacturing Processes*,
Lecture Notes on Multidisciplinary Industrial Engineering,

https://doi.org/10.1007/978-981-15-4331-9_5

in mechanical strength but limited to lower filling level. The reason behind this was twofold, tendency of rice husk to agglomerate and the opposing nature of polymers and rice husk. This, however, can be improved. The solution lies in the surface modification of rice husk.

Various surface modification techniques of rice husk have been proposed. The methods can be categorized as compatibilizers [5, 6], mercerization [7], plasma treatment [7], electron beam irradiation [8] and chemical treatment [9–13]. All the techniques mentioned improved the adhesion between the constituents.

Further improvement in properties can be done by hybridization that is adding more than one fibre as has been done in numerous previous studies.

The impact of surface treatment on the tribological characteristics has not been studied much. According to estimates, annual loss due to wear for industries in the USA is 1–2% of GDP [14]. So taking into account the losses that are accrued due to wear the study of this aspect becomes very important.

The rice husk ash is 92% silica which is known to be a hard abrasive material. Keeping in mind the abrasive nature of silica, it was derived from rice husk ash by thermal degradation and added as the second reinforcement to the already optimized modified rice husk-epoxy bio-composite.

Abrasive wear measurements on composites prepared by RH as fibre and matrix polyvinyl chloride were conducted [15]. As the sliding distance increased, the specific wear rate decreased. The effect of increasing reinforcement on the specific wear rate was not beneficial; there was not proper adhesion between the filler and the matrix material PVC present. For all percentage of reinforcement, the wear rate was higher compared to pure epoxy. However, modification of rice husk by using maleic anhydride as a compatibilizer was seen to be beneficial. The wear strength improved with compatibilizers; it was, however, low compared to pure epoxy.

The wear character of RH-filled composites based on epoxy was studied [16], and by increasing sliding distance the wear rate decreased. With the percentage reinforcement, increasing the wear rate for up to 10% decreased the RH loading in comparison to pure epoxy. For further reinforcement, it increased. Further, treating rice husk with benzoyl chloride improved the compatibility between the two, thereby decreasing the wear and the specific wear rate.

In another study [17], the jute fibre-based composite for wear characteristic was studied. Use of maleic anhydride grafted polypropylene was done, and wear characters of the bio-composite are enhanced significantly.

The tribological properties show improvement due to NaOH treatment [18]. This was attributed to improved adhesion. However, excessive treatment resulted in deterioration of fibre, thereby increasing the wear rate.

5.2 Material Preparation

5.2.1 Materials

CY-230 and HY-951 were used as matrix. Rice husk procured locally was the reinforcing agent. In the beginning, rice husk was thoroughly washed in running water to remove impurities and then dried under sun to make it moisture free after which it was grounded. By the sieving process, particles of 125 microns (ASTM 120) were obtained and used for further research.

5.2.2 Preparation of Rice Husk Ash

Silica from rice husk can be obtained by different processes. The process utilized [19] can be summarized in following steps:

1. Rice husk was soaked in water to remove foreign materials.
2. 0.4 M solution of HCl was prepared; 10 g cleaned husk was mixed in 100 mL of the solution and was further boiled for 30–45 min at 100–105 °C. Rice husk was then washed thoroughly to remove traces of HCl.
3. Then, it was soaked in an oven at 110 °C for 4 h.
4. The treated husk thus obtained is incinerated in an electric furnace at 600 °C for 6 h after which silica was obtained as white ash. Its shape is similar to the shape of the husk but much smaller in size.

5.2.3 Preparation

12-mm-thick Perspex sheets were used to prepare moulds. Using a mechanical stirrer, different weight percentages (wt%) of RHA fibre (0.5, 1 and 2 wt%) and epoxy resin were mixed. The solution obtained was kept in the furnace at a temperature of 90 ± 10 °C for two hours. Then, the whole solution was taken out and air cooled to 45 °C, and the hardener HY-951 (9 weight per cent) was mixed immediately [20]. The viscous solution obtained after addition of hardener is then poured into different moulds for sample preparation.

5.2.4 Tribological Testing

Plinth Wear and Friction Machine which is a “pin and disc machine” was used for the experiments. The lathe-based machine is driven by a 750 W three-phase motor.

The sample pins of 8 mm diameter and length 53 mm were prepared and rotated against a hardened steel disc with a revolution diameter of 43 mm.

5.2.5 Wear Rate Measurement

The test speed was 237 revs/min at 10 N load. The pins were rotated against a steel disc for 2000, 4000, 6000, 8000 and 10,000 number of revolutions, and corresponding sliding distance was evaluated. The formulae for the calculation are as follows:

$$\text{Sliding distance } x = 0.251 n = 0.00419 Nt \quad (1)$$

where

n	Total revolutions
N	Disc speed, rev/min
t	Duration of run
Radius of test track	40 mm

After each revolution, the weight loss was recorded. The specific wear rate was calculated according to the formula

$$K_0 = \frac{W}{\rho LD} \quad (2)$$

where W = weight loss in kg, ρ is density in kg/m^3 , L is the load in Newton and D is sliding distance in metres.

5.2.6 SEM Studies

To study the wear phenomenon and mechanism, morphological studies of worn samples were carried out. The images are obtained through microscopic investigation with scanning electron microscope. Square samples were cut from the worn-out material and gold coated to observe the SEM images. An accelerated voltage of 10 kV was used.

5.3 Results and Discussions

Figure 5.1 depicts the variation of specific wear rate with sliding distance and RHA content. It has been observed that RHA particles have excellent abrasive properties so RHA addition would improve wear strength. This result can be observed in

Fig. 5.1 Specific wear rate for treated fibres for different level of RHA addition

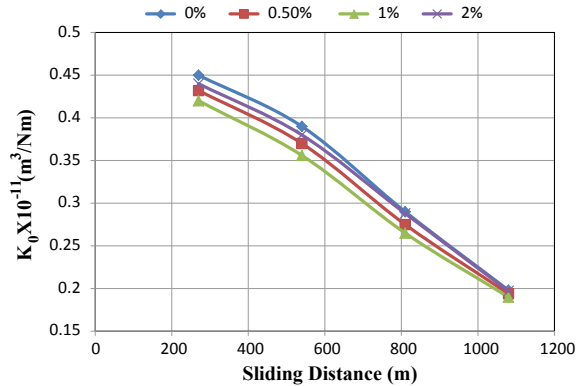


Fig. 5.1 in which it is observed that as the RHA content increased, the wear rate decreased, i.e. the resistance to wear improves. Also it can be seen that with increase in the sliding distance, specific wear rate decreases and for sliding distance greater than 1000 m, the specific wear rate for all the composites becomes approximately equal. The improvement in wear characteristics is because silica is known to be an abrasive material and hence improves abrasive properties. For addition of 1% RHA, the improvement was about 12% while that for 0.5%, it was 6%. However, further addition results in increase in wear rate; it was however still lower than non-RHA bio-composite. This can be due to the high viscosity of the resulting mixture due to which the curing becomes difficult. The RHA has a very low density, and hence, its filling at higher levels poses problems.

From the SEM images of worn surfaces of the samples, it can be observed that as the rice husk ash loading increases, the matrix cracking and surface damage are less pronounced. Figure 5.2a–d represent the micrographs of 0, 0.5, 1 and 2% Si, respectively. From Fig. 5.2b it is seen that RHA has been mixed well with the RH and matrix, and thus, it becomes hindrance to the movement of dislocations thereby increasing tensile strength. From Fig. 5.2d, a void of size approximately 500 micrometre is formed because at higher mixing ratio, the mixture becomes more viscous and thus poses difficulties in casting. It also shows that at higher mixing ratio of RHA to RH, proper mixture is not formed which results in decrease in mechanical strength.

5.4 Conclusions

1. Rice husk ash can be an alternative to increase the wear strength of the composites.
2. Higher filling levels cannot be achieved due to the high viscosity of the mixture.
3. The addition of rice husk ash in tandem with rice husk pre-treatment can be very effective for producing highly wear resistant bio-composites.

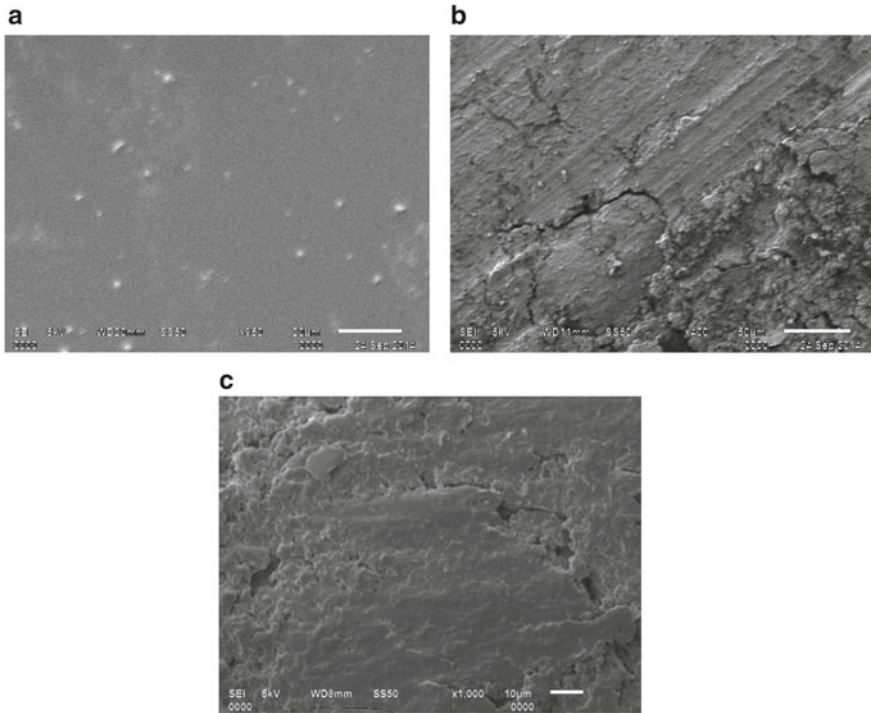


Fig. 5.2 SEM image of worn-out surfaces of different samples—**a** pure epoxy **b** 1 wt% rice husk ash and **c** 2 wt% rice husk

References

1. Trade and Markets Division.: Food and Agriculture Organization of the United Nations. *FAO Rice Market Monitor. Bull* (2010)
2. Beagle, E.C.: Rice-husk conversion to energy. *FAO Agric. Serv. Bull.* (1978)
3. Ismail, H., Nasir, S.M.: Dynamic vulcanization of rubber wood-filled polypropylene/natural rubber blends. *Polym. Test.* **20**, 819–824 (2001)
4. Oksman, K., Clemons, C.: Mechanical properties and morphology of impact modified polypropylene–wood flour composites. *J. Appl. Polym. Sci.* **67**, 1503–1513 (1997)
5. Petchwattana, N., Covavisaruch, S., Chanakul, S.: Mechanical properties, thermal degradation and natural weathering of high density polyethylene/ rice hull composites compatibilized with maleic anhydride grafted polyethylene. *J. Polym. Res.* **19**, 1–9 (2012)
6. Yang, H.-S., Kim, H.-J., Park, H.-J., et al.: Effect of compatibilizing agents on rice-husk flour reinforced polypropylene composites. *Compos. Struct.* **77**, 45–55 (2007)
7. Nguyen, M.H., Kim, B.S., Ha, J.R. et al.: Effect of plasma and NaOH treatment for rice husk/PP composites. *Adv. Compos. Mater.* **20**, 435–442 (2011)
8. Ahmad, I., Lane, C.E., Mohd, D.H. et al.: Electron-beam-irradiated rice husk powder as reinforcing filler in natural rubber/high-density polyethylene (NR/HDPE) composites. *Compos. Part B* **43**, 3069–3075 (2012)
9. Rozman, H.D., Lee, M.H., Kumar, R.N., et al.: The effect of chemical modification on rice husk with Glycidyl Methacrylate on the mechanical and physical properties of rice husk- polystyrene composites. *J. Wood Chem. Technol.* **20**, 93–109 (2000)

10. Santiago, R., Ismail, H., Hussin, K.: Effects of acetic anhydride on the properties of polypropylene(PP)/recycled acrylonitrile butadiene(NBRr)/rice husk powder(RHP) composites. *Polym. Plast. Technol. Eng.* **51**, 1505–1512 (2012)
11. Huang, G.: Tensile behaviours of the coir fibre and related composites after NaOH treatment. *Mater. Des.* **30**, 3931–3934 (2009)
12. Rout, J., Misra, M., Tripathy, S.S., et al.: The influence of fibre treatment on the performance of coir-polyester composites. *Compos. Sci. Technol.* **63**, 1303–1310 (2001)
13. Rahmana, M.M., Khan, M.A.: Surface treatment of coir (*Cocosnucifera*) fibres and its influence on the fibresphysico-mechanical properties. *Compos. Sci. Technol.* **67**, 2369–2376 (2007)
14. Zum Gahr, K.H.: *Microstructure and Wear of Materials*. Tribology Series. Vol. 10, Elsevier (1987). ISBN 0-444-42754-6
15. Chand, N., Sharma, P., Fahim, M.: Tribology of maleic anhydride modified rice-husk filled polyvinylchloride. *Wear* **269**, 847–853 (2010)
16. Majhi, S., Samantarai, S.P., Acharya, S.K.: Tribological behaviour of modified rice husk filled epoxy composite. *Inter. J. Sci. Eng. Res.* **3**(6) (2012)
17. Chand, N., Dwivedi, U.K.: Effect of coupling agent on abrasive wear behaviour of fibre-reinforced polypropylene composites. *Wear* **261** 1057–1063 (2006)
18. Bisht, N., Gope, P.C.: Wear characteristics of untreated and alkali-treated rice husk-epoxy bio-composite. In: Singh, I., Bajpai, P., Panwar, K. (eds.) *Trends in Materials Engineering. Lecture Notes on Multidisciplinary Industrial Engineering*. Springer, Singapore (2019)
19. Ahmed, K., Nizami, S.S., Riza, N.Z.: Reinforcement of natural rubber hybrid composites based on marble sludge/Silica and marble sludge/rice husk derived silica. *J. Adv. Res.* **5**(2), 165–173 (2013)
20. Singh, V.K., Gope, P.C.: Silica-styrene-butadiene rubber filled hybrid composites: experimental characterization and modeling. *J. Reinf. Plast. Compos.* **29**, 2450–2468 (2010)
21. Razavi Nouri, M., Jafarzadeh-Dogouri, F., Oromiehie, A. et al.: Mechanical properties and water absorption behaviour of chopped rice husk filled polypropylene composites, Iran. *Polym. J.* **15**, 757–766 (2006)

Chapter 6

Numerical Analysis of Thermo-Physical Properties Using Disc Blade Inserts with $\text{Al}_2\text{O}_3/\text{TiO}_2$ Water-Based Nanofluids



Jaspreet Kaur and Satyendra Singh

Abstract This study represents a computational investigation on achieving intensified heat transfer rate and TPF by inserting disc blade inserts having different volume fraction of nanofluids. The simulation for examining the performance is carried out in single tube heat exchanger by using $\text{Al}_2\text{O}_3/\text{TiO}_2$ water-based nanofluids with 0%, 1%, 2%, 3%, 4% and 5% concentrations. In this analysis, test section length is 1200 mm, heat flux is 1000 W/m^2 and Reynolds number is varying from 5000 to 13,000. It has been observed that the highest enhancement in heat transfer rate is 5.026 and 4.882 times in case of Al_2O_3 and TiO_2 , respectively, each having 5% concentration. The value of overall thermal performance factor (TPF) increased up to 2.225 and 2.167 times in case of Al_2O_3 and TiO_2 , respectively, each having 5% concentration.

Keywords Disc blade inserts · Nanofluids · Thermal performance factor

Nomenclature

A	Area of pipe, m^2
A_s	Surface area of pipe, m^2
C_p	Specific heat capacity, J/kg-K
D	Hydraulic diameter, mm
f	Friction factor
f_s	Friction factor for smooth tube
h	Average heat transfer coefficient, W/m-K
k	Thermal conductivity, W/m-K
L	Length of test section, mm
m	Mass flow rate, kg/s

J. Kaur (✉) · S. Singh
B.T. Kumaon Institute of Technology, Dwarahat, Uttarakhand, India
e-mail: jaspreetkauratwal1994@gmail.com

S. Singh
e-mail: ssinghiitd@gmail.com

© Springer Nature Singapore Pte Ltd. 2020
I. Singh et al. (eds.), *Advances in Materials Engineering and Manufacturing Processes*,
Lecture Notes on Multidisciplinary Industrial Engineering,
https://doi.org/10.1007/978-981-15-4331-9_6

Nu_s	Nusselt number for smooth tube
Nu	Nusselt no
Pr	Prandtl no
ΔP	Pressure drop, Pa
Re	Reynolds no
T_{fm}	Fluid mean temp, K
T_{wm}	Wall mean temp, K
T_i	Inlet air temp, K
T_o	Outlet air temp, K
TPF	Thermal performance factor

6.1 Introduction

Heat transfer is a process of transferring internal energy from one substance to another substance which takes place due to temperature difference. Heat transfer enhancement using different insert geometries is becoming a popular area of interest for researchers. Thermal conductivity of fluid plays major role in heat transfer. To improve the thermal conductivity of fluid nanosized particles are used with base fluid. Different types of insert geometries [1–3] used for creating turbulence in fluid stream such as helical tapes, modified twisted tape (classic, notched, jagged, perforated) and louvered strip inserts etc. Many researchers have investigated the thermal properties using helically coiled tube, shell and helical tube heat exchangers [4, 5] for providing more reliable and efficient heat transfer rate from thermal systems. Experimental investigation with forced convection had been performed taking different nanofluids [6, 7] such as dilute CuO/water and TiO₂/water in circular tube. Multi-channel and square mini channel heat exchanger used with Al₂O₃/water-based nanofluid [8, 9] by taking different concentrations of nanofluids and the result showed that thermal performance enhances with higher concentration of nanoparticle. Numerical and experimental analysis done with compact minichannel, helical baffled heat exchanger combined with 3-D finned tube [10, 11] for investigating the thermo-physical properties. Laminar flow used in coaxial heat exchanger to study heat transfer properties of aqueous carbon nanotubes [12] and coiled wire inserts used with horizontal tube for enhances the overall performance of heat exchangers [13].

6.2 Numerical Method and Validation

6.2.1 Governing Equation

The problem was presumed to be incompressible, Newtonian, 3-D turbulent and steady flow. Following equations are shown as

Continuity equation:

$$\frac{\partial u_i}{\partial x_i} = 0. \quad (6.1)$$

Momentum equation:

$$\rho u_i \frac{\partial u_j}{\partial x_i} = -\frac{\partial \rho}{\partial x_i} + \frac{\partial}{\partial x_i} \left(\frac{\mu \partial u_j}{\partial x_i} \right). \quad (6.2)$$

Energy equation:

$$\rho C_p \left(u_i \frac{\partial T}{\partial x_i} \right) = k \left(\frac{\partial^2 T}{\partial x_i^2} \right). \quad (6.3)$$

6.2.2 Boundary Conditions

In this present work, Re varies from 5000 to 13,000. No-slip boundary condition is set on the wall. Hydrodynamic and fully developed flow is computed by means of constant inlet temperature that is kept equal to 300 K. Simulation is carried out in varying velocity and constant uniform flux. Al₂O₃/TiO₂ water-based nanofluids are carried as working fluid, and the other properties are supposed to be constant. A constant pressure condition was set with zero gauge pressure at tube's outlet.

6.2.3 Data Processing and Parameters

Reynolds number, friction factor, Nusselt number and thermal performance factor are calculated as given below.

Reynolds number is determined by:

$$\text{Re} = \frac{\rho v D}{\mu}. \quad (6.4)$$

Friction factor is defined as:

$$f = \frac{\Delta P}{\left(\frac{L}{D}\right) \left(\frac{\rho * v^2}{2}\right)}. \quad (6.5)$$

at transfer coefficient is computed by:

$$h = Q_{\text{conv}}/A_s(T_{\text{wm}} - T_{\text{fm}}). \quad (6.6)$$

Nusselt number is determined by:

$$\text{Nu} = \frac{hD}{k}. \quad (6.7)$$

Thermal performance factor is gained by:

$$\text{TPF} = \frac{\left(\frac{\text{Nu}}{\text{Nu}_s}\right)}{\left(\frac{f}{f_s}\right)^{\frac{1}{3}}}. \quad (6.8)$$

We use standard correlation for calculating friction factor and Nusselt number for smooth tube.

Blasius equation:

$$f_s = 0.316 \times \text{Re}^{-0.25} \quad (6.9)$$

Dittus–Boelter equation:

$$\text{Nu}_s = 0.023 \times \text{Re}^{0.8} \text{Pr}^{0.4} \quad (6.10)$$

6.2.4 Numerical Methodology

Selection criterion for turbulence model has important effect on numerical simulation. Three-dimensional CFD software FLUENT 16.0 was selected for the simulation. Solver-based FVM has been selected for this simulation. Cut cell method with coarse relevance centre is used for meshing as shown in Fig. 6.1. For discretizing the continuity equation, momentum equation and energy equation, second-order upwind scheme was used. Further, solutions for continuity equation, momentum equation and energy equations have been considered to converge when the values of residuals were less than 10^{-6} . A famous turbulence method realizable model is used with standard wall functions.

6.2.5 Grid-Independence Test and Validation

To obtain the high computation precision, grid-independence test was done through GCI method. Grid-independence test was performed for different mesh resolutions

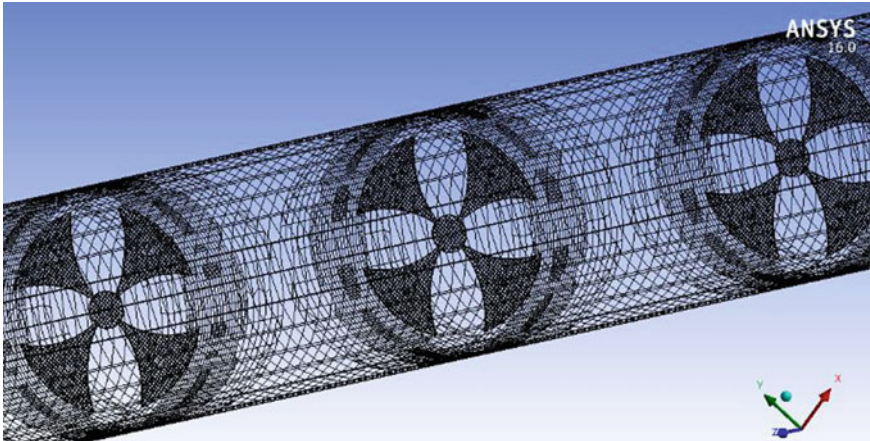


Fig. 6.1 Meshing of disc blade inserts

Table 6.1 Grid-independence test

Grid no.	Nu	$ \text{Nu}^{i+1} - \text{Nu}^i /\text{Nu}^{i+1}$	f	$ f^{i+1} - f^i /f^{i+1}$
39,652	222.74		0.123825	
62,517	314.62	0.29203	0.218593	0.43353
95,625	358.38	0.12210	0.375621	0.41804
349,683	446.7012	0.19771	0.439444	0.14523
1,192,437	447.921	0.00272	0.442632	0.00720

to gain a sensible grid having good correctness for different Nusselt number and friction factor. Table 6.1 shows that the difference in the Nusselt number and friction factor between grid number of 349,683 and 1,192,437 is about 0.27% and 0.72%, respectively, at Reynolds number 13,000. From results of GCI test, the grid system having 349,683 elements was taken for this simulation. To validate the accuracy of this method, we compare the value of Nusselt number and friction factor at fixed Reynolds number for smooth tube. Table 6.2 expressed that deviation in values is obtained from simulation with theoretical values.

6.2.6 Thermo-Physical Properties of Nanofluids

Thermo-physical properties of nanofluids at various volume fractions were calculated by using the following equations [14] and used for further analysis.

Thermal conductivity:

Table 6.2 Validation of Nu and friction factor in smooth tube

Re No.	Nu (ANSYS)	Nu (Dittus–Boelter eq.)	Error (%)	f (ANSYS)	f (Blasius eq.)	Error (%)
5000	48.0042	45.5740	5.0624	0.0399	0.0375	6.0150
7000	63.6291	59.65128	6.2515	0.0368	0.0345	6.2500
9000	76.3676	72.9349	4.4949	0.0350	0.0324	7.4285
11,000	89.1144	85.6358	3.9035	0.0330	0.0308	6.6667
13,000	101.8606	97.8805	3.9073	0.0316	0.0295	6.6455

$$k_{nf} = \frac{k_w [(k_{np} + 2k_w) + 2\phi(k_{np} - k_w)]}{[(k_{np} + 2k_w) - \phi(k_{np} - k_w)]} \quad (6.11)$$

where k_{np} is the thermal conductivity of the nanoparticle and k_w is the thermal conductivity of the water.

Dynamic viscosity:

$$\mu_{nf} = (1 + 2.5\phi)\mu_w \quad (6.12)$$

where μ_{nf} is the dynamic viscosity of nanofluid, μ_w is the dynamic viscosity of the water and ϕ is the volume fraction of nanoparticle.

Density:

$$\rho_{nf} = (1 - \phi)\rho_w + \phi\rho_{np} \quad (6.13)$$

where ρ_{nf} is the density of nanofluid, ρ_w is the density of base fluid and ρ_{np} is the density of nanoparticle.

Specific heat:

$$Cp_{nf} = \phi\rho_{np}Cp_{np} + (1 - \phi)\rho_wCp_w \quad (6.14)$$

where Cp_{nf} , Cp_{np} and Cp_w are the heat capacity of nanofluids, nanoparticles and water, respectively.

6.3 Results and Discussions

6.3.1 Effect on Heat Transfer

Four protruding blades are responsible for creating disturbance in the fluid domain. Hence, more turbulence is generated near the inserts. A small disc placed at centre also created turbulence in the path of fluid domain. It can be observed that the high

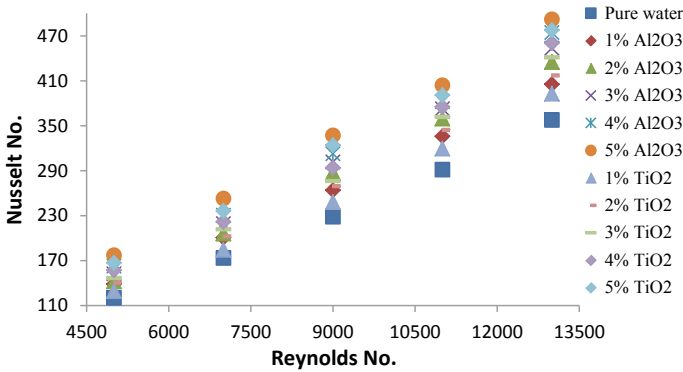


Fig. 6.2 Variation of Nu with Re

impingement of swirl flow and high range of temperature gradient can be taken to the enhanced value of Nu and vice versa. Nu significantly increases with the higher value of Re (see Fig. 6.2). Small concentration of nanofluid enhances the heat transfer rate significantly as it has high thermal conductivity. Result shows that about 5.026 and 4.882 times enhancement is obtained in heat transfer rate when 5% concentration of Al₂O₃ and TiO₂ nanofluids is used, respectively, at Re 13,000 as comparing to smooth tube.

6.3.2 Effect on Friction Factor

Friction factor shows an important aspect in enhancing the value of TPF. Therefore, less value of friction factor is preferred for better performance. Figure 6.3 illustrates that the flow resistance and friction factor value increase when the concentration

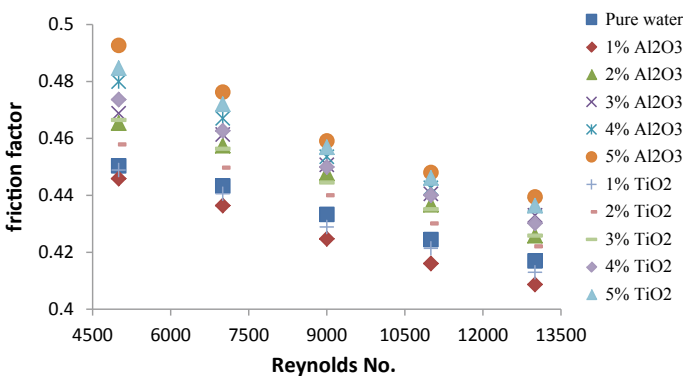


Fig. 6.3 Variation of friction factor with Re

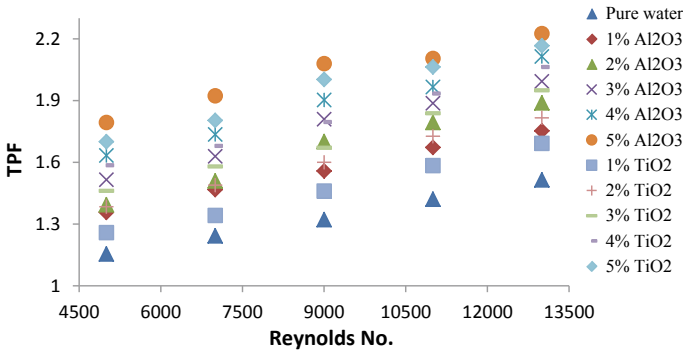


Fig. 6.4 Variation of Thermal performance factor with Re

of nanofluid enhances with fixed range of Re. The geometry of blade occupies less space in the fluid domain. So, the flow blockages decrease and lead to less pressure drop. Less value of friction factor is gained in the higher range of Reynolds number with 1% concentration of Al₂O₃ and TiO₂ nanofluids. This is approximately 12.11 and 11.94 times, respectively, as comparing to smooth tube.

6.3.3 Effect on Thermal Performance Factor

TPF depends on the value of heat transfer and friction factor. As the value of heat transfer enhances and friction factor decreases, the value of TPF significantly increases. On enhancing the concentration of nanofluids, there is increment in energy exchange due to unsymmetrical and uncertain movements of particles. Figure 6.4 shows that value of TPF increases with increase in the volume fraction of nanofluids and Re. Thermal performance factor has maximum value in higher range of velocity. Viscosity of nanofluid enhances as the volume fraction of nanofluid goes up, and it diminishes the fluid movement. It can be found that TPF increases up to 2.225 and 2.167 times in case of 5% concentration of Al₂O₃ and TiO₂ nanofluids, respectively.

6.4 Conclusions

Computational analysis for turbulent forced convection is carried out in circular tube heat exchanger having disc blade inserts with different concentrations of nanofluids. Graphs between Nu, friction factor and TPF with Reynolds number are plotted to compare the thermo-hydraulic properties of heat exchanger. Following conclusions can be made from the above numerical analysis:

1. As the concentration of nanofluids enhances, rate of heat transfer also goes up and vice versa. Largest value of heat transfer is obtained for the high range of Re as 13,000. Maximum increment in heat transfer is gained when 5% concentration of Al_2O_3 and TiO_2 nanofluids was used. It was found to be about 5.026 and 4.882 times enhancement in heat transfer.
2. As the concentration of nanofluid increases, there is an increment in friction factor and vice versa. As the value of Re enhances, friction factor's value reduces and vice versa. Minimum value of friction factor is obtained about 12.11 and 11.98 times as comparing to smooth tube having 1% concentration of Al_2O_3 and TiO_2 nanofluids, respectively.
3. For TPF, maximum performance factor is obtained at Reynolds number 13,000 in case of 5% concentration of nanofluid. Thermal performance factor enhances as the value of Reynolds number would increase. As the concentration of nanofluid increases, value of TPF also goes up. Maximum value of TPF is obtained as 2.225 and 2.167 times in case of Al_2O_3 and TiO_2 nanofluids, respectively.

References

1. Eiamsa-ard, S., Promvongse, P.: Enhancement of heat transfer in a tube with regularly-spaced helical tape swirl generators. *Sol. Energy* **78**, 483–494 (2005)
2. Rahimi, M., Shabaniyan, S., Alsairafi, A.: Experimental and CFD studies on heat transfer and friction factor characteristics of a tube equipped with modified twisted tape inserts. *Chem. Eng. Process.* **48**, 762–770 (2009)
3. Mohammed, H., Hasan, H.A., Wahid, M.: Heat transfer enhancement of nanofluids in a double pipe heat exchanger with louvered strip inserts. *Int. Commun. Heat Mass Transf.* **40**, 36–46 (2013)
4. Ferng, Y., Lin, W., Chieng, C.: Numerically investigated effects of different Dean number and pitch size on flow and heat transfer characteristics in a helically coil-tube heat exchanger. *Appl. Therm. Eng.* **36**, 378–385 (2012)
5. Jamshidi, N., Farhadi, M., Ganji, D., Sedighi, K.: Experimental analysis of heat transfer enhancement in shell and helical tube heat exchangers. *Appl. Therm. Eng.* **51**, 644–652 (2013)
6. Fotukian, S., Esfahany, M.: Experimental study of turbulent convective heat transfer and pressure drop of dilute CuO-Water nanofluid inside a circular tube. *Int. Commun. Heat Mass Transf.* **37**, 214–219 (2010)
7. Khedkar, R., Sonawane, S., Wasewar, K.: Heat transfer study on concentric tube heat exchanger using TiO_2 -water-based nanofluid. *Int. Commun. Heat Mass Transf.* **57**, 163–169 (2014)
8. Jwo, C., Jeng, L., Teng, T., Chen, C.: Performance of overall heat transfer in multi-channel heat exchanger by alumina nanofluid. *J. Alloy. Compd.* **504S**, S385–S388 (2010)
9. Kumar, S., Kothiyal, A.D., Bisht, S.M., Kumar, A.: Numerical analysis of thermal hydraulic performance of Al_2O_3 - H_2O nanofluid flowing through a protrusion obstacles square mini channel. *Case Studies Therm. Eng.* **9**, 108–121 (2017)
10. Ray, D., Das, D., Vajjha, R.: Experimental and numerical investigations of nanofluids performance in a compact minichannel plate heat exchanger. *Int. J. Heat Mass Transf.* **71**, 732–746 (2014)
11. Zhang, Z., Ma, D., Fang, X., Gao, X.: Experimental and numerical heat transfer in a helically. *Chem. Eng. Process.* **47**(9–10), 1738–1743 (2008)

12. Halelfadl, S., Estellé, P., Maré, T.: Heat transfer properties of aqueous carbon nanotubes nanofluids in coaxial heat exchanger under laminar regime. *Exp. Therm. Fluid Sci.* **55**, 174–180 (2014)
13. Akhavan-Behabadi, M., Kumar, R., Salimpour, M., Azimi, R.: Pressure drop and heat transfer augmentation due to coiled wire inserts during laminar flow of oil inside a horizontal tube. *Int. J. Therm. Sci.* **49**, 373–379 (2010)
14. Pourfayaz, F., Sanjarian, N., Kasaeian, A., Astaraei, R.F., Sameti, M., Nasirivatan, S.: An experimental comparison of SiO₂/water nanofluid heat transfer in square and circular cross-sectional channels. *J. Therm. Anal. Calorim.* **131**, 1577–1586 (2018)

Chapter 7

DC Electrical Conductivity and Magnetic Behaviour of Epoxy Matrix Composites Impregnated with Surface-Modified Ferrite Nanoparticles



Ashtosh Kumar Singh, M. G. H. Zaidi, and Rakesh Saxena

Abstract Epoxy-based ferrite nanoparticle composites are appropriate for various potential applications such as energy storage devices, sensors and electronic device. But ferrite nanoparticle epoxy composites have some limitations. To maintain homogeneous dispersion and interfacial bonding strength between FNs and the epoxy resin is main concern in devolvement of epoxy-based ferrite nanoparticle composites (FNECs). In present research, modified ferrite nanoparticles (MFNs) were prepared by surface modification of normal ferrite particles (FNs) by the use of APTS as surface modification agent. MFNs with different concentration (0.0–2.0 wt%) and FNs (2 wt%) used as a filler for fabrication of ferrite epoxy composites. 0, 0.5, 1.0, 1.5 and 2 wt% are denoted as cured epoxy, MFNEs-I, MFNEs-II, MFNEs-III and MFNEs-IV, respectively, whereas ferrite nanoparticle epoxy composites are denoted as FNEs. FT-IR spectral characterization was shown successfully the surface modification of FNs by APTS. Impact of ferrite dispersion in epoxy matrix after surface modification of ferrite nanoparticle on electrical and magnetic behaviour of composites has been investigated by DC conductivity and VSM test, respectively. Magnetization of MFNEs was increased by 24.29% with respect to FNEs, whereas DC electrical conductivity was increased by 38.77%, 31.25% and 15.88% at 1 V, 10 V and 100 V, respectively.

Keywords Ferrite nanoparticles · Nanomagnetic polymer composites · FT-IR · Magnetic behaviour · DC conductivity · Silane coupling

A. K. Singh (✉) · R. Saxena
Mechanical Engineering Department, G.B. Pant University of Agriculture and Technology,
Pantnagar, India
e-mail: mgh_zaidi@yahoo.com; ashu39335@gmail.com

M. G. H. Zaidi
Department of Chemistry, G.B. Pant University of Agriculture and Technology, Pantnagar, India

7.1 Introduction

In the era of electronic industry development, petition of multifunctional composites has been increased day by day to meet special requirement of components. This can be achieved by use of suitable fillers such as aluminium, nickel and copper fillers. Such fillers have good electrical and mechanical properties in order to mix with polymers to make composites for various applications [1].

Numerous efforts were proposed to improve epoxy composites properties through embedded cured matrix with various functional nanofilling materials, i.e. SiO_2 , GO, Al_2O_3 , nanodiamond, CNT and graphite. These organic/inorganic nanoparticles which are different types and grades were impregnated within epoxy matrix with various proportions to meaningfully enhanced their mechanical and physical properties and get improved nanocomposites [2]. For example, carbon nanofillers are used in epoxy for enhancing mechanical and electrical characterization by Zhu et al. (2009).

Composites which have conductive and magnetic properties are impregnated by ferrite particles into the bulk of an epoxy used. Embedding inorganic ferrite nanoparticle fillers in organic–inorganic epoxy composites display enhanced electrical properties as well as magnetic behaviour. This arrangement of a system allows the development of charge transporters of the fillers through the framework; thus, the composites accomplish a specific level of electrical conductivity properties; similarly, hysteresis properties of ferrite introduced magnetic behaviour in cured epoxy [3].

Ferrite particles are used in many applications because of good electrical and magnetic behaviours. Epoxy resin is the most promising polymer which based on its property those are low dielectric constant, electrical resistivity and ease of processing [4]. Addition of ferrite nanoparticles in epoxy is exclusively significant as magnetic nanoparticles have displayed ability in different applications such as spin-polarized devices, drug delivery carriers, recording application and as a microwave absorber materials whose main purpose to reduce dielectric losses, improved absorption ratio, reduce density of material and adjust electromagnetic parameters. Epoxy composites are best suitable for this purpose [5].

Additionally, by using ferrite particle, the magnetic behaviour as well as electrical behaviour of the epoxy can be simultaneously enhanced. Only polymer is not sufficient to drive good electrical property of composite because it have small amount of free charge carriers and so it is nonconductive and transparent to electromagnetic radiations. This can be derived by adding ferrite in the epoxy so that composites can have good electrical property [6]. Polymer composites gain conductivity after a certain concentration of conductive filler dispersion. This epoxy filler combination allows the movement of filler's charge carriers through cured epoxy matrix, and so resultant filler epoxy composite gains electrical conductivity [7].

This combination could make the polymer-based ferrite nanocomposite materials appropriate for various potential applications such as energy storage devices, sensors, electronic device, fuel cell's conducting membranes, microwave absorbers, capacitors, anticorrosive coating and fire-retardant composites [8]. Basically, the

main advantage of adding low concentrations nanoparticles which have larger surface/interface area per unit volume into polymers that nanoparticles enhanced characterization of particle composites without negotiating on density, or manufacturing process and accordingly increased the physicochemical interactions with cured epoxy matrix [9, 10]. But ferrite nanoparticle epoxy composites have some limitations. To maintain homogeneous dispersion and interfacial bonding strength between FNs and the epoxy resin is main concern in devolvement of epoxy-based ferrite nanoparticle composites. Actually, during the process when ferrite nanoparticles dispersed into epoxy resin slurry, ferrite nonoparticles formed agglomerates because of the strong magnetic interactions between the ferrite nanoparticles [11]. Agglomerates of hydrophilic ferrite nanoparticles could not be dispersed homogeneously in organic epoxy which commonly helped to the creation of micro-structural imperfections in the FNECs. These imperfections disturb the electrical conductivity and magnetic behaviour of composite [12].

For this reason, many research has searched an effective technique for enhancing the dispersion ferrite nanoparticles in the epoxy composite. Surface modification of filler materials by chemical treatments with suitable surfactant or coupling agents has been studied to enhanced dispersion and interfacial adhesion between the cured matrix and its fillers [13]. However, not much work has been made to investigate the surface modification of ferrite particles to improve characterization of ferrite nanoparticles' epoxy composites.

In present research, modified ferrite nanoparticles (MFNs) were prepared by surface modification of normal ferrite particles (FNs). In this chemical treatment process, APTS is used as a silane coupling agent. MFNs and FNs are used as a filler for fabrication of ferrite epoxy composites. The impact of ferrite dispersion in epoxy matrix after surface modification of ferrite nanoparticle on electrical and magnetic behaviour of composites is investigated. Spectral characterization of MFNs and FNs was analysed using FT-IR. Electrical and magnetic properties were examined by DC conductivity and VSM test, respectively.

7.2 Experimental

7.2.1 Materials

CY230, a commercially accessible epoxy which is based on DGEBA and HY 951 hardener, was procured from M/S Huntsman India Limited. APTS, a surface modification agent, was purchased by HiMedia Laboratory Pvt. Ltd., India. FNs (minimum assay 95%) were obtained from Research-Lab Fine Chem Industries, Mumbai, India. All chemicals are used without further any purifications process. Deionized water with conductivity 10^{-8} S/cm was used in the modification process.

7.2.2 *Synthesis of Modified Ferrite Nanoparticles Epoxies (MFNEs)*

The synthesis of MFNEs has been executed into two parts. In first part, modification of FNs is completed by surface treatment. In this part, by the help of ultra-sonication, 10 gm quantity of FNs was dispersed in 1000 ml deionized water in a flask, and 9 ml of APTS was added drop-wise into ferrite/water slurry. For vigorous stirring, a Teflon-coated powerful stirring bar has been used for 12 h at 45 ± 5 °C. The obtained particles were then centrifuged, cleaned with ethanol-distilled water solution (1:1) four times and then dried at 90 ± 5 °C to acquire MFNs, and on second part, epoxy composites were impregnated with varying weight percentage of MFNs and FNs. Separately, both ferrite particles were firstly mixed properly into CY 230 and then applied ultra-sonication in ice bath for 15 min. The attained ferrite/epoxy mixture was heated in microwave for 1 h at 90 ± 10 °C, and then ferrite/epoxy mixture was cooled down to 45 ± 5 °C. After that addition of the HY 951, the epoxy-modified ferrite nanoparticle and epoxy-normal ferrite nanoparticles were kept for curing at room temperature for 7 days in Teflon moulds to avoid stacking.

7.2.3 *Characterization*

The spectral characterization of the MFNEs, FNEs and cured epoxy samples was determined using FT-IR spectra. FT-IR spectra were recorded on PerkinElmer spectrophotometer over Thermo Nicolet in KBr pellet in transmission mode. VSM tests for magnetic behaviour of MFNEs, FNEs and cured epoxy were investigated over Lakeshore Vibrating Sample Magnetometer, 7410 series model, at room temperature, and DC conductivity test of MFNEs, FNEs and cured epoxy samples was performed on a 2182 A Keithley Nanovoltmeter machine. A current source which model number is 6221 and specimen holder with oven regulated by PID is connected to the voltmeter. This arrangement is procured from Scientific Instruments, India. A tissue paper is used for removing dust particles from two parallel sources of each sample which are 1 mm apart from each other. Successively, electrical condition was checked after polished with silver paint. At room temperature, four probe method has been used for obtaining specimen conductivity at 1, 10 and 100 V.

7.3 Results

Surface modification of FNs has been verified through FT-IR spectra as shown in Fig. 7.1. In FNs spectrum, OH group was shown one broad and another weak band at 3450 and 1820 cm^{-1} [14–16]. The peak at 560 cm^{-1} is representative to “Fe–O” [17]. FT-IR spectrum of MFNs compared with FNs spectra shown that the band

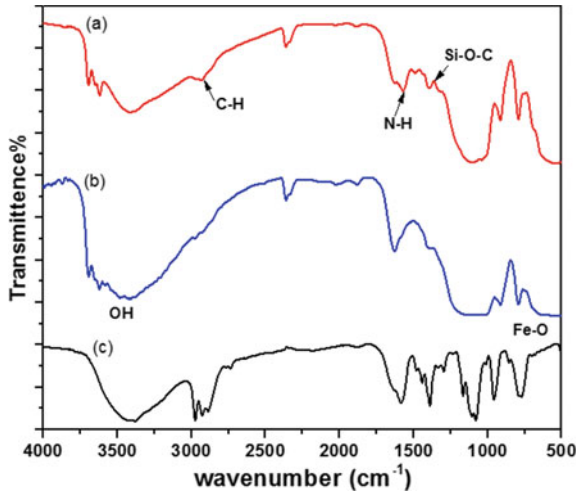


Fig. 7.1 FT-IR pattern of MFNs, FNs and APTS

near 3450 cm^{-1} becomes narrow due to APTS reaction that attached to FNs. In addition, MFN spectra have been shown three new bands at $2920(\text{C-H})$, $1600(\text{N-H})$ and 1300 cm^{-1} (Si-O-C) [15, 18]. These absorption bands approve that APTS surface modification agent was covalently attached to FNs. The acquired FT-IR spectra accept successful grafting of FNs with surface modification agent yielding MFN nanoparticles.

Figure 7.2 has shown the magnetization ($\text{emu/g} \times 10^{-2}$) of cured epoxy, FEs and MFNs with concentration of MFNs which are obtained by measuring their M–H loops in the applied field ranging -8 to 8 kOe . M–H curve of cured epoxy has revealed magnetization indicating 0.29 . However, with increased concentration of MFNs, magnetic moment has been increased and has shown a range from 6.80 to 18.06 . This relates to the growth in magnetic moment of MFNEs-I, MFNEs-II, MFNEs-III and MFNEs-IV by 6.80 , 8.72 , 13.70 and 18.06 , respectively, as compared to cured epoxy.

While magnetic moment of FNEs shows 14.53 . Surface modification of ferrite nanoparticles enhanced the dispersion of ferrite fillers in epoxy resin due to which homogeneously dispersion of modified ferrite nanoparticles improved magnetic property of epoxy composite compared to cured epoxy and normal ferrite epoxy composites [19–21].

Figure 7.3a, b show the variations in different DC conductivity ($\sigma_{\text{DC}} \times 10^{-3}$) properties of cured epoxy, FNEs and MFNEs with various voltage ranges from 1 to 100 V at room temperature. DC conductivity of cured epoxy has shown 2.99 at 1 V in Fig. 7.3a. A remarkable increment in electrical conductivity ranging from 4.07 to 5.44 has been shown with, respectively, increasing concentration of MFN. With variation in MFN concentration, MFNEs-I, MFNEs-II, MFNEs-III and MFNEs-IV have been shown 4.07 , 4.62 , 4.86 and 5.44 , respectively, at 1 V . Similarly at 10 V

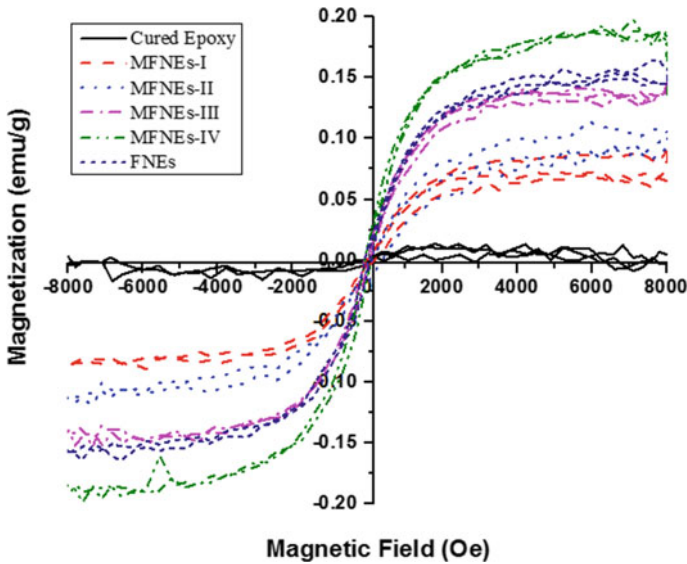


Fig. 7.2 VSM of different epoxy-modified ferrite nanoparticle (MFNEs), epoxy-normal ferrite nanoparticles (FNEs) and cured epoxy

and 100 V, cured epoxy has shown 3.28 and 1.13, respectively. Further increase in particles concentration σ_{DC} also shows a gradual increment in conductivity for 10 and 100 V. At 10 V DC conductivity of MFNEs-I, MFNEs-II, MFNEs-III and MFNEs-IV have been shown 4.28, 4.62, 4.90 and 5.46, respectively, whereas at 100 V, MFNEs-I, MFNEs-II, MFNEs-III and MFNEs-IV have been shown 10.24, 11.66, 12.57 and 13.28, respectively.

Figure 7.3b shows a comparison of σ_{DC} between cured epoxy, FNEs and MFNEs which indicate that σ_{DC} of MFNEs has been higher value comparison to cured epoxy and FNEs with respect to 1 V, 10 V and 100 V. FNEs conductivity at 1 V, 10 V, 100 V has shown 3.92, 4.16 and 11.46, respectively. The homogeneous dispersion of MFN into epoxy resin was established through gradually increase in σ_{DC} with respect to increasing concentration of filler. Increasing concentration of MFN decreased insulation of epoxy and increased conduction medium for electric charge in epoxy composite [22, 23]. Due to this reason, conductivity of MFNEs enhanced with respect to cured epoxy.

7.4 Conclusions

FNs were successfully converted into MFNs by the using of APTS as a surface modification agent. The acquired FT-IR spectra accept successful grafting of FNs with surface modification agent yielding MFNs nanoparticles. Enhanced dispersion

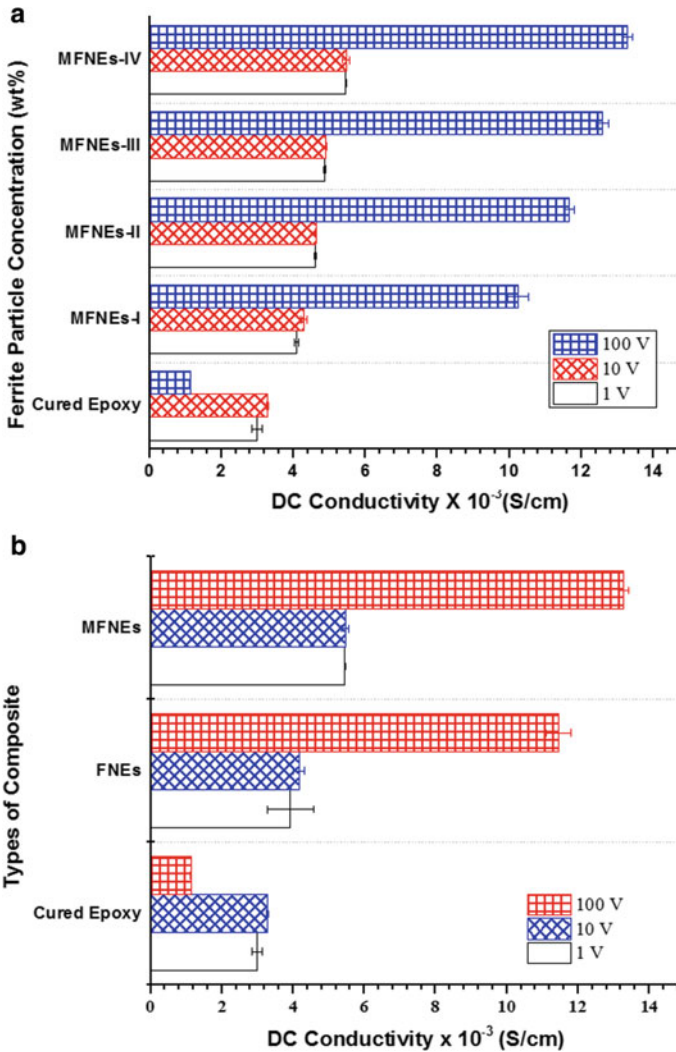


Fig. 7.3 **a** Effect of voltage on σ (S/cm) of MFNEs at room temperature with increasing wt% of MFNs. **b** Effect of voltage on σ (S/cm) of cured epoxy, FNEs and MFNEs at room temperature

and interfacial adhesion between the cured matrix and its ferrite nanoparticles were achieved due to APTS coupling. Due to APTS surface modification, agglomeration of ferrites has been minimized and attained homogeneously dispersion of ferrites in epoxy resin which has been shown better magnetic behaviour and DC electrical conductivity MFNEs compared to FNEs. Enhanced homogeneous dispersion of FNs into epoxy allows the movement of ferrite's charge carriers through cured epoxy matrix and so resultant ferrite/epoxy composite gain enhanced electrical conductivity. Results have been shown that magnetization of MFNEs was increased by 24.29%

with respect to FNEs, whereas DC electrical conductivity was increased by 38.77%, 31.25% and 15.88% at 1 V, 10 V and 100 V, respectively.

References


1. Fu, M., Jiao, Q., Zhao, Y.: In situ fabrication and characterization of cobalt ferrite nanorods/graphene composites. *Mater. Charact.* **86**, 303–315 (2013)
2. Zhang, X., Yan, X., Guo, J., Liu, Z., Jiang, D., He, Q.: Polypyrrole doped epoxy resin nanocomposites with enhanced mechanical properties and reduced flammability. *J. Mater. Chem. C* **3**(1), 162–176 (2015)
3. Ramajo, L.A., Cristóbal, A.A., Botta, P.M., López, J.M., Reboredo, M.M., Castro M.S.: Dielectric and magnetic response of Fe₃O₄/epoxy composites. *Comp.: Part A* **40**, 388–393 (2009)
4. Huang, Y., Li, Y.Q., Wang, Y.: Magnetic and electromagnetic properties of Pr doped strontium ferrite/polyaniline composite film. *J. Magn. Magn. Mater.* **368**, 133–138 (2014)
5. Wilson, J.L., Poddar, P., Frey, N.A., Srikantha, H.: Synthesis and magnetic properties of polymer nanocomposites with embedded iron nanoparticles. *J. Appl. Phys.* **95** (2004)
6. Chand, N., Jain, D.: Evaluation of a.c. conductivity behaviour of graphite filled poly sulphide modified epoxy composites. *Bull. Mater. Sci.* **27**(3), 227–233 (2004). © Indian Academy of Sciences)
7. Nadia, A.A.: The effect of additives metal on the DC conductivity of epoxy resin. *Baghdad Sci. J.* **8**(1), 168–174 (2009)
8. Guo, J., Zhang, X., Guo, H., Wang, Y., Yan, X., Ding, D., Long, J., Tadakamalla, S., Wang, Q., Mojammel, A.K., Jingjing, L., Zhang, X., Brandon, L.W., Sun, L., David, P.Y., Suying, W.Z.G.: Reinforced magnetic epoxy nanocomposites with conductive polypyrrole nanocoating on nanomagnetite as a coupling agent. *RSC Adv.* **4**, 36560–36572 (2014)
9. Ling, G., He, J.: The influence of nano-Al₂O₃ additive on the adhesion between enamel and steel substrate. *Mater. Sci. Eng. A Struct.* **379**, 432–436 (2004)
10. Giannelis, E.: Polymer layered silicate nanocomposites. *Adv. Mater.* **8**, 29–35 (1996)
11. Stabik, J., Chrobak, A., Haneczok, G., Dybowska, A.: Magnetic properties of polymer matrix composites filled with ferrite powders. *Arch. Mater. Sci. Eng.* **48**(2), 97–102 (2011)
12. Hsiang, H., Chen, W.S., Chang, Y.L., Hsu, F.C., Yen, F.S.: Ferrite load effects on the mechanical and electromagnetic properties of nzn ferrite powders-epoxy resin coatings. *Am. J. Mater. Sci.* **1**(1), 40–44 (2011)
13. Kalendová, A., Veselý, D., Kohl, M., Stejskal, J.: Effect of surface treatment of pigment particles with polypyrrole and polyaniline phosphate on their corrosion inhibiting properties in organic coatings. *Prog. Org. Coat.* **77**(9), 1465–1483 (2014)
14. Xiong, Q.Q., Tu, J.P., Ge, X., Wang, X.L., Gu, C.D.: One-step synthesis of hematite nanospindles from choline chloride/urea deep eutectic solvent with highly powerful storage versus lithium. *J. Power Sources* **274**(1), 1–7 (2015)
15. Naguib, H.M., Ahmed, M.A., Shanab, Z.L.A.: Silane coupling agent for enhanced epoxy-iron oxide nano composite. *J. Mater. Res. Technol.* **7**(1), 21–28 (2018)
16. Zaidi, M.G.H., Bhullar, N., Sharma, D., Agarwal, V., Alam, S., Rai, A.K., Pant, R.P.: Synthesis of polyvinyl pyridine ferrite nanocomposites in supercritical carbon dioxide. *J. Nanostruct. Polym. Nanocompos.* 103–109 (2007)
17. Roshan, A.H., Vaezi, M.R., Shokuhfar, A., Rajabali, Z.: Synthesis of iron oxide nanoparticles via sonochemical method and their characterization. *Particuology* **9**(2), 95–99 (2011)
18. Karakassides, M.A., Gournis, D.A., Petridis, D.: An infrared reflectance study of Si-O vibrations in thermally treated alkali saturated montmorillonites. *Clay Miner.* **34**(3), 429 (1999)
19. Hora, D., Lednický, F.E., Petrovsky, E., Ka, A.K.: Magnetic characteristics of ferrimagnetic microspheres prepared by dispersion polymerization, macromol. *Mater. Eng.* **2004**(289), 341–348 (2001)

20. Guo, J., Ye, X., Liu, W., Wu, Q., Shen, H., Shu, K.: Preparation and characterization of poly(acrylonitrile-co-acrylic acid) nanofibrous composites with Fe_3O_4 magnetic nanoparticles. *Mater. Lett.* **63**, 1326–1328 (2009)
21. Zaidi, M.G.H., Sah, P.L., Alam, S., Rai, A.K.: Synthesis of epoxy ferrite nanocomposites in supercritical carbon dioxide. *J. Exp. Nanosci.* **4**, 55–66 (2009)
22. Zheng, H., Cheng, Y., Wang, S., Bao, F., Zhou, H., Wei, F., et al.: Quasicubic Fe_2O_3 nanoparticles with excellent catalytic performance. *J. Phys. Chem. B* **110**, 3093–3097 (2006)
23. Chen, W.S., Chang, Y.L., Hsiang, H.I., Hsu, F.I., Yen, F.U.: Effects of titanate coupling agent on the dielectric properties of NiZn ferrite powders–epoxy resin coatings. *Ceram. Int.* **37**, 2347–2352 (2011)
24. Fulco, A.P., Melo, J.D., Paskocimas, C.A., Medeiros, S.N., Machado, F.L., Rodrigues, A.R.: Magnetic properties of polymer matrix composites with embedded ferrite particles. *NDT E Int.* **77**, 42–48 (2015)
25. Kim, H.J., Jung, D.H., Jung, I.H., Cifuentes, J.I., Rhee, K.Y., Hui, D.: Enhancement of mechanical properties of aluminium/epoxy composites with silane functionalization of aluminium powder. *Compos. B: Eng.* **43**(2012), 1743–1748 (2012)

Chapter 8

A Review on Coating for Hydro-turbine Application by HVOF Process



Mohit Vishnoi , Paras Kumar , and Qasim Murtaza 

Abstract Erosive wear of hydro-turbine runner's blade is a complex aspect, which depends upon different factors like silt size, hardness, velocity of water and substrate material properties. The turbine runner's efficiency has been deteriorated with the increase in the erosive wear, and final failure of hydro-turbine runners occurs. In many of the literatures, researchers have conducted different experiments to investigate the effect of these factors on erosive wear, but the size of samples has been considered in various types of test apparatus to affect the flow conditions in the turbine, but actual flow conditions and the fact of erosive wear are too complex to replicate. The literature presents the concern associated with materials and fabrication process of deployed coatings by HVOF approach used for the stability of hydro-turbine runner. The primitive mechanisms of annihilation techniques resulting in the hydro-turbine runner's blade were given in article. The primitive approaches of thermal spraying were described, which grant the deployment of coatings with the chemical composition, phase structure and properties convenient for the improvement of functional performance. There are some recently used and possible target materials, and coating materials were presented in this article. The advantages and disadvantages of the approach of HVOF were discussed. The primitive groups of coatings with a considerable resistance to corrosion and slurry erosion wear produced by thermal spraying (HVOF) method, which can be used in the hydro-electric power plant industry, were described, and also studies undertaken in this field by several investigators have been discussed broadly.

Keywords HVOF (high-velocity oxy fuel) · Silt erosion · Erosion wear

M. Vishnoi (✉) · P. Kumar · Q. Murtaza
Department of Mechanical Engineering, Delhi Technological University, Delhi 110042, India
e-mail: vishnoi.mohit06@gmail.com

P. Kumar
e-mail: paraskumar@dtu.ac.in

Q. Murtaza
e-mail: qasimmurtaza@dce.ac.in

8.1 Introduction

The components of hydro-electric power plants like turbine blades need to carry consistent high-speed impingement of water (with erodent and without erodent particles); along these lines, they ought to have outstanding erosion/corrosion resistance and mechanical properties [1, 2]. Indeed, even erosion is extensive for the consistent expulsion of material from the part surfaces; the consistent exposure to erosive climate could prove to be unfavourable and consequence in failure of equipment because of weight reduction.

The high-velocity oxy fuel (HVOF) coating is favoured in the light of the fact that replacement cost of substrate material is 50% more than the manufacturing cost [3, 4] and furthermore its inherent advantageous points. HVOF process offers following points of interest as: (i) it has unrivalled dexterity of resorting high enough kinetic energy in depositing hard element powders of nitrides and carbides on different substrate materials. (ii) To furnish coatings with invulnerable, homogeneous deposition with elevated hardness and wear resistance, toughness with shortened deformities and porosity just as better binding quality, it makes them prudent for application which has awful environmental factors, for example, hydro-turbine blades. [5–8].

In recent years, HVOF spraying has been viewed as an advantage for the group of thermal spray processes particularly for materials with melting point below 3000 °K. It has been supported effectively, since it shows favourable circumstances in density and bond strength making it attractive for many wear and corrosion resistance applications [9–12].

There are two key parts tungsten carbide/cobalt and chromium carbide/nickel chrome which are utilized in hard metal-based coatings.

Tungsten carbide materials are in general recommended for wear applications where service temperature is under 500 °C. Matrices of considerable cobalt upgrade the coating toughness. The utilization of chromium upgrades the impact resistance as well as corrosion resistance.

Chromium carbide materials are frequently utilized for high-temperature operation materials than tungsten carbide materials with a service temperature range from 540 to 815 °C. Secondary constituents' components like nickel and chromium are utilized in chromium carbide materials to prevent chromium carbide decomposition at the time of spraying process (carbon loss) as well as to improve some physical and mechanical properties [13].

Addition of molybdenum to the hard phase's metallic alloys gives the better adhesion between bindings and ceramics which positively improves sufficient oxidation kinetics. In addition, from sintered ceramics, it is said that replacing carbon by nitrogen up to 20% in the hard phase's metallic compounds confines carbide development at the time of sintering and gives more uniform phase dispersion [14].

TiC–Ni-based composite coatings can link the disparity between tungsten carbide and chromium carbide materials coating with practically identical fair corrosion resistance and abrasion resistance [14].

8.2 Overview of the Experimental Studies Performed on HVOF Coated Substrate

Table 8.1 summarizes the experimental details like coating material, substrate material, sample dimension, test conducted and coating thickness used by various investigators.

8.3 Discussion

Various researchers have mainly focussed on tribological behaviour, mechanical properties and coating characterization.

Coating Characterization

Katranidis et al. [21] gave a brief thought regarding the more prominent level of defects and porosity in the beginning powder which emerges in the spraying and involving of fine particles (under 5μ) which approved in significant plastic deformation during impact and persistent edges of metallic tungsten spreading along the splat boundary.

Kiilakoski et al. [22] revealed that the covering morphologies were denser and bimodal, with nanosized YSZ/ZrO₂ particles and bunches thereof covering the inter-lamellar regions between the Al₂O₃ splats, along with some mixed phases of Al₂O₃-YSZ/ZrO₂.

de Souza Brandolt et al. [29] analysed the HVOF-coated surface and observed that HVOF coatings behaved as an obstacle to the passage of hydrogen, which advanced the entire material (substrate + coating) and had a greater hydrogen retention limit. Micro-printing demonstrated the preferential aggregation hydrogen inside to the splashed layers, checking the coating obstruction effect. Utilizing cobalt and nickel coatings created by warm spraying against hydrogen entry showed to be significant, because of the presence of considerable density of discontinuities.

Liu et al. [32] were investigated three fixed coatings deployed on the iron-based amorphous coatings. All were adequately close the imperfections and improve the micro-hardness of iron-based amorphous coating, and by addition of cerium nitrate into the sol-gel coating deteriorates the density of deployed coating. Electrochemical test for corrosion resistance of iron-based amorphous coating indicated upgrade in corrosion resistance after sealing treatment in correlation with that of unsealed coating. The corrosion resistance increases in the arrangement: Substrate < Fe-based amorphous < SCN < SG < SCT covering. EPMA and XPS results revealed that by the addition of cerium salts indicated a specific corrosion restraint job on the sol-gel coating because of the formation of cerium oxide.

Giouse et al. [34] experimented that cracks starts nucleating from the edge of the particle also found by proposing that failure could preferentially take place in the layer affected by the grit blasting, and it is not at the coating base mental interface. Failure

Table 8.1 Comparative study of various researchers

References/author/paper year	Coating material	Substrate material	Sample dimension	Test conducted	Coating thickness
Bolelli et al. (2018) [15]	75% (vol.) TiC – 25% (vol.) (Fe-20 wt%Cr-5wt% Al)	AISI 304 stainless steel plates	(60 mm * 25 mm * 3 mm)	1. Scanning electron microscopy test 2. X-ray diffraction test 3. Hardness test 4. Wear test 5. Electrochemical corrosion test	Set-1: 307 ± 26 µm Set-2: 520 ± 9 µm

(continued)

Table 8.1 (continued)

References/author/paper year	Coating material	Substrate material	Sample dimension	Test conducted	Coating thickness
Kiragi et al. (2018) [16]	Ti-Al-N	AA1050 and AA5083	(25 mm * 25 mm * 5 mm)	<ol style="list-style-type: none"> 1. Scanning electron microscopy test 2. Energy dispersive X-ray spectroscopy test 3. Slurry erosion wear test 4. Micro-hardness test 5. Optimization by Taguchi approach by control parameters like impact velocity, impingement angle, erodent feed rate, erodent size 6. Contour plot with the help of HyperMesh 	AA1050 and AA5083: 170 and 210 µm

(continued)

Table 8.1 (continued)

References/author/paper year	Coating material	Substrate material	Sample dimension	Test conducted	Coating thickness
Ghazanfari et al. (2018) [17]	Fe ₃ Al–TiC (Fe ₃ Al-30TiC, Fe ₃ Al-50TiC, and Fe ₃ Al-70TiC)	Mild steel	(Diameter 10 mm)	1. Scanning electron microscopy test 2. X-ray diffraction test 3. Energy-dispersive X-ray spectroscopy test 4. Micro-hardness test 5. Dry sliding wear test	Average thickness: 200–250 μm
Rodríguez et al. (2018) [18]	316L austenitic stainless steel powder (17 Cr, 12 Ni, 2.5 Mo, 2.3 Si, 0.03 C and balance Fe (in wt%))	ZE41 magnesium alloy (4.09 Zn, 1.7 rare earths (Pr + Nd + La + Ce), 0.68 Zr, 0.6 O and balance Mg)	(Discs of diameter 10 mm)	1. Scanning electron microscopy test 2. Nano-indentation test 3. Micro-hardness test 4. X-ray diffraction test 5. Light microscopy	L1: 240 ± 13 μm L2: 309 ± 18 μm L3: 318 ± 19 μm L4: 315 ± 16 μm (L: Layer)

(continued)

Table 8.1 (continued)

References/author/paper year	Coating material	Substrate material	Sample dimension	Test conducted	Coating thickness
Liu et al. (2018) [19]	WC-10Co4Cr	35CrMo steel	(50 mm * 10 mm * 5 mm)	<ol style="list-style-type: none"> 1. Scanning electron microscopy test 2. X-ray diffraction test 3. Micro-hardness test 4. Slurry erosion wear test 5. Porosity and roughness test 	Average thickness: 325 μm
Krelling et al. (2018) [20]	WC-10Co-4Cr	AISI 4140 steel	(Disc of thickness 10 mm and diameter 50.8 mm)	<ol style="list-style-type: none"> 1. Scanning electron microscopy test 2. X-ray diffraction test 3. Energy-dispersive X-ray spectroscopy test 4. Micro-hardness test 5. Roughness test 6. Abrasive wear test 	Before grinding: HC: 203 ± 16 μm TC: 218 ± 23 μm After grinding: HC: 135 μm TC: 138 μm (HC: hard chromium WC: tungsten carbide)

(continued)

Table 8.1 (continued)

References/author/paper year	Coating material	Substrate material	Sample dimension	Test conducted	Coating thickness
Katranidis et al. (2018) [21]	WC-17Co	Steel	–	1. Scanning electron microscopy test (a) Back-scattered electron (b) Focused ion beam 2. Energy-dispersive X-ray spectroscopy test 3. X-ray diffraction test	13 μm^2 square area
Kiilakoski et al. (2018) [22]	1. Al ₂ O ₃ 2. Al ₂ O ₃ -20YSZ 3. Al ₂ O ₃ -40YSZ 4. Al ₂ O ₃ -40ZrO ₂	Stainless steel (AISI 316)	(50 mm * 100 mm * 5 mm)	1. Field emission scanning electron microscopy test (a) Focused ion beam 2. Energy-dispersive X-ray spectroscopy test 3. X-ray diffraction test 4. Micro-hardness test	1. 180 μm 2. 170 μm 3. 134 μm 4. 250 μm Respectively as in coating materials

(continued)

Table 8.1 (continued)

References/author/paper year	Coating material	Substrate material	Sample dimension	Test conducted	Coating thickness
Mohanty et al. (2018) [23]	Carbon nanotube-reinforced in WC-Co	Ti-6Al-4V	(50 mm * 50 mm * 5 mm)	<ol style="list-style-type: none"> 1. Field emission scanning electron microscopy test 2. X-ray diffraction test 3. Micro-hardness test 4. Roughness test 5. Super-abrasive grinding test 6. Cohesive strength test and residual strength 7. Ball-on-disc tribometry test 	Average diameter is increased to 28 nm
Marques et al. (2018) [24]	<ol style="list-style-type: none"> 1. (Cr₃C₂ 25Ni Cr) 2. (WC 10Co 4Cr) 	H13 tool Steel	-	<ol style="list-style-type: none"> 1. Scanning electron microscopy test 2. X-ray diffraction test 3. Micro-hardness test 4. Roughness test 5. Abrasive wear test 	<ol style="list-style-type: none"> 1. 118.3 μm 2. 122 μm Respectively as in coating materials

(continued)

Table 8.1 (continued)

References/author/paper year	Coating material	Substrate material	Sample dimension	Test conducted	Coating thickness
Xie et al. (2018) [25]	Fe-9.6Si-5.4Al (in wt%) powder precoated with Ni	Pure aluminium plates	–	1. Scanning electron microscopy test 2. Energy-dispersive X-ray spectroscopy test 3. Micro-hardness test 4. Magnetic properties test 5. Dry sliding wear test	Total 325 μm
Toma et al. (2018) [26]	Cr_2O_3 (+10 to 45 μm) and Cr_2O_3 -15TiO ₂ (+5 to 25 μm and +10 to 45 μm) CoNiCrAlY bond coat	1.4462 duplex steel (X2CrNiMoN22-5-3)	(25 mm of diameter)	1. Scanning electron microscopy test 2. X-ray diffraction test 3. Energy-dispersive X-ray spectroscopy test 4. Sliding wear resistance test 5. Porosity test	Average thickness: 150 \pm 20 μm

(continued)

Table 8.1 (continued)

References/author/paper year	Coating material	Substrate material	Sample dimension	Test conducted	Coating thickness
Koga et al. (2018) [27]	FeCrMnCoSi (6.1 wt% Fe, 17 wt% Cr, 10 wt% Mn, 9 wt% Co, 3 wt% Si, 0.2 wt% C, 0.2 wt% N)	304 stainless steel	(190 mm * 120 mm * 1.5 mm)	<ol style="list-style-type: none"> 1. Scanning electron microscopy test 2. X-ray diffraction test 3. Potentiodynamic polarization test 4. Micro-hardness test 5. Dry sliding wear test 	Average thickness: 50 μ m
Bandyopadhyay et al. (2019) [28]	<ol style="list-style-type: none"> 1. Diamond-reinforced bronze (90 wt% pure bronze, 10 wt% commercially available diamond) 2. Bronze (gas atomized, $-30 + 5 \mu$m) 	AISI 52100 bearing steel	(50 mm * 50 mm * 6 mm)	<ol style="list-style-type: none"> 1. Scanning electron microscopy test 2. Optical microscopy test 3. X-ray diffraction test 4. Micro-hardness test 5. Porosity test 6. Ball-on-disc sliding test 	Average thickness: 180–250 μ m

(continued)

Table 8.1 (continued)

References/author/paper year	Coating material	Substrate material	Sample dimension	Test conducted	Coating thickness
Brandolt et al. (2019) [29]	API 5CT P110 steel (Fe-0.3C-0.65Mn-0.02P-0.01S-1.01 Cr-0.2 Mo-0.17 Ni)	Nickel (99.9425%) and cobalt (99.9%) powders	(120 mm * 20 mm * 10 mm)	1. Scanning electron microscopy test 2. X-ray diffraction test 3. Roughness test 4. Micro-hardness test 5. Porosity test 6. Hydrogen embrittlement tests (a) Tensile test (b) CHNS (carbon, hydrogen, nitrogen and sulphur) elemental analysis for hydrogen mass quantification (c) Determination of hydrogen trapping mechanisms by micro-printing technique	Average thickness: 100 µm

(continued)

Table 8.1 (continued)

References/author/paper year	Coating material	Substrate material	Sample dimension	Test conducted	Coating thickness
Chen et al. (2019) [30]	WC-17Co	AISI 1045 steel	(55 mm * 50 mm * 4.5 mm)	<ol style="list-style-type: none"> 1. Scanning electron microscopy test 2. X-ray diffraction test 3. Energy-dispersive X-ray spectroscopy test 4. Micro-hardness test 5. Sliding wear test (ball-on-disc apparatus) 	Average thickness: 300 µm
Singh et al. (2019) [31]	<ol style="list-style-type: none"> 1. Ni- Cr₂O₃ 2. NiCr₅Si-WC(Co) 	Stainless steel (SS 316L) substrate	(67.5 mm * 25 mm * 5 mm)	<ol style="list-style-type: none"> 1. Scanning electron microscopy test 2. X-ray diffraction test 3. Energy-dispersive X-ray spectroscopy test 4. Micro-hardness test 5. Roughness test 6. Slurry erosive wear test 	<ol style="list-style-type: none"> 1. 261 ± 95 µm 2. 265 ± 35 µm Respectively as in coating materials

(continued)

Table 8.1 (continued)

References/author/paper year	Coating material	Substrate material	Sample dimension	Test conducted	Coating thickness
Liu et al. (2019) [32]	Fe _{54.2} Cr _{18.3} Mo _{13.7} Mn _{2.0} W _{6.0} B _{3.3} C _{1.1} Si _{1.4} (in wt%)	921 carbon steel (10CrNi ₃ MoV)	(10 mm * 10 mm * 15 mm)	<ol style="list-style-type: none"> 1. Scanning electron microscopy test 2. Fourier transform infrared spectroscopy (FTIR) Test 3. Potentiodynamic polarization 4. Electrochemical impedance spectroscopy (EIS) 5. X-ray photoelectron spectroscopy (XPS) 6. Electron probe micro-analyser (EPMA) 7. Micro-hardness tests 	-

(continued)

Table 8.1 (continued)

References/author/paper year	Coating material	Substrate material	Sample dimension	Test conducted	Coating thickness
Chen et al. (2019) [33]	$Fe_{71}B_{20}Si_5Nb_4$	0.45 wt% middle-carbon steel	–	<ol style="list-style-type: none"> 1. Scanning electron microscopy test 2. Energy-dispersive X-ray spectroscopy test 3. Micro-hardness test 4. Roughness test 5. Slurry erosive wear test 6. Impact surface morphology 7. Cohesive strength 	HVOF: 235.4 μm WPPA-HVOF: 193.5 μm
Giouse et al. (2019) [34]	Chromium carbides Cr_3C_2 embedded in a NiCr metallic binder (80% Cr_3C_2 , 20% NiCr)	17-4 precipitation hardening (17-4PH) martensitic steel	–	<ol style="list-style-type: none"> 1. Scanning electron microscopy test 2. Atomic force microscopy 3. Nano-indentation test 4. Grit blasting 	Average thickness: 250 μm

(continued)

Table 8.1 (continued)

References/author/paper year	Coating material	Substrate material	Sample dimension	Test conducted	Coating thickness
Qiao et al. (2019) [35]	20% Cr, 15% Mo, 5% Ni, 4.5% B, 3% Co, 2.5% Cu, 1.875% Si, 0.625% C, and the balance Fe (in wt%)	45 steel	–	1. Transmission electron microscopy 2. Energy-dispersive X-ray spectroscopy test 3. X-ray diffraction test 4. Optimization of parameters like spray distance, oxygen flow and kerosene flow by Taguchi approach	–
Azizpour et al. (2019) [36]	Stellite-6 powder (Cr 28.6%, Si 1.1%, C 1.3%, W 4.9%, Fe 1.9%, Ni 2.2, Mn 0.3 and the rest balancing cobalt matrix) (in wt%)	AISI 1045 steel	–	1. Scanning electron microscopy test 2. X-ray diffraction test 3. Micro-hardness test 4. Electro-discharge milling 5. Exact evaluation of stress	Average thickness: 400 µm

in the coating at the interface is greater chance to occur, and hardness increased by 20% more at the interface as compared to the bulk was observed.

Qiao et al. [35] reported that the use of kerosene showed the greatest effect on the porosity of the coatings. All coatings subsisted primarily of amorphous phases. Likewise, in the iron-based amorphous coatings, coating with lower porosity showed better corrosion resistance.

Mechanical Characterization

García-Rodríguez et al. [18] reported that larger the deformation developed in the coatings at the time of spraying process, the higher was compactness achieved, the fracture resistance and hardness of the coatings considerably enhanced also by increasing the number of layers in the coatings resulted more compact coatings with very less enhance in hardness which also showed higher fracture resistance because ferrite content enhanced with addition of number of layers. These result a slight enhance in hardness of coating. When spraying distance was increased and the porosity of the coated surface reduced, but the amount of oxides enhanced so a lesser fracture resistance was achieved.

Azizpour et al. [36] investigated the residual stress at the surface evaluated was tensile and turned into compressive towards the coated base metal interface. The results obtained from the numerical simulation showed a good compromise with electro-discharge hole drilling method.

Tribological Behaviour

Bolelli et al. [15] performed the ball-on-disc test at room temperature on three type of Cr based coating such as HVOF-TiC-FeCrAl, HVOF-Cr₃C₂-NiCr and hard chromium electroplating. The characterization result revealed that the TiC-FeCrAl coatings give minimum wear rate and can be used for the application in dry sliding condition.

Kiragi et al. [16] detailed that order for these parameters on coatings is as follows: for AA1050, impact velocity showed the highest affected parameter and least affected parameter is erodent size got optimum value 30 m/s (impact velocity), 225 μm (erodent size); for AA5083, impact velocity indicated the most noteworthy parameter and erodent feed rate are the least affected parameters which got optimum values 25 m/s (impact velocity) and 160 g/min (erodent feed rate).

Ghazanfari et al. [17] saw that wear rate went down up to 75% by addition of TiC content from 30 to 50 mol%. The wear rate further get somewhere around more than one order for size by including TiC content from 50 to 70 mol% and that coatings hardness improved with expansion of TiC content. Liu et al. [19] examined bimodal and proposed that traditional and bimodal coatings are seen as accommodating to increment in the slurry erosion assurance in contrast with 35CrMo substrate attributable to the extraordinary hardness. Likewise, the bimodal coating has predominant erosion assurance.

Krelling et al. [20] detailed that the resistance for WC-10Co-4Cr coating was discovered multiple (five) times higher than the wear resistance of the SAE 4140 steel

under Q&T condition and concluded noteworthy point that abrasion and adhesion because of plastic distortion were the key wear systems acknowledged in Q&T tests.

Mohanty et al. [23] revealed that the reinforced coatings showed up to 10, 30 and 33% improvement in elastic modulus, hardness and cohesive strength, respectively. The residual stress of the HVOF splashed coatings was compressive in nature and increased further, in the magnitude of compressive stress using surface grinding. Further, it can be justified in HVOF coatings to use 1 wt% carbon nanotube as reinforcement in both regular and nanostructured WC-Co feedstock to ease in surface grinding and carbon nanotube (CNT) does not encounter deterioration during the spraying whereas it improve wear resistance, fracture toughness, hardness and elastic modulus of the coating.

Marques et al. [24] noticed that both punches undergone a combination of various categories of wear primarily abrasive wear and thermal fatigue. The coefficient of thermal expansion of the base material and the coatings were distinct, and this was a one of the factors that provoked stresses and led to coating cracks also. They have also noticed fragmentation and aggregation of worn debris which has prone to change the wear mode. The busted debris acted as an abrasive particle which increased the overall coating wear.

Xie et al. [25] gave the remarkable conclusions that the cold spray Ni/FeSiAl composite coating showed the greater deformation of the particles as well as superior density, whereas the high-velocity oxy fuel (HVOF) coating showed large levels of noticeable defects and marginally greater oxide content. By X-ray diffraction analysis, both Ni/FeSiAl soft magnetic composite coatings had no considerable phase conversion and oxide formation during impeachment processes, while incomplete melting of FeSiAl particles was realized in the HVOF-coated surface. The nickel bonding layer contributes a vital role for successful deposition of the composite particles in both the cold spray and HVOF techniques. In cold spray process, metallic bonding can be obtained by the severe plastic deformation (SPD) of the nickel layers with high-impact velocity of particles. The partial melting of nickel layer owing to a large processing temperature should be contributed for the strong bonding during HVOF deposition process as well as the greater retainability of FeSiAl particles in the composite coating.

Toma et al. [26] reported that the suspension (S-HVOF) sprayed coatings showed almost closed micro-structure and having considerable hardness. The corrosion resistances in acidic medium of S-HVOF-coated surfaces were remarkable good to those formed from feedstock spray powders. Despite almost close packed micro-structure of S-HVOF, there is an existence of some defects in the coating (i.e. open porosity, cracks). These coating defects have a vital role on the corrosion performance of the coated surfaces sprayed with metallic bond coat. The sliding wear resistance of the S-HVOF-coated surface was having great dependency on the coating system also on the wear conditions (lubricated or un-lubricated system, counterpart). As in un-lubricated situations, the S-HVOF-coated surfaces revealed greater coefficients of friction than the atmospheric plasma spraying-coated surfaces on sliding against alumina ball but results the lowest coefficients of friction with sliding against steel ball was done.

Koga et al. [27] investigated the FeCrMnCoSi HVOF coating which obtained satisfactory results to corrosion and wear performance for practical applications in seawater environments and subjected to sliding wear.

Bandyopadhyay et al. [28] shown some important results after experimentation that the composite bronze coatings showed better wear resistance and wear coefficient was reduced about 65%. The ductility and greater hardness of the coating is traced to finite dislocation movement due to presence of diamond. This final consistent increase in the wear resistance of the diamond-reinforced coatings has been observed.

Chen et al. [30] reported that the WC grains within the presolid solution treatment powder (PSTP) feedstock showed a faceted shape and bimodal size arrangement, whereas those in the ball-milled powder mixture (BMPM) feedstock displayed a rounded shape and uni-modal size distribution. For the PSTP-SHIP (sintered hot isostatic pressing) route, abnormal grain growth takes place, prominent to a bimodal grain size distribution and the cermets which resulted in the greatest hardness and transverse rupture strength (TRS). For the BMPT-SHIP route, the tungsten carbide grains were evenly distributed and the cermet showed the lowest hardness but the greatest fracture toughness. The cermets obtained using the BMPM-SHIP route showed the excellent wear resistance, which is associated with the development of a closely packed tribo film on the surface at the time of sliding contact.

Singh et al. [31] investigated NiBCrSi-WC (Co) and Ni-Cr-O coatings and concluded the order of influenced parameters on coatings and reported that NiBCrSi-WC (Co) sprayed revealed lesser erosion wear as compared to Ni-Cr-O sprayed on SS-316L. At an impingement angle of 30°, SS-316L and Ni-Cr-O coatings showed maximum erosion. The order of erosion wear at 45°, 30° and 0° was found as NiBCrSi-WC (Co) > Ni-Cr-O > SS316L. At an impingement angle of 60°, the chronological order of erosion wear was found as Ni-Cr-O > NiBCrSi-WC (Co) > SS316L.

Chen et al. [33] investigated the residual stress of the warm particle peening-assisted (WPPA-HVOF) coating which turns into more compressive. As an out-growth, the coating structure turns into dense as the porosity can be as less as 0.70%. When compared with the high-velocity oxy fuel obtained coatings, the mechanical properties of the WPPA-HVOF coating like cohesive strength, micro-hardness and wear resistance are also enhanced to different degrees. Inclusion of peening particle greatly provoked erosion to the earlier deposited layers and deteriorates the deposition of the influence splats.

As shown in Fig. 8.1, few common hard metal compositions and their important properties, like hardness (VHN), abrasive wear (mg/cm²) and cavitation wear (mg/h) on the basis of oxygen (wt%) and carbon (wt%) in powder/coating, respectively.

8.4 Applications

There are some practical industrial applications of different thermal sprayed coatings with adapted form of pictures as shown in Figs. 8.2, 8.3, 8.4, 8.5, 8.6, 8.7 and 8.8 [13].

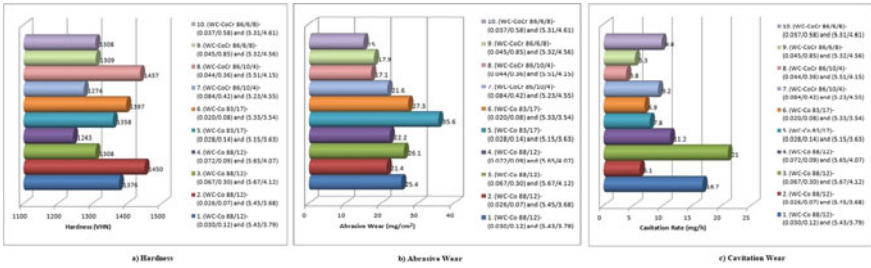


Fig. 8.1 Variation of **a** hardness, **b** abrasive wear, **c** cavitation rate of different hard metal HVOF coatings, respectively



Fig. 8.2 Pure metals/Zinc: Due to good corrosion resistance used at metal structure in bridges [37]



Fig. 8.3 Self-fluxing alloys/Ni-Cr-B-Si: used at shafts, sleeves due to its high hardness, almost no pores after fusing [38]

Fig. 8.4 Steels/Fe-13Cr: Used at repair parts due to its low-cost material, good wear resistant [39]



Fig. 8.5 MCrAlY alloys/Ni-Cr-Al-Y: Used at blades and vanes in gas turbines due to its good corrosion and oxidation resistance at high temperature [40]



Fig. 8.6 Nickel-graphite composites/Ni-25C: Used at sealing of air inlet channels in compressors due to its clearance control [41]



8.5 Conclusions

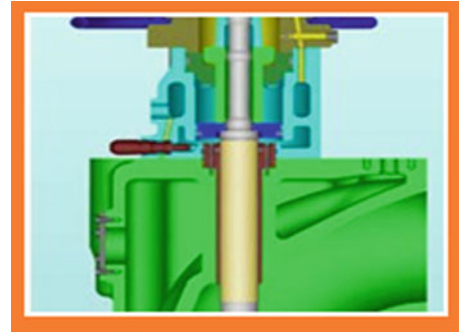
From various literatures, following points can be concluded:

1. Tungsten carbide material coatings are generally most suitable for wear applications of hydro-turbine due to its service temperature which is less than 500 °C.

Fig. 8.7 Oxides/ Al_2O_3 , Cr_2O_3 : Used at parts in textile machines, paper machine cylinders due to its high hardness, good temperature stability [42]



Fig. 8.8 Hard metal (Carbides)/WC-12Co, Cr_3C_2 -25NiCr: Used at valves, wear parts, paper machine cylinders due to its high hardness and wear resistance in nature [43]



2. Various coatings such as WC-CoCr, Cr_3C_2 -NiCr, Al_2O_3 , stellite, Cr_2O_3 , Cr_3C_2 -NiCr, NiCrSiB-35 wt% WC-Co, WC-10Co-4Cr, nanostructured Ni60-TiB₂ and WC-12Co had been investigated by the researchers for producing resistance against slurry and wear erosion. Despite investigating various coating behaviours, still requirement of investigation is needed more on HVOF coating so that new composite coatings can be obtained by mixing these powders.
3. Erosive wear rate mainly depends on the parameters like as impact angle, velocity, concentration and particle size.
4. Ductile materials exhibited maximum erosion loss at lower impingement angles and decreases at higher impingement angles. But in case of brittle materials, erosion rate increases with increase in the impingement angle attained maximum at 90°.
5. The roughness of the coating obtained by HVOF plays a significant role in wear rate of the coated surface. It has been observed that the coated surface with greater surface roughness eroded out at a rapid rate than lower surface roughness.

6. Maximum thickness of HVOF-coated surfaces was reported as in the range of 50–500 μm by different investigators.

References

1. Lin, M.C., Chang, L.S., Lin, H.C., Yang, C.H., Lin, K.M.: A study of high-speed slurry erosion of NiCrBSi thermal-sprayed coating. *Surf. Coat. Technol.* **201**, 3193–3198 (2006)
2. Goyal, D.K., Singh, H., Kumar, H., Sahni, V.: Slurry erosion behaviour of HVOF sprayed WC-19Co-4Cr and $\text{Al}_2\text{O}_3 + 13\text{TiO}_2$ coatings on a turbine steel. *Wear* **289**(15), 46–57 (2012)
3. Peat, T., Galloway, A., Toumpis, A., Harvey, D., Yang, W.H.: Performance evaluation of HVOF deposited cermet coatings under dry and slurry erosion. *Surf. Coat. Technol.* **300**, 118–127 (2016)
4. Grewal, H.S., Agrawal, A., Singh, H., Shollock, B.A.: Slurry erosion performance of Ni- Al_2O_3 based thermal-sprayed coatings: effect of angle of impingement. *J. Therm. Spray Technol.* **23**(3), 389–401 (2014)
5. Pawlowski, L.: Thermal Spraying Techniques. In: Pawlowski, L. (ed.) *The Science Engineering of Thermal Spray Coatings*, 2nd edn. Wiley, London (2008)
6. Nitesh, V., Khatirkar, R.K., Sapate, S.G.: Tribological behaviour of HVOF sprayed WC-12Co, WC-10Co-4Cr and Cr3C2-25NiCr coatings. *Tribol. Int.* **105**, 55–68 (2017)
7. Murugan, K., Ragupathy, A., Balasubramanian, V., Sridhar, K.: Optimizing HVOF spray process parameters to attain minimum porosity and maximum hardness in WC-10Co-4Cr coatings. *Surf. Coat. Technol.* **247**, 90–102 (2014)
8. Kumar, A., Sharma, A., Goel, S.K.: Erosion behaviour of WC-10Co-4Cr coating on 23-8-N nitronic steel by HVOF thermal spraying. *Appl. Surf. Sci.* **370**, 418–426 (2016)
9. Stein, K.J., Schorr, B.S., Marder, A.R.: Erosion of thermal spray MCr-Cr3C2 cermet coatings. *Wear* **224**, 153–159 (1999)
10. Jacobs, L., Hyland, M.M., De Bonte, M.: Study of influence of microstructural properties on the sliding wear behaviour of HVOF and HVOF sprayed WC-cermet coatings. *J. Thermal Spray Technol.* **8**(1), 125–132 (1999)
11. Hawthorne, H.M., Arsenault, B., Immarigeon, J.P., Lagouse, J.G., Parameswaram, V.R.: Comparison of slurry and dry erosion behavior of some HVOF thermal sprayed coatings. *Wear* **225–229**, 825–834 (1999)
12. Browning, J.A.: Viewing the future of high velocity oxy fuel (HVOF) and high velocity Air fuel (HVOF). *J. Thermal Spray Technol.* **8**(3), 351–356 (1999)
13. Vuoristo, P.M.: High velocity sprays boost hardmetal industrial coatings. *Met. Powder Rep.* **62**(3), 22–29 (2007)
14. Qi, X., Eigen, N., Aust, E., Gärtner, F., Klassen, T., Bormann, R.: Two-body abrasive wear of nano- and microcrystalline TiC-Ni-based thermal spray coatings. *Surf. Coat. Technol.* **200**(16–17), 5037–5047 (2006)
15. Bolelli, G., Colella, A., Lusvardi, L., Puddu, P., Rigon, R., Sassatelli, P., Testa, V.: Properties of HVOF-sprayed TiC-FeCrAl coatings. *Wear* **418**, 36–51 (2019)
16. Kiragi, V.R., Patnaik, A., Singh, T., Fekete, G.: Parametric optimization of erosive wear response of TiAlN-coated aluminium alloy using Taguchi method. *J. Mater. Eng. Perform.* **28**(2), 838–851 (2019)
17. Ghazanfari, H., Blais, C., Alamdari, H., Gariépy, M., Savoie, S., Schulz, R.: Characterization of dry-sliding wear of HVOF coatings made of Fe3Al powders reinforced with sub-micrometer TiC particles produced by combustion synthesis. *Surf. Coat. Technol.* **360**, 29–38 (2019)
18. García-Rodríguez, S., Torres, B., López, A.J., Otero, E., Rams, J.: Characterization and mechanical properties of stainless steel coatings deposited by HVOF on ZE41 magnesium alloy. *Surf. Coat. Technol.* **359**, 73–84 (2019)

19. Liu, X.B., Kang, J.J., Yue, W., Fu, Z.Q., Zhu, L.N., She, D.S., Liang, J., Wang, C.B.: Performance evaluation of HVOF sprayed WC-10Co4Cr coatings under slurry erosion. *Surf. Eng.* **1–10** (2019)
20. Krelling, A.P., Souza, M.M.D., Costa, C.E.D., Milan, J.C.G.: HVOF-sprayed coating over AISI 4140 steel for hard chromium replacement. *Mater. Res.* **21**(4) (2018)
21. Katranidis, V., Gu, S., Cox, D.C., Whiting, M.J., Kamnis, S.: FIB-SEM sectioning study of decarburization products in the microstructure of HVOF-sprayed WC-Co coatings. *J. Therm. Spray Technol.* **27**(5), 898–908 (2018)
22. Kiilakoski, J., Puranen, J., Heinonen, E., Koivuluoto, H., Vuoristo, P.: Characterization of powder-precursor HVOF-sprayed Al₂O₃-YSZ/ZrO₂ coatings. *J. Therm. Spray Technol.* **28**(1–2), 98–107 (2019)
23. Mohanty, D., Kar, S., Paul, S., Bandyopadhyay, P.P.: Carbon nanotube reinforced HVOF sprayed WC-Co coating. *Mater. Des.* **156**, 340–350 (2018)
24. Marques, A.S., de Costa, L.D.L., dos Santos, G.R., da Silva Rocha, A.: Wear study of hot forging punches coated with WC-CoCr and Cr₃C₂-NiCr through high-velocity oxygen fuel (HVOF) process. *Int. J. Adv. Manuf. Technol.* **100**(1–4), 3–11 (2019)
25. Xie, X., Chen, C., Xie, Y., Aubry, E., Ren, Z., Ji, G., Liao, H.: Comparative investigation of microstructure and properties of Ni-coated FeSiAl soft magnetic composite coatings produced by cold spraying and HVOF. *Surf. Coat. Technol.* **371**, 224–234 (2019)
26. Toma, F.L., Potthoff, A., Barbosa, M.: Microstructural characteristics and performances of Cr₂O₃ and Cr₂O₃-15% TiO₂ S-HVOF coatings obtained from water-based suspensions. *J. Therm. Spray Technol.* **27**(3), 344–357 (2018)
27. Koga, G.Y., Wolf, W., Schulz, R., Savoie, S., Bolfarini, C., Kiminami, C.S., Botta, W.J.: Corrosion and wear properties of FeCrMnCoSi HVOF coatings. *Surf. Coat. Technol.* **357**, 993–1003 (2019)
28. Das, P., Paul, S., Bandyopadhyay, P.P.: Tribological behaviour of HVOF sprayed diamond reinforced bronze coatings. *Diam. Relat. Mater.* **93**, 16–25 (2019)
29. de Souza Brandolt, C., de Fraga Malfatti, C., Vega, M.R.O., Hidalgo, G.E.N., Schroeder, R.M.: Determination of hydrogen trapping mechanisms by microprinting in Ni and Co coatings obtained by HVOF. *Surf. Coat. Technol.* **362**, 262–273 (2019)
30. Chen, C., Guo, Z., Li, S., Xiao, Y., Chai, B., Liu, J.: Microstructure and properties of WC-17Co cermets prepared using different processing routes. *Ceram. Int.* **45**(7), 9203–9210 (2019)
31. Singh, J., Kumar, S., Mohapatra, S.K.: Erosion wear performance of Ni-Cr-O and NiCrBSiFe-WC (Co) composite coatings deposited by HVOF technique. *Ind. Lubr. Tribol.* **71**(4), 610–619 (2019)
32. Liu, M.M., Hu, H.X., Zheng, Y.G., Wang, J.Q., Gan, Z.H., Qiu, S.: Effect of sol-gel sealing treatment loaded with different cerium salts on the corrosion resistance of Fe-based amorphous coating. *Surf. Coat. Technol.* **367**, 311–326 (2019)
33. Chen, Y., Shang, J., Liang, X., Wang, H., Zhou, Z.: Warm-particle peening assisted HVOF spraying: a new process to improve the coating performances. *Surf. Coat. Technol.* **367**, 135–147 (2019)
34. Giouse, J.B., White, K., Tromas, C.: Nanoindentation characterization of the surface mechanical properties of a 17-4PH stainless steel substrate treated with grit blasting and coated with a Cr₃C₂-NiCr coating. *Surf. Coat. Technol.* **368**, 119–125 (2019)
35. Qiao, L., Wu, Y., Hong, S., Cheng, J., Wei, Z.: Influence of the high-velocity oxygen-fuel spray parameters on the porosity and corrosion resistance of iron-based amorphous coatings. *Surf. Coat. Technol.* **366**, 296–302 (2019)
36. Azizpour, M.J., Tolouei-Rad, M.: Evaluation of residual stress in HVOF stellite-6 coatings using non-contact drilling. *Mater. Res. Express* **6**(6), 066577 (2019)
37. https://www.google.com/search?q=hvof+at+Metal+structure+in+Bridges.&source=lnms&tbn=isch&sa=X&ved=0ahUKEWjc4ankkIXIAhUYIbcAHTakA8sQ_AUIEigB&biw=1337&bih=640#imgrc=sZShP1wp54yqDM
38. https://www.google.com/search?q=hvof+at+Shafts&source=lnms&tbn=isch&sa=X&ved=0ahUKEwiZ0JGkkYXIAhUD7HMBHfBNCqEQ_AUIEygC&biw=1337&bih=640#imgrc=5axsdn3809Um8M

39. https://www.google.com/search?q=hvof+at+Repair+parts&source=lnms&tbm=isch&sa=X&ved=0ahUKEwi3re3UkYXIAhVS63MBHY_zCICQ_AUIEygC&biw=1337&bih=640#imgcr=dKRRHVU80oyjCM
40. https://www.google.com/search?tbm=isch&sa=1&ei=NYXXZL7Lofez7sP0tOF4Aw&q=hvof+at+Blades&oq=hvof+at+Blades&gs_l=img.3...82330.84668...85181...1.0...0.180.735.0j5...0...1...gws-wiz-img.GyOnWJHmk3A&ved=0ahUKEwjS6dj5kYXIAhUH73MBHdJpAcwQ4dUDCAc&uact=5#imgcr=oMD0Ep4Cn09UnM
41. https://www.google.com/search?tbm=isch&sa=1&ei=d5CYXZ7qBeraz7sPno6imAM&q=hvof+at+Sealing+in+compressors+&oq=hvof+at+Sealing+in+compressors+&gs_l=img.3...27659.37192...37669...0.0...1.300.2413.0j8j4j1...0...2j1...gws-wiz-img.tJOnyrht854&ved=0ahUKEwjegfWsk4XIAhVq7XMBHR6HCDMQ4dUDCAc&uact=5#imgcr=ubZ0rshnXe9ZkM
42. https://www.google.com/search?tbm=isch&sa=1&ei=SZSYXeKVBF_hz7sP8uG0mAg&q=Parts+in+textile+machines&oq=Parts+in+textile+machines&gs_l=img.3...126209.126980...127599...0.0...0.240.814.0j4j1...0...1...gws-wiz-img.0op_mV_XXf0&ved=0ahUKEwii3qDlloXIAhX_8HMBHfIwDYMQ4dUDCAc&uact=5#imgcr=G1J2-dTUMB6IYM
43. https://www.google.com/search?tbm=isch&sa=1&ei=SZSYXeKVBF_hz7sP8uG0mA&q=hvof+at+Used+at+Valves&oq=hvof+at+Used+at+Valves&gs_l=img.3...3501.3501...4491...0.0...0.143.143.0j1...0...2j1...gws-wiz-img.d3UPSCXCYc4&ved=0ahUKEwii3qDlloXIAhX_8HMBHfIwDYMQ4dUDCAc&uact=5#imgcr=VYQNQt2f7MpokM:

Chapter 9

An Investigation of Cutting Parameters and Its Effects on Surface Roughness in High-Speed Turning of 52100 Bearing Steel



Rahul Kshetri, Shivasheesh Kaushik, Vinay Sati, Kuldeep Panwar, and Ajay

Abstract An investigation was conducted to analyse the effect of machining parameters (cutting speed, depth of cut and feed rate), and there generated forces during turning operation cause the increasing temperature of tool. The effect of temperature and forces causes plastic deformation of tool whose effects can easily see on the surface finishing of workpiece. According to the review, data of turning has been selected and created a mathematical model in terms of temperature by selecting a previous literature data and developed a mathematical model by regression analysis. Temperature generation of all three zones and their overall effects of temperature on tool tip with different values of input parameters are also presented with the help of surface plots. The complete analysis is performed by selecting bearing steel (AISI 52100) as a workpiece with CBN tool.270.

Keywords Surface roughness · Machining · Tool tip temperature

R. Kshetri (✉)

Department of Industrial and Production Engineering, G. B. Pant University of Agriculture and Technology, Pantnagar, Uttarakhand, India
e-mail: rahulkshetricot@gmail.com

S. Kaushik

Department of Mechanical Engineering, Shivalik College of Engineering, Dehradun, Uttarakhand, India

V. Sati

Department of Mechanical and Automation Engineering, Delhi Technical Campus, Greater Nodia, India

K. Panwar

Department of Mechanical Engineering, Amrapali Institute of Technology, Haldwani, Uttarakhand, India

Ajay

Professor, Department of Industrial and Production Engineering, G. B. Pant University of Agriculture and Technology, Pantnagar, Uttarakhand, India

© Springer Nature Singapore Pte Ltd. 2020

I. Singh et al. (eds.), *Advances in Materials Engineering and Manufacturing Processes*, Lecture Notes on Multidisciplinary Industrial Engineering,

https://doi.org/10.1007/978-981-15-4331-9_9

Nomenclature

d	depth of cut (mm);
f	feed rate (mm/rev);
HRC	Rockwell hard ness;
t_1	uncut chip thickness;
t_2	cut chip thickness;
w	width of chip;
Ra	total roughness (μm);
r_ϵ	tool nose radius (mm);
VB	flank wear (mm);
V	cutting speed (m/min);
α	relief angle (degree);
γ	rake angle (degree);
λ	inclination angle (degree);
χ	major cutting edge angle (degree);
T_p	Temperature of primary zone ($^\circ\text{C}$);
T_s	Temperature of secondary zone ($^\circ\text{C}$);
T_i	Temperature of finished zone ($^\circ\text{C}$);
T	Tool tip temperature ($^\circ\text{C}$).

9.1 Introduction

There are so many dependent and independent parameters that act during orthogonal turning in the presented literature, and there is an analysis in which we are working over a variation of independent parameters and how does it affects their dependent parameter which causes tool wear and surface roughness of workpiece [1–3]. Independent parameters which we have to consider these are cutting speed (V), feed rate (f) and depth of cut (d), and their dependent parameters are the generation of temperature in different zones [4]. Temperature of all zones has been calculated by formulation in MATLAB software by Simulink mathematical blocks. Machining is performed in dry conditions. List of independent and dependent variables during machining operations is given in Table 9.1.

Table 9.1 Selected dependant and independant variables

Independent variables	Dependent variables
Starting materials (tool/workpiece)	Maximum temperature in cutting
Tool geometry	
Cutting velocity	Surface finish

In orthogonal machining, the occurrence of plastic deformation in tool causes burning temperature and combination of all forces [5, 6], and due to this effect [7, 8], tool wear and failure generally occur who is one of the responsible factors of increasing surface roughness of workpiece [9–13].

9.2 Heat Generation and Cutting Tool Temperature

Thermal analysis in orthogonal turning is based on three zones, and these three sources of heat generation zones during orthogonal cutting are given below.

9.2.1 Primary Zone (Shear Zone)

The major plastic deformation takes place in the shear zone, and this heat source is known as the primary heat source. A large fraction of this heat goes to the chip.

9.2.2 Secondary Zone (Friction Zone)

The sliding motion of the chip on the rake surface of the tool also generates heat, and this is the secondary heat source.

9.2.3 Tertiary Zone

Source of heat where the job rubs against the flank surface of the tool. But by this sharp tool, the contribution of this source to the heating phenomenon is insignificant, and generally, initial temperature (room temperature) is represented as a tertiary zone.

The contribution of this source to the heating phenomenon is insignificant all temperature zones which are clearly mentioned in Fig. 9.1. In which v denotes cutting velocity; v_c chip velocity; T_p temperature of primary zone; T_s secondary zone temperature; T_i tertiary zone temperature; t_1 uncut chip thickness; t_2 cut chip thickness; and w is width of chip.

Effect of temperature and other parameters influences on surface roughness has been calculated by taking data [14] which is shown in Table 9.2. Author had performed their experiment by selecting bearing steel (AISI 52100) as a work piece with CBN tool.

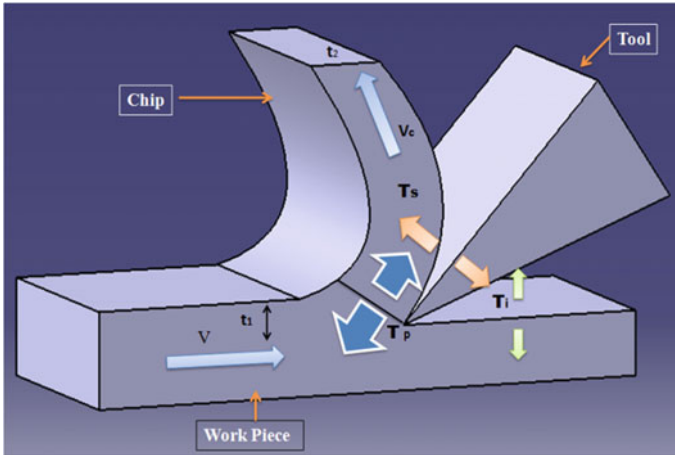


Fig. 9.1 Heat generation zones during machining

9.3 Specification of Tool

Rake angle $\gamma = -6^\circ$, clearance angle $\alpha = 6^\circ$, negative cutting edge inclination angle $\lambda = -6^\circ$ and cutting edge angle $\chi_r = 75$.

Mechanical and thermal properties of work piece (AISI 52100 bearing steel).

Density—7720 kg/m³, Thermal conductivity—19.00 W/m K, Specific heat capacity—468 J/Kg K.

Mathematical approach for finding temperature primary zone (shear zone) and secondary zone (friction zone).

Power = Rate of heat generation

$$W_p = F_s * V_{\text{shear}}$$

$$W_s = F * V_{\text{chip}}$$

For temperature measurement (known parameters of workpiece)

$$T_p = \frac{(1 - A)W_p}{\rho C V t_1 w} \dots \tag{9.1}$$

A = fraction of primary heat which goes to the workpiece, ρ = density of material (Kg/m³),

c = specific heat of the material (J/Kg °C), t_1 , w = uncut thickness (mm), width of cut (mm), respectively.

where, it has been found that A is a function of shear angle and a non-dimensional quantity, namely,

Table 9.2 Effects of input parameter on tool temperature and surface roughness

Cutting speed V (m/min)	Feed rate f (mm/rev)	Depth of cut, d (mm)	Tool tip temperature, T (°C)	Surface roughness, Ra (μm)
125	0.08	0.15	409.2	1.446667
125	0.08	0.3	420.11	1.513333
125	0.08	0.45	448.06	1.65
125	0.12	0.15	429.59	2.466667
125	0.12	0.3	455.89	2.38
125	0.12	0.45	490.09	2.553333
125	0.16	0.15	449.37	2.856667
125	0.16	0.3	487.22	2.816667
125	0.16	0.45	515	2.876667
176	0.08	0.15	428.306	0.903333
176	0.08	0.3	469.55	0.923333
176	0.08	0.45	493.74	0.973333
176	0.12	0.15	460.96	1.57
176	0.12	0.3	492.71	1.646667
176	0.12	0.45	517.84	1.643333
176	0.16	0.15	502.29	2.04
176	0.16	0.3	523.38	2.06
176	0.16	0.45	548.69	2.11
246	0.08	0.15	480	.67
246	0.08	0.3	517.67	0.723333
246	0.08	0.45	539.22	0.78
246	0.12	0.15	513.01	1.243333
246	0.12	0.3	540.69	1.336667
246	0.12	0.45	575.02	1.363333
246	0.16	0.15	540.33	1.616667
246	0.16	0.3	569.52	1.68
246	0.16	0.45	618.47	1.686667

$$\Omega = \frac{\rho C V t_1}{K}$$

K is the thermal conductivity (W/m °C) of material. For a wide range of work materials and machining conditions,

$$A = 0.15 \ln\left(\frac{25.5}{\Omega \tan(\emptyset)}\right) \dots \tag{9.2}$$

Table 9.3 Variation of temperature with input parameters (Feed, mm) as per L9 orthogonal array

Speed (m/min)	Feed (mm)	Depth of cut (mm)	Temperature (°C)
125	0.15	0.08	409.2
176	0.3	0.08	469.55
246	0.45	0.08	539.22
125	0.15	0.12	429.59
176	0.3	0.12	492.71
246	0.45	0.12	575.02
125	0.15	0.3	449.37
176	0.3	0.3	523.38
246	0.45	0.3	618.47

Table 9.4 Variation of temperature with input parameter (Depth of Cut, mm) as per L9 orthogonal array

Cutting speed (m/min)	Depth of cut (mm)	Feed (mm)	Temperature (°C)
125	0.08	0.15	409.2
176	0.12	0.15	460.96
246	0.16	0.15	540.33
125	0.08	0.3	420.11
176	0.12	0.3	492.71
246	0.16	0.3	575.02
125	0.08	0.45	448.06
176	0.12	0.45	517.84
246	0.12	0.45	575.02

Hence, if \emptyset is known or determined, A can be calculated using Eq. (9.2).

Secondary deformation zone along with the rake face of tool can be expressed as.

$$T_s = 1.13 \sqrt{\left(\frac{\Omega t_2}{(1 + \tan(\emptyset - \alpha) t_2)} \right) \left(\frac{w_s}{\rho C V w t_1} \right)}$$

now final temperature can be calculated by the addition of all ($T_p + T_s + T_o$), where T_o is the initial temperature of workpiece.

With the help of Simulink (MATLAB), all mathematical equations can be arranged like that, and after put down all input values, the output values can easily find out in the form of primary zone and secondary zone temperature which is clearly mentioned in Fig. 9.2.

Mathematical model of temperature generation is presented in Eq. (9.3)

$$T(^{\circ}\text{C}) = 245.9 + 0.516v + 195f + 811d - 2215d * d + 2.12v * d - 311f * d \dots \quad (9.3)$$

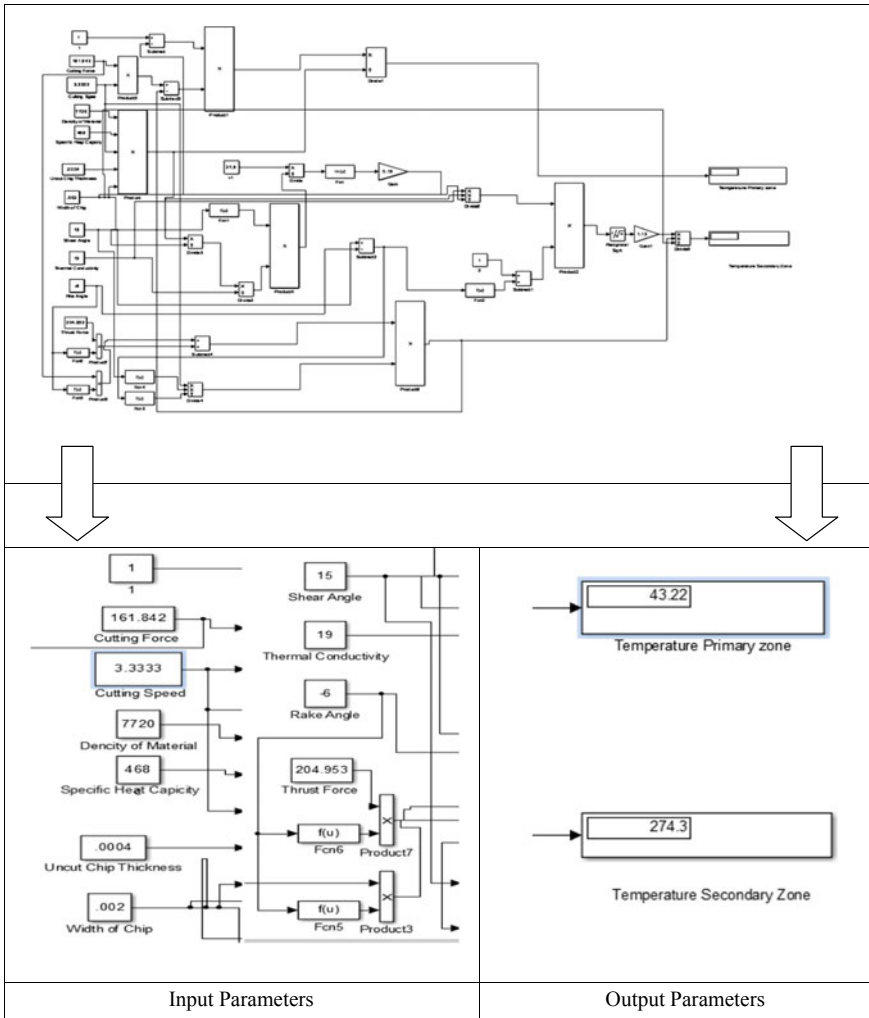


Fig. 9.2 Simulink block diagram

According to the surface plots shown in Fig. 9.3a–c influence, of cutting speed plays a vital role for the generation of temperature. Figure 9.4 also presents how cutting speeds (V), feed rate (f) and depth of cut (d) effects to tool tip temperature (T °C) of cutting tool.

Mathematical model of temperature is given in Eq. (9.4)

$$\begin{aligned}
 T(^{\circ}\text{C}) = & 309 + 0.38V - 59f + 291d + 0.00104V * V \\
 & + 116f * f - 0.05V * f + 1571f * d \dots
 \end{aligned}
 \tag{9.4}$$

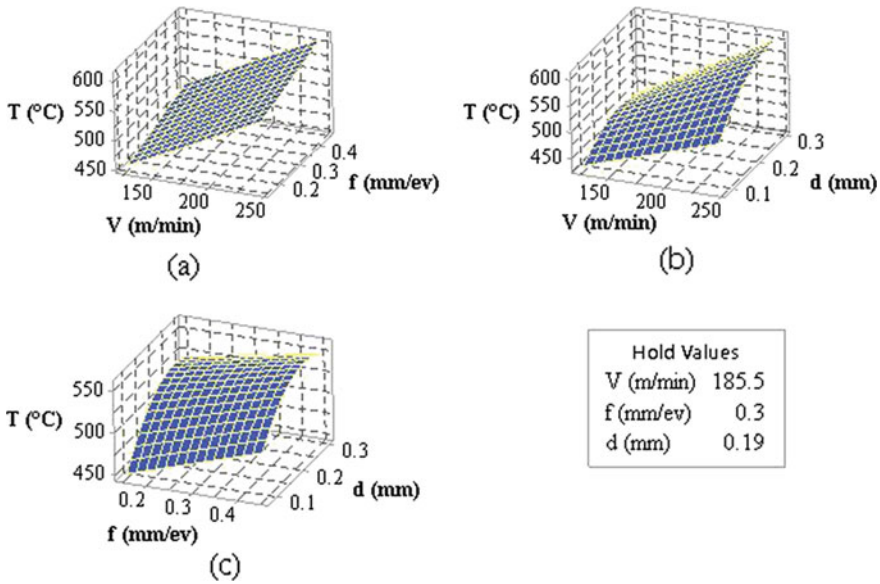


Fig. 9.3 Surface plots of temperature (Table 9.3)

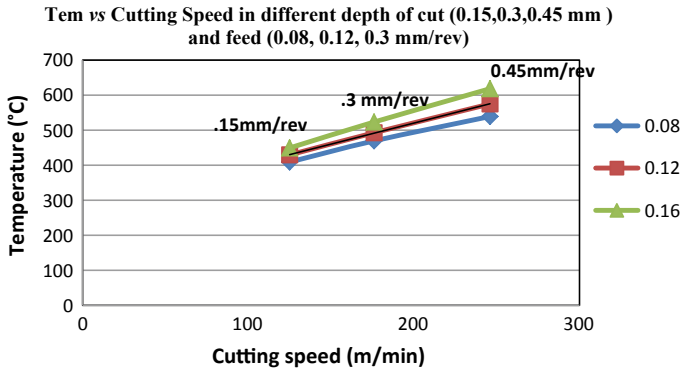


Fig. 9.4 Cutting speed versus temperature for a given feed and depth of cut

According to the surface plots of temperature generation of tool tip temperature increasing with increasing all dependent selecting parameters [speed, feed rate (mm/rev) and depth of cut (m)], but the influence of cutting speed (m/min) is shown in Fig. 9.5c, and main effect plots in Fig. 9.6 are higher as compared to all parameters because the generation of temperature in this case exceeding more than 540 °C whereas the appearance of temperature shows almost same effects in feed rate and depth of cut.

Mathematical model of surface roughness is given in Eq. (9.5)

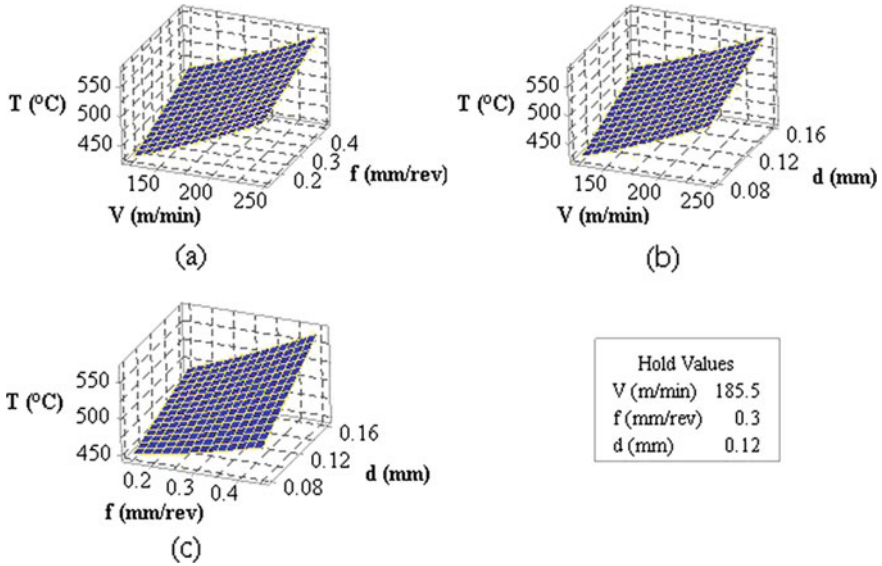


Fig. 9.5 Surface plots of temperature (Table 9.4)

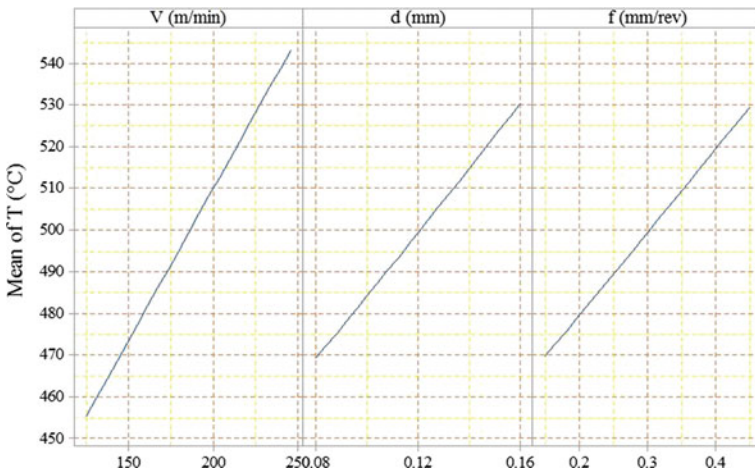


Fig. 9.6 Main effect plots of temperature

$$Ra(\mu m) = 1.841 - 0.03525V + 47.77d + 0.248f + 0.000084V * V - 106.9d * d + 0.72f * f - 0.03872V * d - 0.00000V * f - 3.10d * f \dots \quad (9.5)$$

According to surface and main effect plots, it has been very clear that, effects of feed rate and depth of cut during machining are the key causes of surface roughness

as soon as cutting speed is increasing, the generation of tool temperature increases but surface finishing increasing (roughness decreases) as shown in Figs. 9.7 and 9.8.

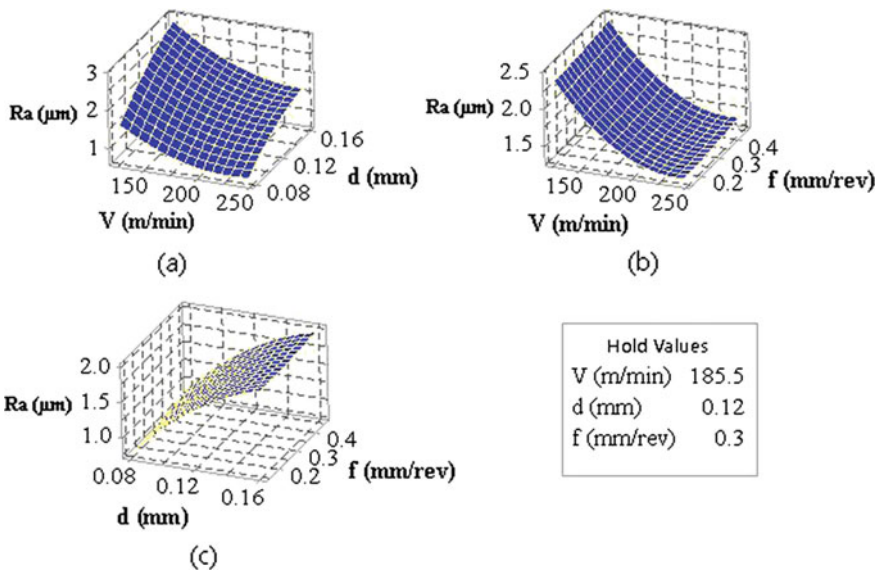


Fig. 9.7 Surface plots of roughness

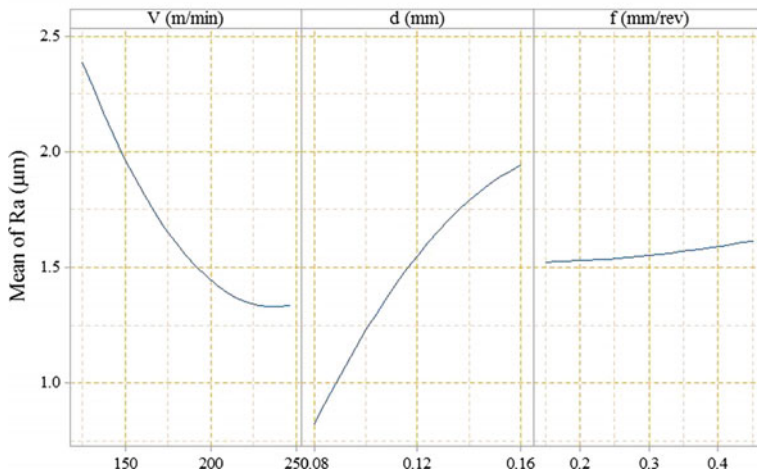


Fig. 9.8 Main effects of plot of surface roughness

9.4 Conclusions

The objective of our study was to define the effects of different parameters on bearing steel (AISI 52100) turning with a CBN tool, and during machining all the effects of different parameters on surface roughness followed by generated tool temperature. During machining, tool tip temperature increases with cutting speed and reaches its maximum point 544 °C when the cutting speed is 246 m/min, whereas the generation of temperature due to feed and depth of cut reaches up to 530 °C for both in its maximum value of feed and depth of cut. The effect of cutting speed is more influential parameter on surface roughness, for cutting speed 250 m/min and the value of surface roughness is nearby 1.25 μm, and that is, the result of best surface finish and the effects of increasing value of depth of cut show poor surface finish about 1.8 μm. Maximum value of surface roughness occurs if the cutting speed is minimum.

References

1. Mehta, M., et al.: Experimental analysis of the cutting forces in dry turning of EN8 steel. *Imp. J. Interdiscip. Res.* **2**(7) (2016)
2. Davim, J.P.: A note on the determination of optimal cutting conditions for surface finish obtained in turning using design of experiments. *J. Mater. Process. Technol.* **116**(2), 305–308 (2001)
3. Jadhav, J.S., Jadhav, B.R.: Experimental study of effect of cutting parameters on cutting force in turning process. *Int. J. Innov. Res. Adv. Eng.* **1**(6), 240–248 (2014)
4. Gosai, Mehul, Bhavsar, Sanket N.: Experimental study on temperature measurement in turning operation of hardened steel (EN36). *Procedia Technol.* **23**, 311–318 (2016)
5. Adesta, E.Y.T., Riza, M., Ali, M.Y.: Cutting force impact to tool life of CT5015 in high speed machining by applying negative rake angles. *Mater. Comput. Mech.* **117–119**, 633–638 (2012)
6. Bartarya, G., Choudhury, S.K.: Effect of cutting parameters on cutting force and surface roughness during finish hard turning AISI52100 grade steel. *Procedia CIRP* **1**, 651–656 (2012)
7. Das, S.R., Dhupal, D., Kumar, A.: Experimental study and modeling of surface roughness in turning of hardened AISI 4340 steel using coated carbide inserted. *Int. J. Autom. Eng.* **3**(1) (2013)
8. Lazoglu, I., et al.: Forces and temperatures in hard turning. *Mach. Sci. Technol.* **10**(2), 157–179 (2006)
9. Fnides, B., et al.: Application of response surface methodology for determining cutting force model in turning hardened AISI H11 hot work tool steel. *Sadhana* **36**(1), 109–123 (2011)
10. Ansari, M.S., Sharma, D., Nikam, S.: Study of cutting forces and surface roughness in turning of bronze filled polytetrafluoroethylene
11. Sahu, D.K., et al.: A review on effect of cutting parameters on cutting force in turning process
12. Kolahan, F., Manoochehri, M., Hosseini, A.: Application of Taguchi method and ANOVA analysis for simultaneous optimization of machining parameters and tool geometry in turning. *World Acad. Sci., Eng. Technol.* **74** (2011)
13. Islam, M.N., Boswell, B.: An investigation of surface finish in dry turning. In: *Proceedings of the World Congress on Engineering Vol I WCE 2011 London, UK, 6–8 July (2011)*
14. Khamel, S., Ouelaa, N., Bouacha, K.: Analysis and prediction of tool wear, surface roughness and cutting forces in hard turning with CBN tool. *J. Mech. Sci. Technol.* **26**(11), 3605–3616 (2012)

Chapter 10

Calculation for the Output of Solar Still of an Individual Hour



Mohd Zaheen Khan, Etkaf Hasan Khan, Nitesh Agarhari,
Mohd Atif Wahid, and I. Nawaz

Abstract A study has been done over the 9-h cycle for the solar still and calculates their output for an individual hour. The values of solar intensity, coefficient of heat transfer, ambient temperature, depth of water, and the coefficient of heat transfer through the walls of base and sides of the water basin are measured from the approximate method for each hour and later check their performance. In the previous methods, we required the graphical constructions and also constant coefficients of heat transfer assume but this thing is not required in this proposed method and observed the coefficients of heat transfer value for all the earlier time interval in the equations of heat balance is must. Actually, observed the two alternatives method of calculation is obtained evaporation rate for each an hour. From the energy balance equations, we compared the results from one which is found by mathematical solution. By using the energy balance equations, results which are calculated are different from the results obtained from the 9-h cycle of the approximate method and having the $\pm 1.5\%$ error. Water depth is 5–15 cms, coefficient of heat transfer in wind is 5–40 W/m² K and the coefficient of heat transfer through side and base walls is 0–3 W/m² K; these are variable ranges which taken for the analysis.

Keywords Solar intensity · Water depth · Productivity · Solar still

M. Z. Khan (✉) · I. Nawaz

Department of Mechanical Engineering, Jamia Millia Islamia, New Delhi, New Delhi 110025,
India

e-mail: zhnkhan4@gmail.com

E. H. Khan

Department of Mechanical and Automation Engineering, Delhi Technical Campus, Greater Noida
201306, India

N. Agarhari · M. A. Wahid

Centre for Advancement in Materials and Manufacturing Processes, Delhi Technical Campus,
Greater Noida 201306, India

© Springer Nature Singapore Pte Ltd. 2020

I. Singh et al. (eds.), *Advances in Materials Engineering and Manufacturing Processes*,
Lecture Notes on Multidisciplinary Industrial Engineering,

https://doi.org/10.1007/978-981-15-4331-9_10

10.1 Introduction

Figure 10.1 shows a “basin-type solar still.” Basin is insulated by proper insulating material, or it may be well-fitted on the ground. Dunkle [1] and Lof et al. [2] is defined as the fabrication features of the solar still. “Dunkle [1], Lof et al. [2], Morse and Read [3], and Cooper [4]” are defined as the energy balance of the distillation unit. Dunkle [1] reported and analyzed the heat balance and the heat and mass transfer relationship of a basin-type conventional distillation unit. A complete study was made by Lof et al. in 1961 in a solar still to investigate the heat and mass transfer, and also, he examined about the climatic variables and the different design parameters effects on the solar still performance. With the help of software, the results of energy balance equations were found. Different heat fluxes which are the function of the temperature of glass cover have described by Morse and Read [3]; hence, a graphical solution is obtained accordingly. From the mathematical solutions of energy balance equations, the different parameter effects like water depth and wind velocity are studied by Cooper [4] and also analyzed under different operations. In the detailed form, heat losses from the ground have studied and plotted the upward heat flux as the function of $(T_w - T_g)$ because the glass cover temperature is unknown.

For any given value of T_w and T_g , an experimental equation has been established to calculate the glass cover temperature and is given by Mullick and Sharma in 1991 [5]. By the given equation, the temperature of the glass cover has obtained, which allows correct calculation of evaporation and upward heat flux; from the proposed equations, the value of glass cover temperature allows exact calculations of instant value of evaporation and heat flux, when we compared it with the mathematical solution of energy balance for glass cover.

For the given climatic data, calculation of heat transfer is mainly doing for one hour of 24-h cycle for the solar still. The operation is unsteady, and the equations are

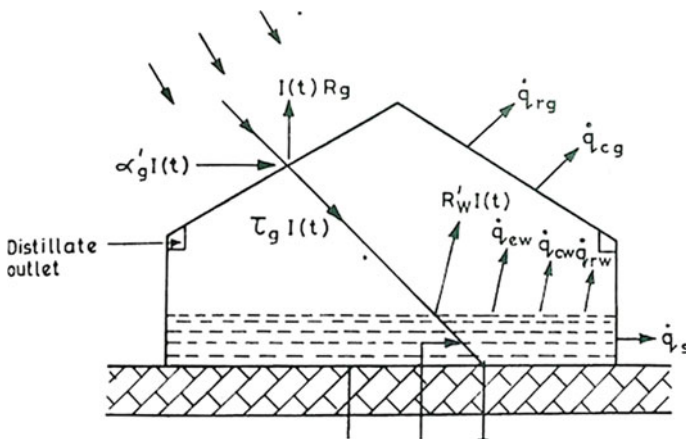


Fig. 10.1 Schematic diagram of heat flow in a conventional solar still

nonlinear in the heat balance equation of solar still. Hence, closed-form solutions are very hard to obtain. From mathematical results, it becomes easy to calculate the hourly output of solar still. For the studies, this method saves this time of the analysis.

To analyze the output hourly, Morse and Read in 1968 [3] gave a graphical solution. The accuracy of graphical method is less as compared to the geometrical constructions, and it also a very boring process. The closed-form solutions are given by Kumar in 1981 [6] by using harmonic series. Although for 24-h cycle, all the individual values of coefficient of heat transfer are assumed to be constant. Sharma and Mullick in 1991 [5] say this is an invalid assumption as the nonlinearly variations of this coefficient.

Calculating the output for 24-hour cycle, by a simple method, the objective of this work is achieved. First calculate the water temperature for each individual hour by the combination of energy balance equation for water keeping the coefficient of heat transfer constant for some particular interval of time. Investigation of the two different basic methods occurs. For simple calculation, we assume the coefficient of heat transfer which is constant for base and sides (U_b).

10.2 The Energy Balance

Appendix 1 contains all the individual coefficient of heat transfer, and thermal equation for basin-type distillation unit is mentioned. In this solar still, the energy balance on water is given by following,

$$\frac{c_w dT_w}{A_w dT} = \eta_o I - U_t(T_w - T_s) - U_b(T_w - T_a) \quad (10.1)$$

In glass and water neglecting the temperature gradients and assume no ventilation. Sharma and Mullick in 1991 [5] given the upward heat flow factor which is given by the following equation,

$$U_t = \left[\frac{1}{U_i} + \frac{1}{A_r \cdot U_o} \right]^{-1} \quad (10.2)$$

where

$$U_i = h_{cwg} + h_{ewg} + h_{rwg} \quad (10.3)$$

$$U_o = \frac{h_w(T_g - T_a)}{(T_g - T_s)} + h_{rgs} \quad (10.4)$$

$$A_r = \frac{A_g}{A_w} \quad (10.5)$$

“The overall upward heat flow factor, U_t , is based on $(T_w - T_s)$, since the sky temperature, T_s , has been used as the sink temperature”. After calculating the glass cover temperature, we determine the value of (U_t) which is calculated from the convective, radiative, and evaporative coefficient of heat transfer. By “quasi-steady heat balance on the glass cover,” the temperature of solar still glass cover is calculated and neglected thermal resistance and heat capacity of solar still glass cover; the energy balance on glass cover is calculated by following relations,

$$(T_g - T_a)A_r h_w + A_{rm} h_{rgs}(T_g - T_s) = (T_w - T_g)[h_{cwg} + h_{ewg} + h_{rwg}] \quad (10.6)$$

From Eqs. (10.12)–(10.17), the individual coefficient of heat transfer is mentioned in Appendix (1). From the solution of nonlinear Eq. (10.6), the glass cover temperature is obtained along with the property relation Eqs. (10.19) and (10.20). Sharma and Mullick in 1991 [5] gave the semi-empirical relation for calculating this,

$$T_g = \frac{\{(0.02612T_w^2 - 15.76T_w + 2392)T_w + A_r h_w T_a + A_r(0.048T_a - 9)T_s\}}{\{(0.02612T_w^2 - 15.76T_w + 2392) + A_r h_w + A_r(0.048T_a - 9)\}} \quad (10.7)$$

10.3 Hourly Output Calculation of Solar Still

The calculation of heat transfer of the distillation unit is performed for each one hour or less. After integrating Eq. (10.1), we obtained the water temperature for each one hour or less, and also, we assume the coefficient of heat transfer value that remains constant during the complete interval.

$$T_{wf} = \left[\frac{\eta_o \bar{I} + U_t T_s + U_b T_a}{(U_t + U_b)} \right] + \left[T_{wi} - \frac{\eta_o \bar{I} + U_t T_s + U_b T_a}{(U_t + U_b)} \right] \times \left[e^{-\left(\frac{U_t + U_b}{c_w}\right)} \right] \quad (10.8)$$

The initial and final temperatures of water are T_{wi} and T_{wf} . The average insolation and the ambient temperature for a particular interval are \bar{I} and T_a . For a low time interval, the coefficient of heat transfer is supposed to be constant. As the time interval decreases, the accuracy of Eq. (10.8) increases, and the error becomes zero when the time interval goes to zero. For the ease of calculations, the end of earlier time interval U_t is calculated.

If we know the temperature of glass cover, we easily calculate the evaporation rate as well as individual coefficient of heat transfer for any moment. From the solution of energy balance Eq. (10.6), we can obtain the glass cover temperature. For calculating, two different methods of glass cover temperature are checked in this current work.

These are accomplished by method (i): from Eq. (10.4) of semi-empirical (ii) by using the heat balance Eq. (10.6) which is given as,

$$T_g = \frac{U_i T_w + A_r h_w T_a + A_r h_{r_{gs}} T_s}{U_i + A_r h_w + A_r h_{r_{gs}}} \quad (10.9)$$

After the end of earlier time interval, we evaluate coefficient of heat transfer.

“The method (i) has the advantage in that it does not involve the assumption of constant heat transfer coefficients over the time interval. The method (ii) is more accurate for smaller time intervals and in fact converges with the numerical solution as the time interval tends to zero”. $U_t \cdot (T_w - T_s)$ is the upward flow of heat so for evaporation the utilized energy is given as,

$$\dot{q}_e'' = \frac{h_{ewg}}{U_i} U_t (T_w - T_s) \quad (10.10)$$

The distilled water mass is given by the following relation,

$$\dot{m}_w'' = \frac{\dot{q}_e''}{h_{fg}} \quad (10.11)$$

For any instant of time, the distilled water rate can calculate by the average values of the ambient and water temperature. At the start and the end of the previous time interval, a good method is to obtain the evaporation rate, although the output is nonlinear w.r.t. temperature. Now take the average of these two evaporation rates to signify evaporation rate for different time slots. It is confirmed that the second method is more accurate than the first one, so this method is continuing in this work.

By using the exact method, the calculations have been done for 24 h And comparing all the results with the mathematical solutions. In mathematical calculations, the time interval made is generally 30 s or maximum 1 min in the complete process. Data for the ambient temperature and the solar radiation especially in continuous function form to make the comparisons. In Appendix 2, the meteorological data for the June month is represented for the clear day by Fourier series. In Fig. 10.2, the day is shown.

10.4 Results Came Out in This Study and Further Made Discussion

In Figs. 10.3, 10.4 and 10.5, a comparison is made between the given method of the hourly production and the results of mathematical solutions over 24-h cycle of the heat balance Eqs. (10.1) and (10.6). By the method (i) and method (ii), the calculations have made with the temperature of glass cover. The coefficient of wind heat transfer, depth of water, and the coefficient of heat transfer from side and base

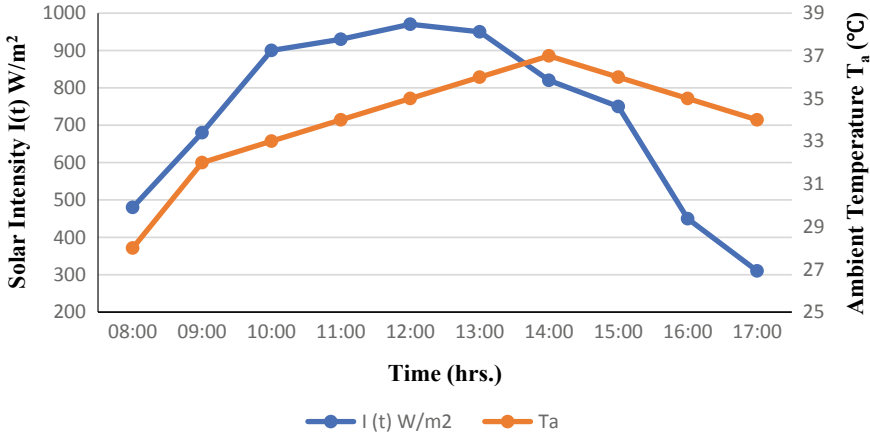
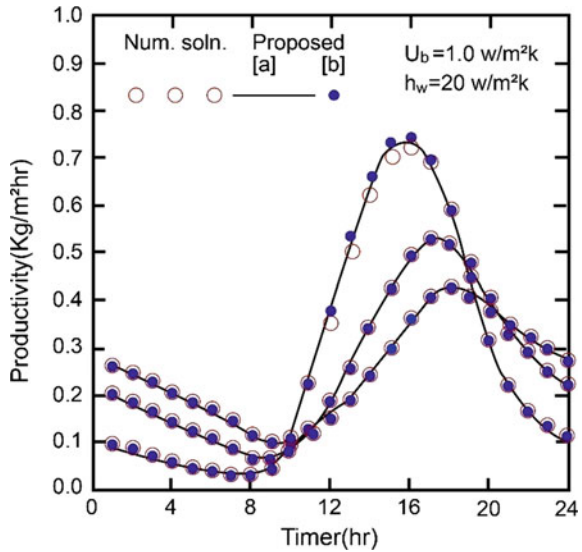


Fig. 10.2 Continuous function of solar intensity and ambient temperature

Fig. 10.3 Hourly productivity of water depth



walls; a comparison is made for different values of all these. Hence, the outcome of the given approach is approximately the same as mathematical solutions.

During the cloudy season, this method is also applicable; hence, we also confirmed by checking this. As shown in Fig. 10.6, assuming the solar radiation zero the calculations have been done between 11:00 am and 1:00 pm. In the same figure, the results for this change in solar intensity are also mentioned. From the given method, the results which are obtained are having a good agreement to the mathematical calculations using the glass temperature in both the methods.

Fig. 10.4 Hourly production of wind heat transfer coefficient

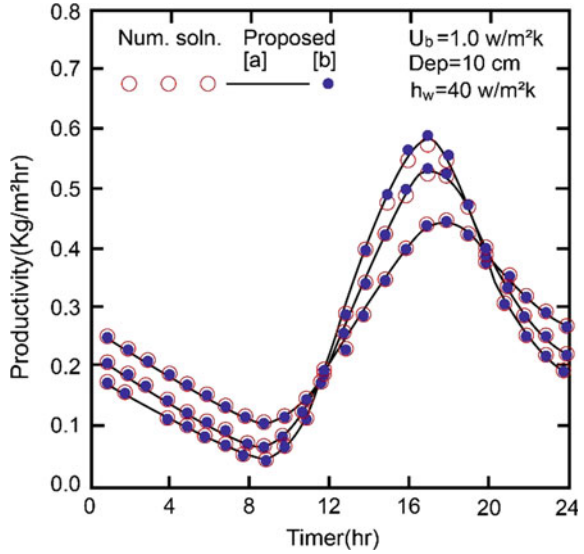
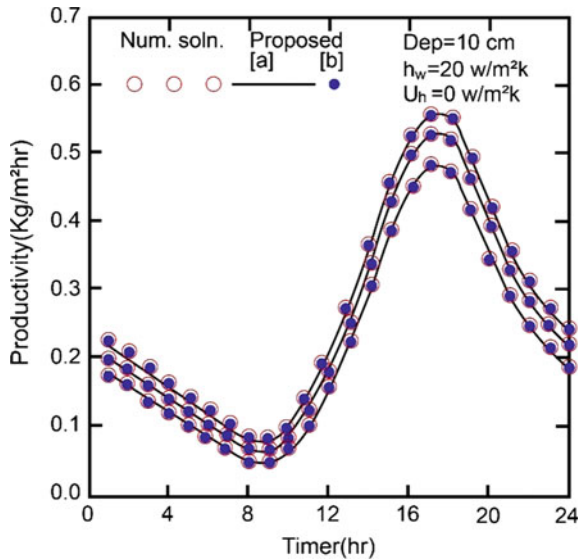


Fig. 10.5 Hourly productivity effect on U_b



5–15 cms is the depth of water, 5–40 W/m². K is the coefficient of wind heat transfer, and 0–3 W/m² K is the coefficient of heat transfer through base, and side walls are the basic parameters which is used in the present method to check their accuracy. To determine the glass cover temperature, a comparison of methods (i) and (ii) includes in the study. In Table 10.1, results are categorized. During the 24-h cycle computed the hourly values of maximum percentage, error is mentioned in

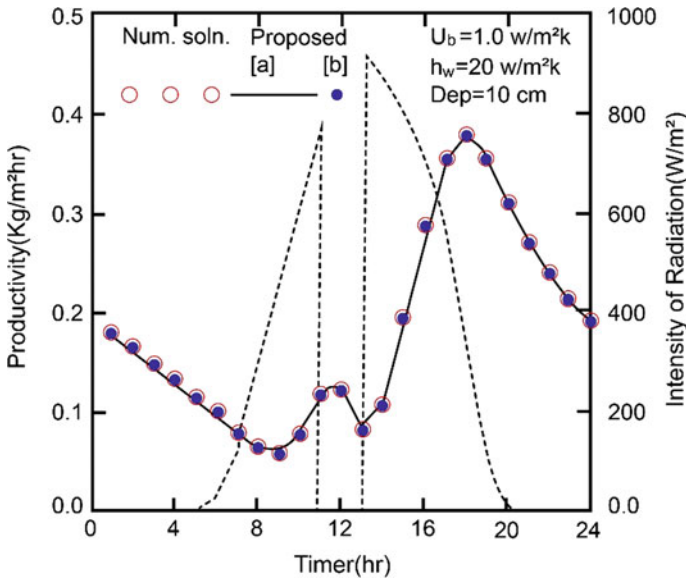


Fig. 10.6 Response of solar still during the changes in solar intensity

Table 10.1 The maximum percentage computation error in hourly output for the proposed method with a selected time interval size of one hour

Time interval = 1 h

Depth (cms)	h_w (W/m ² K)	$U_b = 0$		$U_b = 1$		$U_b = 3$	
		Max Per. error		Max Per. error		Max Per. error	
		<i>a</i>	<i>b</i>	<i>a</i>	<i>b</i>	<i>a</i>	<i>b</i>
5	5	4.75	4.78	4.54	4.63	3.96	4.2
	20	8.9	10.08	8.57	9.53	7.93	8.89
	40	11.4	12.46	11.2	12.19	10.74	11.81
10	5	1.96	1.85	2.0	1.85	2.01	4.2
	20	5.02	4.7	4.96	4.66	4.5	8.89
	40	6.21	6.91	6.01	6.87	5.98	11.81
15	5	1.208	1.115	1.23	1.222	1.28	1.12
	20	3.31	2.99	3.356	3.15	3.40	3.47
	40	4.57	5.45	4.581	5.698	4.54	6.18

Table 10.1. Different combinations of basic parameters are mentioned in Table 10.1 which shows the maximum computational error.

- (1) As h_w increases, the maximum error increases; but on increasing the depth of water, this maximum error decreases; the following are the reasons;

- (i) Increasing the h_w as the maximum error increases: U_t value does not change with temperature for the smaller values of h_w as it is mentioned in Sharma and Mullick [5]. Hence over a time interval, it is good to assume a constant U_t . From Eq. (10.8), the introduced error for the prediction of T_w is small. Over a time interval, larger variation in U_t for larger values of h_w which results in higher error prediction by Eq. (10.8) for U_t .
 - (ii) Increasing the depth of water as maximum error decreases: During the daytime, the water temperature is reduced at larger depth which results in the reduction of error prediction by Eq. (10.8) of T_w . Hence, effect of U_b on maximum error is small.
- (2) To determine the temperature of glass cover, it is necessary to compare both methods (i) and (ii); however, both the approach produced an acceptable result. When the water depth is small, then the temperature of water changes significantly; this is the main reason, that the heat balance Eq. (10.9) in the method (ii) at the end of earlier time interval using time interval gives the large computational error. As expected, the method (ii) gives better results for the large water depth, except the large value of h_w , so large change in water temperature as well as coefficient of heat transfer. For the 24-h cycle, the output from method (i) at lower water depth gives better results and method (ii) at larger depths gives better results.
- (3) In Table 10.2, the time interval effect on maximum computational error is mentioned. As the interval of time is halved, i.e., from 1 h to 30 min. the computational error percentage is also reduced.

The reason for this is to assume constant U_t in Eq. (10.8) during the time interval. Table 10.3 listed all the computational error over the time interval and all other

Table 10.2 The maximum percentage computation error in hourly output for the proposed method for different time interval sizes, for $U_b = 1.0 \text{ W/m}^2 \text{ K}$

$U_b = 1.0 \text{ W/m}^2 \text{ K}$							
Depth (cms)	h_w (W/m ² K)	Interval = 1 h		30 min		15 min	
		Max Per. error		Max Per. error		Max Per. error	
		<i>a</i>	<i>b</i>	<i>a</i>	<i>b</i>	<i>a</i>	<i>b</i>
5	5	4.54	4.63	2.4	2.42	1.25	1.26
	20	8.57	9.53	4.62	5.2	2.58	2.72
	40	11.2	12.19	6.0	6.2	3.21	3.37
10	5	2.0	1.85	1.05	0.97	0.6	0.47
	20	4.96	4.66	2.75	2.9	1.73	1.64
	40	6.0	6.87	3.51	4.93	2.3	2.77
15	5	1.23	1.22	0.64	0.527	0.24	0.25
	20	3.35	3.15	2.02	1.185	0.98	0.97
	40	4.581	5.696	2.7	3.44	1.77	1.92

Table 10.3 The maximum percentage computation error in an hourly and daily output over the entire range of variables covered for different time intervals sizes

	1 h		30 min		15 min		5 min	
	<i>a</i>	<i>b</i>	<i>a</i>	<i>b</i>	<i>a</i>	<i>b</i>	<i>a</i>	<i>b</i>
Max percentage error in hourly output	11.6	12.46	6.11	6.48	3.3	3.5	3.65	1.12
Max percentage error in daily output	1.04	1.52	0.48	0.46	0.4	0.2	0.37	0.05

variables. The daily output computation is also mentioned in Table 10.3 for maximum percentage error. The time interval of 15 min or less than that the method (ii) leads to small error. Hence, the outcome is that for a small change in time interval which leads to a small change in coefficient of heat transfer.

- (4) The error listed in Table 10.3 is greater than the average computational errors for a time interval, and this error is very less in the daily output.
- (5) Now the clear fact is that for determining the temperature of glass cover over a small-time interval, the method (ii) has a great advantage over the method (i). The coefficient of heat transfer before the end of earlier time for the method (ii) is also used for calculating the glass cover temperature. As the size of time interval approaches to zero, the method (ii) result converges with mathematical solutions. For one minute or less time interval size, these results are practically converging. The experimental equation is given by method (i) for temperature of glass cover; hence, it does not have any advantage over method (ii).

10.5 Conclusions

- (a) The hourly output of solar still by the given method does not require graphical construction to calculate the hourly output, and during the complete day, they also care about the variations of individual coefficient of heat transfer. In most of the cases, the given method can replace mathematical solutions and hence significantly decrease the computational effort. “In addition to verifying the response to a harmonic variation in solar radiation, the capability of the method to correctly predict the response to a sudden variation in solar radiation has been demonstrated.”
- (b) For large estimating of errors in side and bottom losses, vapor leakage, etc., this is a satisfactorily method. Although for the requirement of large accuracy, 30 min or less is the time interval needed, and also, the data of ambient temperature and solar intensity is needed at these time slots. For estimating, the glass cover temperature method (i) and method (ii) are quite well.

- (c) For smaller time intervals, the method (ii) has an advantage over the method (i) for calculating temperature of glass cover. For time slots of one or less minute, the results from the method (ii) meet with mathematical solutions.

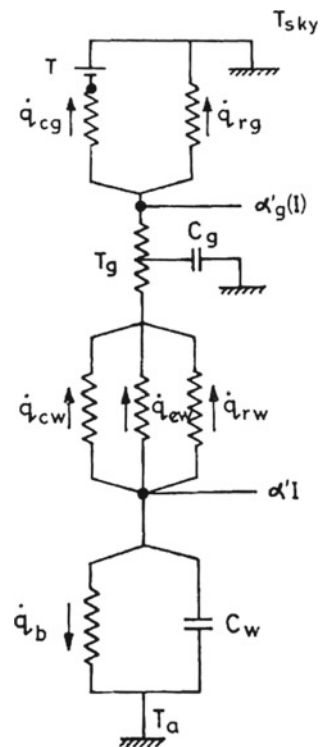
Appendix 1

In a basin-type solar still, the energy balance and the individual heat transfer coefficient

In Fig. 10.7, thermal circuit diagram for a basin-type solar still is mentioned, and it is because of Dunkle in 1961 [1]. The coefficient of heat transfer of radiation, convection, and evaporation is given by the following equation between the water and glass cover “(Duffie and Beckman [7], Dunkle [1], Kreith and Kreider [8]).”

$$h_{cwg} = 0.884 \left[T_w - T_g + \frac{(P_w - P_g)(T_w + 273)}{268.9 \times 10^3 - P_w} \right]^{1/3} \tag{10.12}$$

Fig. 10.7 Thermal circuit diagram of a solar still



$$h_{rwg} = 0.9\sigma \left[(T_w + 273)^2 + (T_g + 273)^2 \right] [T_w + T_g + 546] \quad (10.13)$$

$$h_{ewg} = 16.273 \times 10^{-3} h_{cw} \frac{P_w - P_g}{T_w - T_g} \quad (10.14)$$

between the atmosphere and the glass cover of solar still, the coefficient of radiative heat transfer is given by the following equation,

$$h_{rsg} = \varepsilon_{\text{eff}} \sigma \left[(T_g + 273)^2 + (T_s + 273)^2 \right] [T_s + T_g + 546] \quad (10.15)$$

coefficient of radiative heat transfer is located to surrounding temperature particularly for flat plate collectors which is given by,

$$h_{rga} = \varepsilon_{\text{eff}} \sigma \left[(T_g + 273)^2 + (T_s + 273)^2 \right] [T_s + T_g + 546] \frac{(T_g - T_s)}{(T_g - T_a)} \quad (10.16)$$

for small values of $(T_g - T_a)$; this method gives a large value of h_{rga} . The sink temperature is higher than the actual sink temperature means $(T_a > T_s)$; due to this, the large value of h_{rga} is obtained. The sink temperature is used in the earlier work of Sharma and Mullick [5] in 1991 as a sky temperature (T_s) for thermal network which is the lowest temperature. Among all calculations, this method gives the better results related to the present problem; during the nighttime, this approach gives better results under such conditions. The wind heat transfer coefficient is given by the following relation, because the sink temperature is used like ambient temperature,

$$h_{cgs} = h_w \frac{(T_g - T_a)}{(T_g - T_s)} \quad (10.17)$$

from the Swinbank 1963, the ambient temperature in this work is given by,

$$T_s = 0.0522 \times T_a^{1.5} \quad (10.18)$$

Equation formed for Latent heat and Water vapor Pressure as the temperature function.

Keenan and Keyes [9] in 1936 gives an empirical relation for partial pressure of water for the temperature limit of (10–150) °C is shown by the below equation,

$$p = 165960.72 \times 10^{-[X(a+bX+cX^3)]/[T(1+dX)]} \quad (10.19)$$

in the above equation, the constants a , b , c , d , and X having the values of 3.2437, 5.8682×10^{-3} , 1.1702×10^{-8} , 2.1878×10^{-3} , and 647.27, respectively; temperature (T) is measured in Kelvin.

In this current work for latent heat of vaporization, the relation given by Sharma and Mullick in 1991 [5] is as follows,

$$h_{fg} = 3044205.5 - 1679.1109T_w - 1.14258T_w^2 \quad (10.20)$$

Appendix 2

Calculate the data of solar insolation and ambient temperature

For 24-h period, for the mathematical solutions, it is easier to have ambient temperature and solar intensity in form of continuous functions. From the Fourier series with the 6 harmonics, the data of Delhi of June month for the clear day is shown by,

$$\begin{aligned} I = & 7.691 \cos(6w - 48.247r) + 18.089 \cos(5w - 183.169r) \\ & + 22.051 \cos(4w - 235.161r) + 18.917 \cos(3w - 4.459r) \\ & + 157.995 \cos(2w - 20.85r) \\ & + 475.165 \cos(w - 188.961r) + 306.055 \end{aligned} \quad (10.21)$$

$$\begin{aligned} T_a = & 0.157 \cos(6w - 25.516r) + 0.298 \cos(5w - 299.941r) \\ & + 0.3 \cos(4w - 155.915r) + 0.045 \cos(3w - 77.879r) \\ & + 1.107 \cos(2w - 351.466r) + 6.666 \cos(w - 230.105r) + 36.70 \end{aligned} \quad (10.22)$$

where radius (r) = $\pi/180$ and $w = 2\pi/(24 \times 3600)$.
so, continuous functions are shown in Fig. 10.2.

References

1. Dunkle, R.V.: Solar water distillation: the roof type still and a multiple effect distillation still. In: International Developments in Heat Transfer, Papers presented at the 1961 Int. Heat Transfer Conference, University of California, Part V, pp. 895–902 (1961)
2. Lof, G.O.G., Eibling, J.A., Bloemer, J.M.: Energy balances in solar distillers. *AICHE J.* **7**(4), 641–649 (1961)
3. Morse, R.N., Read, W.R.W.: A rational basis for the engineering development of a solar still. *Sol. Energy* **12**, 5–17 (1968)
4. Cooper, P.I.: Digital simulation of transient solar still processes. *Sol. Energy* **12**, 313–331 (1969)
5. Sharma, V.B., Mullick, S.C.: Estimation of heat transfer coefficients, the upward heat flow, and evaporation in a solar still. *ASME J. Solar Energy Eng.* **113**, 36–41 (1991)
6. Kumar, A.: Physics of the solar still. Ph.D. Thesis, Centre of Energy Studies, Indian Institute of Technology, Delhi (1981)
7. Duffie, J.A., Beckman, W.A.: *Solar Engineering of Thermal Process*, New York (1980)

8. Kreith, F., Kreider, J.F.: Principles of Solar Engineering. Hemisphere, New York (1978)
9. Keenan, J.H., Keyes, F.G.: In Thermodynamic Properties of Steam. Wiley, New York (1936)

Chapter 11

Effects of Secondary Parallel Cracks on the Fracture Parameters in a Rectangular Plate Under Static Loading



Gulfam Akhtar Ansari and Neeraj Bisht

Abstract In the present work, a numerical study using finite element is performed to investigate the effects of randomly oriented secondary parallel cracks on the fracture parameters in a rectangular plate under static loading. Crack is damaged that often occurs in members of structures and may cause the sudden serious failure of the structures. In the present study, two geometrical parameters, viz. crack offset distance and crack ratio, have been varied and their effect on stress intensity factor observed. Two types of effects were observed, viz. the shielding effect and the intensification effect. It was observed that there was mode mixity due to the presence of secondary cracks; it, however, was negligible.

Keywords Stress intensity factor · Shielding · Intensification

11.1 Introduction

Fracture mechanics involves the study of influence of existence of cracks on the properties and behaviour of the engineering components. Failure in aircraft industry, nuclear power generation plants, etc., would have a huge impact economically and more importantly in the form of human casualties. The analytical projections are produced by calculating fracture parameters in the crack region, such as stress intensity factor, J -Integral and T -stress, which are used to calculate the rate of crack growth. The stresses in the vicinity of a crack can be characterized by a single parameter called the stress intensity factor (SIF). The SIF can be determined analytically only for relatively simple components and loading. There are many distinct variables that influence the amount of component efficiency in service, such as the material's characteristics, the application of the load or stress system, the environment and its

G. A. Ansari (✉)
GBPUAT, Pantnagar, India
e-mail: gulfamakhtar786@gmail.com

N. Bisht
Department of Mechanical Engineering, GBPUAT, Pantnagar, India

© Springer Nature Singapore Pte Ltd. 2020
I. Singh et al. (eds.), *Advances in Materials Engineering and Manufacturing Processes*,
Lecture Notes on Multidisciplinary Industrial Engineering,
https://doi.org/10.1007/978-981-15-4331-9_11

maintenance. The causes of failure in engineering parts may be the absence of adequate design, unsuitable choice of material to be used, defects already present in the material during its production, incorrect maintenance of the component, crossing the boundaries presented by the component design, etc. Besides these factors, multiple site damage is one of the important reasons for the failure of the component. Due to the presence of two or more cracks, engineering component loses their strength and fails before reaching its theoretical value. Multiple site damage is one of the main factors for the failure of aircraft, riveted joints, turbine blades, pressure vessels and piping components.

Number of studies had been take place to find out the SIF of multi-crack interaction problems. McNeill et al. [1] determined the value of K_1 through the use of digital image correlation. Roux and Hild [2] calculated the SIF with 7% uncertainty. Ismail [3] found that for internal axial cracks under internal pressure, stress intensity factors along the crack front decreased when crack aspect ratio, a/t is increased. Lam and Phua [4] found that the interaction between micro-cracks could produce either an enhancement or a shielding effect on the stress intensity factor depending on the positions and orientations of the micro-cracks. Gope and Bisht [5] found that due to the presence of a neighbouring crack, the intensification effect was observed. It was seen that the amount of interaction between the cracks depends to a great extent upon the parameter Peng and Jones [6] found that the closer of the two cracks to boundary accelerates crack growth towards the boundary and decelerates linking of the cracks.

11.2 Methodology

Finite element analysis (FEA) is one of the most powerful and impressive numerical methods used in modern engineering practises. It utilized Ritz method of numerical analysis and minimization of variational calculus to obtain approximate solutions to vibration systems. In the present work, stress intensity factor has been calculated for a finite plate under plane stress condition, i.e. (stress along z -direction is zero) for different single and multiple orientations crack by ANSYS APDL software. Figure 11.1 shows the plane 82 element with 8-nodes.

- L 20 mm, length of the specimen
- W 10 mm, width of the specimen
- H varies from 1 to 10 mm, crack offset distance
- $A1$ right side crack tip of centre crack
- $B1$ left side crack tip of centre crack
- $A2$ right side crack tip of secondary crack
- $B2$ left side crack tip of secondary crack
- a_1 2 mm, length of the primary crack
- a_2 varies from 0.5 to 4 mm, length of the secondary crack

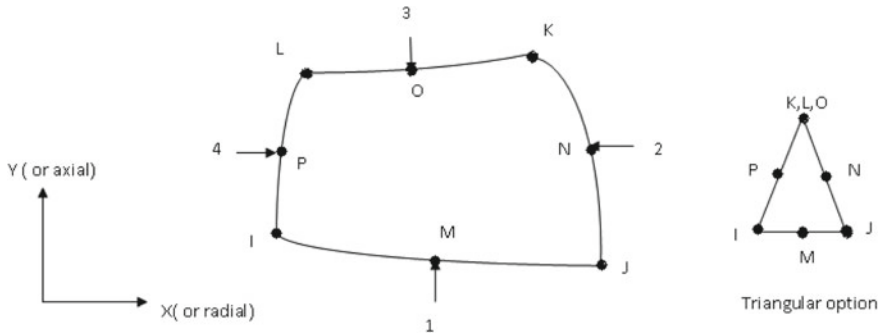


Fig. 11.1 Plane 82 element with 8-nodes

Specimen Geometry (A1)—Geometry A1 is shown in Fig. 11.2, and the effects of presence of secondary parallel cracks on fracture parameters are investigated. In this geometry, the secondary crack is parallel to the primary crack. Several effects can be observed with the use of geometry A1 such as effect of crack offset distance (H), crack ratios and number of parallel cracks (Tables 11.1 and 11.2).

Fig. 11.2 Specimen geometry A1

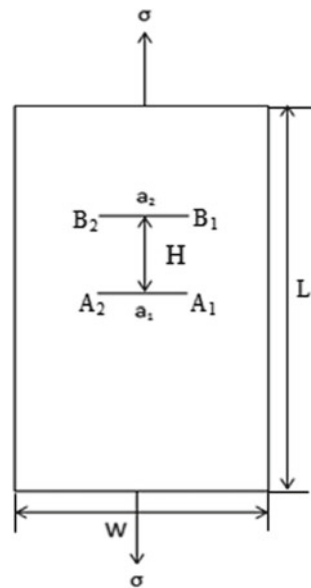


Table 11.1 Geometry specifications

Crack length (a_1) (mm)	Width (W) (mm)	Length (L) (mm)	Stress applied (σ) (Mpa)
2	10	20	500

Table 11.2 Material properties [7]

Material	Young's modulus (GPa)	Poisson's ratio	Density (kg/m ³)
Steel	210	0.3	8050

11.3 Results

11.3.1 Effect of Crack Offset Distance(H) on SIF

The effects of crack offset distance for the geometry having two parallel cracks are shown in Fig. 11.3. Figure 11.3 shows the effect of crack offset distance on normalized mode I and mode II SIF. It is observed that the presence of a secondary crack initiates mode mixity in the structure. The presence of a secondary crack shields the mode I for the primary crack. It is also observed that when the (H/L) ratio becomes lesser than 0.3, there is 25% reduction in the SIF of mode I. The mode II SIF that appears has no profound effect as the mode mixity ratio is below 0.15, and the mode I SIF is predominant. It can be seen that the presence of a secondary crack is beneficial when the multi-site damage occurs and an effective zone of ($H/L = 0.3$) can be seen beneficial in terms of reducing the mode I SIF by 25%.

It can also be seen that the stress intensity factor for mode I decreases when $H/L = 0.3$, and it reduces by about 25%. However as the cracks start moving further away, the mode I SIF starts increasing, and eventually, the crack interaction ceases to exist. This effect shows that as crack offset distance increases, the stress intensity factor for mode I also increases. Initially, the rate of increase of stress intensity factor is very high for mode I about 10% for $H/L = 0.05$ to $H/L = 0.3$; but as

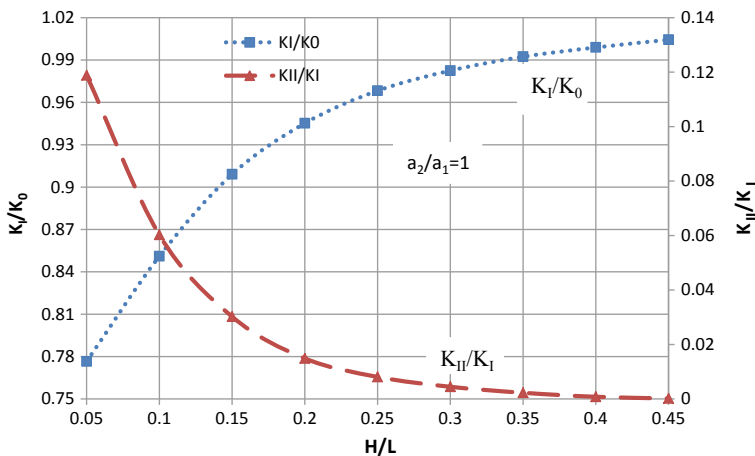


Fig. 11.3 Variation of K_I and K_{II} with crack offset distance (H) at crack tip A1 (crack parallel to center crack)

H/L increases beyond 0.3, the stress intensity factor for mode I will remain almost constant with only 0.2% change. From the above results, it can be concluded that the crack shielding phenomenon exists due to the existence of secondary crack of any size and configuration. With decrease in crack offset distance, the mode I SIF decreases and this will produce the shielding effect for the crack growth as the stress concentration near the crack tip is decreased.

11.3.2 Effect of Crack Ratio (a_2/a_1) on SIF When Cracks Are Parallel

The effect of crack ratio (a_2/a_1) on SIF behaviour of two parallel cracks is shown in Fig. 11.4 for $H = 3$ mm. It shows that the normalized mode I stress intensity factor (K_I/K_0) decreases as the crack ratio increases. The variation of mode II SIF (K_{II}/K_I) is just opposite to that of the mode I SIF. From the above results shown in Fig. 11.4, it is clearly shown that due to the increase in size of secondary crack the mode I stress intensity factor, i.e. K_I , will decrease. This effect in which the stress distribution near the crack tip decreases due to the presence of secondary crack is known as shielding effect.

It can be concluded that the length of the secondary crack has a major influence on the interaction. Smaller crack lengths give lesser interaction (shielding). However as the crack length increases, the shielding effect increases and reduces by about 30% when the secondary crack becomes twice that of primary crack. The mode mixity in this case, however, is negligible.

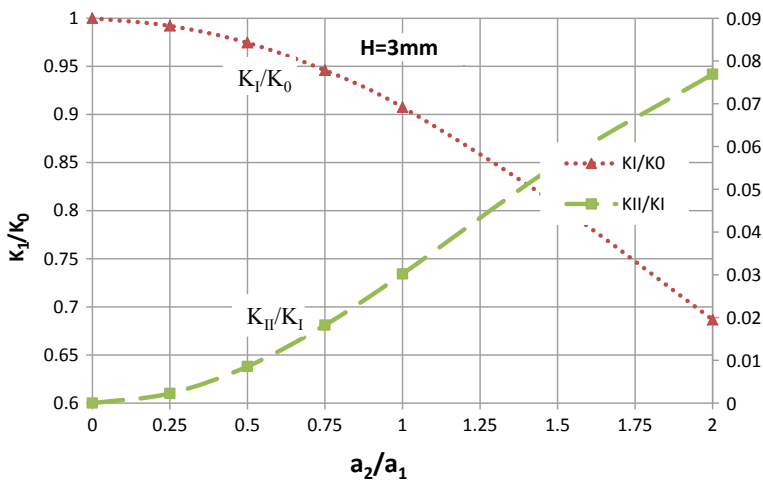


Fig. 11.4 Variation of K_I and K_{II} with crack ratio a_2/a_1 when cracks are parallel at crack tip A1

The variation in mode II SIF, i.e. (K_{II}/K_I) , is just opposite to that of the mode I SIF. On increasing the crack ratio (a_2/a_1) , the normalized mode II SIF (K_{II}/K_I) is increasing. But the value of mode II SIF is very less as compared to the mode I SIF; therefore, mode II SIF will not affect the overall shielding effect produced by the secondary crack to any greater extent.

11.4 Conclusion

For this case, it was observed that the mode I SIF was under shielding effect and it decreased to 75% of the value of K_I compared to that obtained for a single crack and as the cracks move away from each other K_I increases and approaches the value of K_I for single crack. It was also seen that mode II SIF that was absent for single crack is also developed when cracks are very close but it decreases and becomes zero as cracks move farther away. It was also observed that the length of the secondary crack has a major influence on the interaction. Smaller crack lengths give lesser interaction (shielding). However as the crack length increases, the shielding effect increases and reduces by about 30% when the secondary crack becomes twice that of primary crack. The mode mixity in this case, however, was negligible.

References

1. McNeill, S.R., Peters, W.H., Sutton, M.A.: Estimation of stress intensity factor by digital image correlation. *Eng. Fracture Mech.* **28**, 101–112 (1987)
2. Roux, S., Hild, F.: Stress intensity factor measurements from digital image correlation: post-processing and integrated approaches. *Int. J. Fracture* **140**, 141–151 (2006)
3. Ismail, A. E.: Solutions of stress intensity factor of multiple internal axial cracks in hollow cylinders. In: IOP Conference Series: Materials Science and Engineering, vol. 165, p. 012001. <https://doi.org/10.1088/1757-899x/165/1/012001> (2017)
4. Lam, K.Y., Phua, S.P.: Multiple crack interaction and its effects. *Eng. Fracture Mech.* **40**(3), 585–592 (1991)
5. Gope, P.C., Bisht, N.: Influence of crack offset distance on interaction of multiple cracks. *Theoretical Appl. Fracture Mech.* **70**, 19–29 (2015)
6. Peng, D., Jones, R.: The analysis of stress intensity factors in two interacting collinear asymmetric cracks in a finite plate. *Theoretical Appl. Fracture Mech.* **75**, 53–58 (2015)
7. Ayatollahi, M.R., Pavier, M.J., Smith, D.J.: Determination of T -stress from finite element analysis for mode I and mixed mode I/II loading. *Int. J. Fracture* **91**, 283–298 (1998)

Chapter 12

Flow Analysis of Flue Gas and Effectiveness of Regenerator Using Simulation in Packed Bed Regenerator



Kuldeep Rawat and Vivek Sachan

Abstract The main intent of this work is to examine the thermal characteristics of regenerator by the help of CFD analysis to find the special effects of pressure variation, velocity vector and variation of effectiveness of regenerator of fluid along with the regenerator distance end-to-end. These different factors affect the thermal regenerator such as regenerator distance end to end, diameter, heat storage capacity, gas flow direction; practical diameter and switching time are investigated by commercial Ansys Fluent software to understand the various thermal characteristics.

Keywords CFD · Regenerator · Ansys fluent · Skewness factor · Effectiveness of regenerator

12.1 Introduction

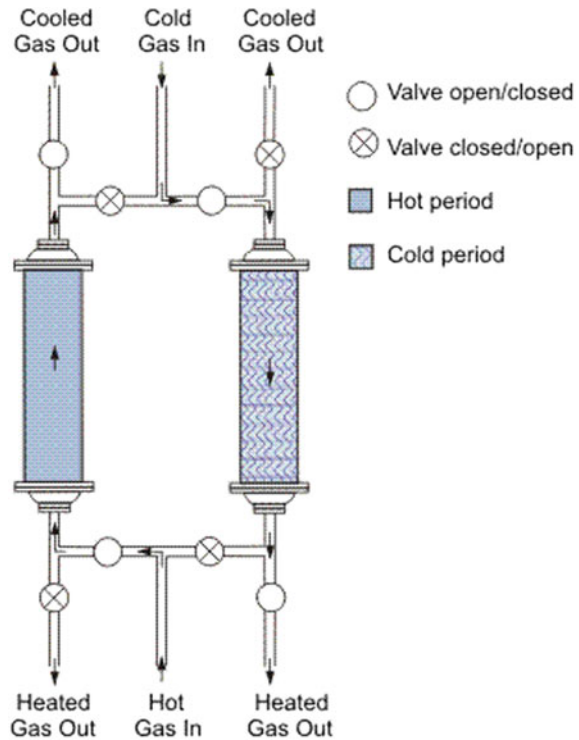
12.1.1 Heat Exchanger

This is a kind of device which is used to transfer the heat between two fluids. Heat exchanger classified according to the basis of heat transfer takes place between the fluids. Heat exchangers which have direct contact between two fluids are called direct contact heat exchanger, and heat exchangers which have no contact between fluids are called indirect contact heat exchanger.

K. Rawat (✉) · V. Sachan
Department of Mechanical Engineering, Shri Venkateshwara University, Gajraula,
Uttar Pradesh, India
e-mail: mail2kuldeeprawat@gmail.com

© Springer Nature Singapore Pte Ltd. 2020
I. Singh et al. (eds.), *Advances in Materials Engineering and Manufacturing Processes*,
Lecture Notes on Multidisciplinary Industrial Engineering,
https://doi.org/10.1007/978-981-15-4331-9_12

Fig. 12.1 Example of a figure caption



12.1.2 Heat Regenerators

Heat regenerator is a class of heat exchanger which is used to accumulate the heat by filled with a solids means (metals or ceramics) with changed shape and size which contain high volumetric heat ability. Thermal regenerator consists of two working phases: heating phase and cooling phase. In case of heating phase flue gases or warm gases worn out from regenerator in which warm gases heat transfer the energy to solid and warm gases at lower temperature exhausted from regenerator after the complete process of heating cycle start the cooling cycle in this cold air enter inside the regenerator to absorb the heat from solid and cold air get heated [1] (Fig. 12.1).

12.2 Review of Literature

A lot of researchers have done both theoretical and experimental work on packed bed regenerator. The following table summarises it as follows:

Researcher	Findings
Carman et al. [2]	Calculated the drag coefficient for flow through pebble bed regenerator for laminar flow
Ergun et al. [3]	Experimental work for turbulent flow through regenerator. Proposed a correlation for turbulent flow regimes
Mehta et al. [4]	Calculated pressure drop and drag coefficient in laminar flow through regenerator
Macdonald et al. [5]	Experimental work for regenerator having D/d_p ratio of more than 15

12.3 CFD Modeling

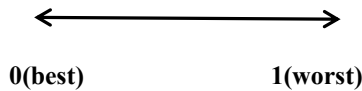
To solve the complex problem of heat transfer using the help of Computational Fluid Dynamics (CFD) analysis to analysis the pressure variation, velocity vector, temperature variation and effectiveness of regenerator with respect to the length of regenerator through the help of CFD.

In experimental arrangement we cannot evaluate the suitable result, however by using CFD analysis can be analyze precise result. In this paper, we consider the 5499 hexahedral cells and 6160 nodes for making a meshing to analysis the accurate result.

(a) Mesh Skewness

In CFD for getting accurate results, mesh quality is very important parameter. Skewness is the measuring factor for the quality of mesh.

$$\text{Skewness} = \frac{\text{Optimal cell size} - \text{Cell size}}{\text{Optimal cell size}}$$



Hexahedral cell skewness should not be exceeding 0.85, and in this geometry, the worst value of skewness factor is 0.41, and the average skewness factor in geometric model is 0.16. All details of skewness factors used for computational model are given in Table 12.1.

(b) Aspect Ratio

For measuring the quality of meshing aspect ratio, mesh should also be calculated. Aspect ratio is defined as the ratio of the longest side to the shortest side in the given cell. Preferably it should be 1. Table 12.2 shows the details of computational model of fixed-bed regenerator

Table 12.1 Skewness factor used for regenerator bed model geometries

Parameters	Computational model (steady-state model)
Total number of elements	5499
Element type	Hexahedral
Max. skewness	0.41
Min. skewness	$2.5 * 10^{-06}$
Average skewness	0.16

Table 12.2 Aspect ratio used for regenerator bed modeled geometries

Parameters	Phy-1 (steady-state model)
Total number of elements	5499
Element type	Hexahedral
Max. skewness	0.41
Min. skewness	$2.5 * 10^{-0}$
Average skewness	0.16

12.4 Governing Equations

The flow-through regenerator is governed by following governing equation

Panwar and Murthy et al. [1]

Continuity Equation:

$$\Delta (\epsilon \rho \vec{v}) = 0$$

Momentum Equation:

$$\frac{\partial}{\partial t} (\epsilon \rho \vec{v}) + \nabla \cdot (\epsilon \rho v \vec{v}) = -\epsilon \nabla p + \nabla \cdot (\epsilon \vec{\tau}) + \epsilon \vec{B} f - \left(\frac{\mu}{\alpha} + \frac{C_2 \rho}{2} |\vec{v}| \right) \vec{v}$$

$$\left\{ \begin{array}{l} \text{Rate change} \\ \text{of momentum} \\ \text{per unit} \\ \text{volume} \end{array} \right\} + \left\{ \begin{array}{l} \text{Net rate of} \\ \text{momentum} \\ \text{flux due to} \\ \text{convection} \end{array} \right\} = \left\{ \begin{array}{l} \text{Pressure} \\ \text{force} \end{array} \right\} + \left\{ \begin{array}{l} \text{Viscous} \\ \text{force} \end{array} \right\} + \{ \text{Body force} \} - \left\{ \begin{array}{l} \text{viscous \& inertial} \\ \text{drag force by} \\ \text{the pore wall} \\ \text{on the fluid} \end{array} \right\}$$

The viscous loss coefficients as well as the inertial loss coefficients of the porous region are calculated by the following equations:

$$\alpha = \frac{(d_p^2 \times \varepsilon^3)}{203 \times (1 - \varepsilon)^2}$$

where

- d_p Diameter of solid particle (alumina)
- ε Porosity of the regenerator bed
- α Permeability.

Viscous loss coefficient into each component direction = $1/\alpha$

$$C_2 = \frac{3.9(1 - \varepsilon)}{d_p \times \varepsilon^3}$$

where

- d_p Diameter of solid particle (alumina)
- ε Porosity of the regenerator bed
- C_2 Inertial loss coefficient.

12.5 Result and Discussion

The simulated results for creeping flow of flue gases and air are in both heating and cooling phases of computational model of a fixed-bed regenerator. Afterwards, the meshing of computational domain is divided into 5499 hexahedral cells with 6160 nodes. To capture the effects of heat and fluid flows in 3D, Ansys fluent software was used and results were studied once the conversation criteria was reached. After the CFD, simulation results have been presented in this paper as follows.

- Pressure contour variation of flue gases along the regenerator height.
- Velocity vector variation along regenerator length.
- Effect of regenerator height on its effectiveness (Figs. 12.2, 12.3, 12.4, 12.5 and 12.6).

The comparative study of effectiveness of regenerator and exit flue gas temperature indicate that as increases the regenerator length with respect that decreases the exit flue gas temperature as shown in Fig. 12.8 this happen due to flue gas flows through the regenerator and heat from flue gas is transferred to words the solids so that temperature of exit flue gas decreases (Fig. 12.7).

It means for higher length, the thermal mean residence time of flue gas increases which means the flue gas remains in the regenerator for longer period; hence, more

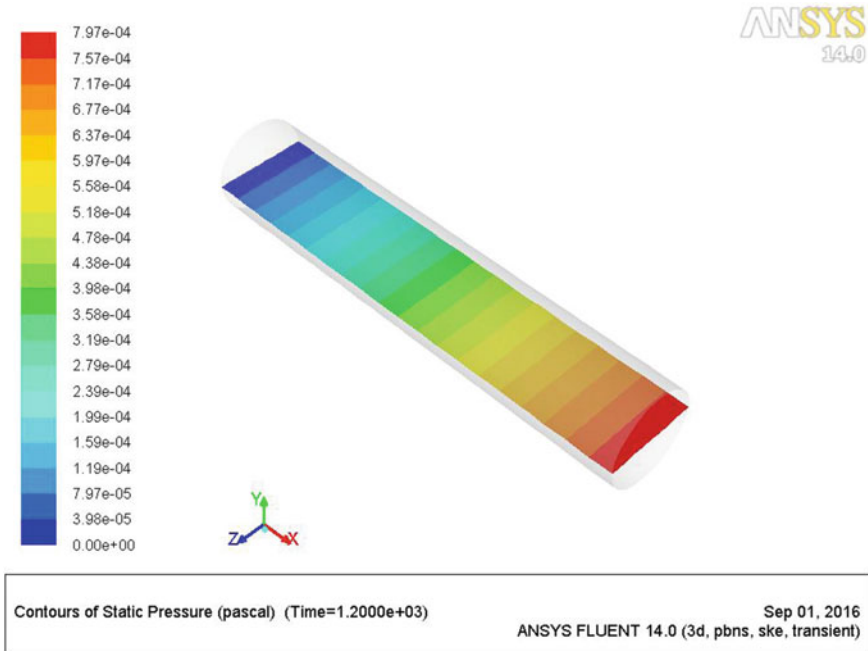


Fig. 12.2 Pressure drop along with regenerator length for cooling cycle at $t = 2$ min

heat is transferred towards solids. When decrease in exit flue gas temperature than effectiveness of fixed-bed regenerator increases which is shown in Fig. 12.8.

But it is seen from the same Fig. 12.7 that after a certain length (0.62 m), the thermal efficiency of the regenerator remains constant, i.e. it does not increase with regenerator length. Hence, it is very important for the designer to have an optimal regenerator length such that the thermal efficiency is highest and the same time material cost is also low or optimum.

12.6 Conclusion

A thermal characteristic of regenerator was studied with the effect of different factors and also studied such as regenerator height, D/d_p ratio, and porosity. By using Ansys fluent analysis, the different factors such as pressure variation, velocity vector, effectiveness of regenerator, and exit flue gases were studied designed regenerator with different lengths.

Regenerator was designed in Fluent, and simulations were done to study the pressure variation along with regenerator length, exit flue gas temperature, velocity vector, and effectiveness of regenerator was calculated. As shown in relation between exit flue gas temperature and designed bed height for longer regenerator exit flue gas

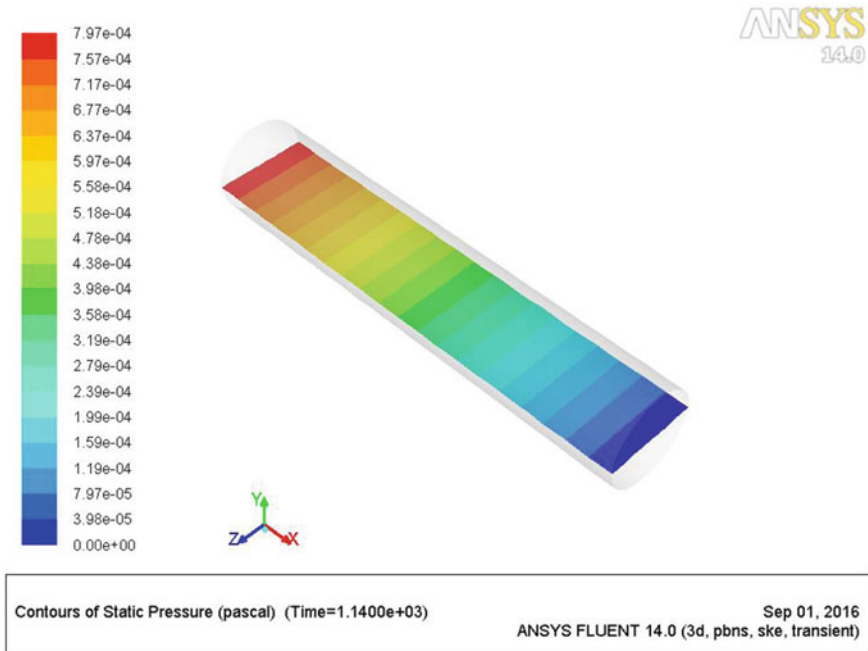


Fig. 12.3 Pressure drop along with regenerator length for heating cycle at $t = 19$ min

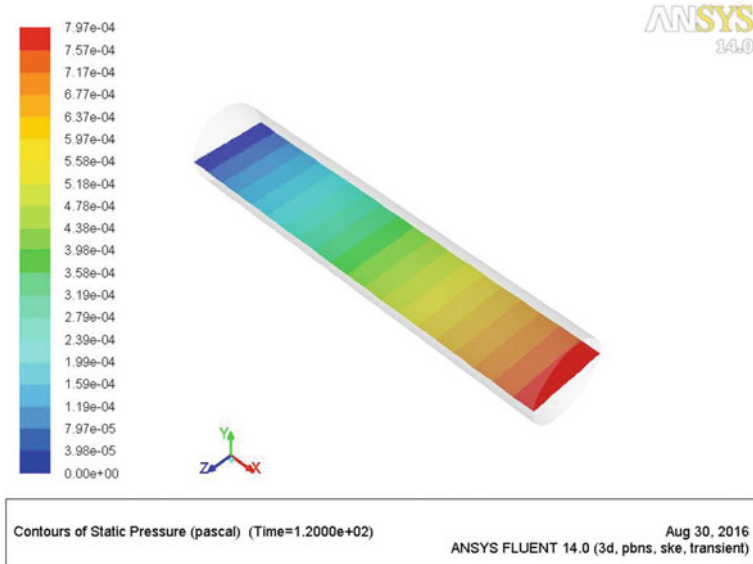


Fig. 12.4 Pressure drop along with regenerator length for cooling cycle at $t = 20$ min

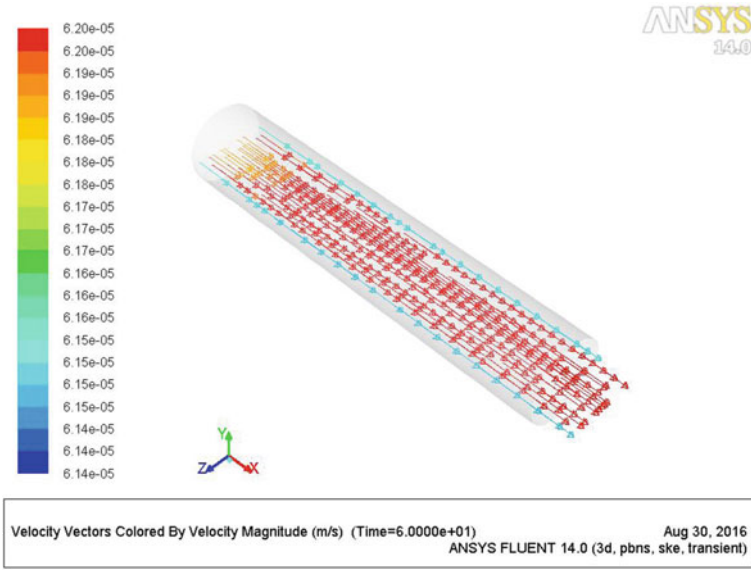


Fig. 12.5 Velocity vector along with regenerator length at $t = 1$ min

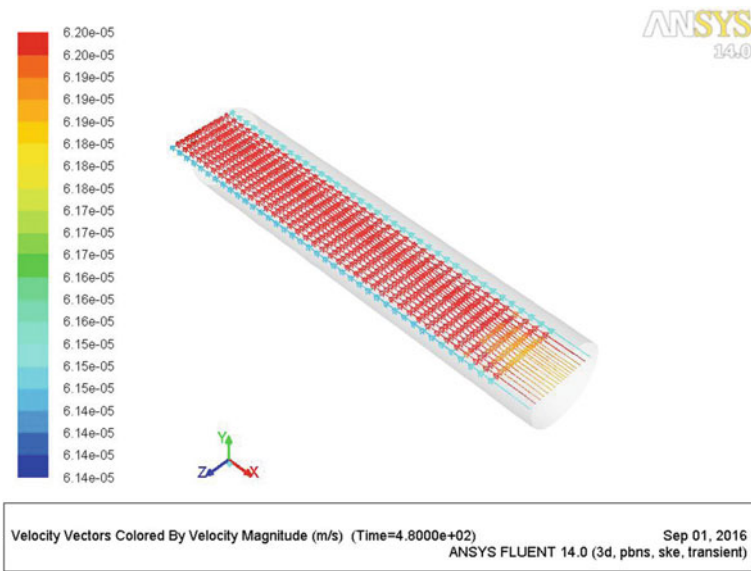


Fig. 12.6 Velocity vector along with regenerator length at $t = 8$ min

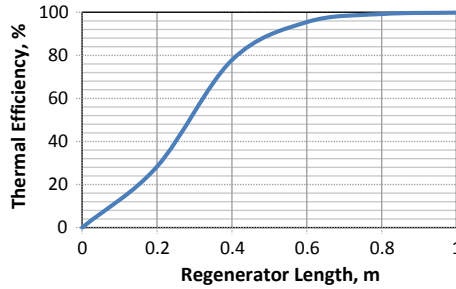


Fig. 12.7 Variation of effectiveness of regenerator with regenerator length

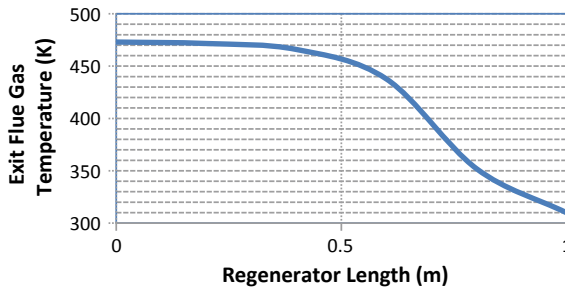


Fig. 12.8 Variation of exit flue gas temperature with regenerator length

temperature found low and effectiveness of regenerator varying from 20 to 90% with respect to varies the height of regenerator from 0.2 to 1 m.

References

1. Panwar, K., Murthy, D.S.: Analysis of thermal characteristics of the ball packed thermal regenerator. *Procedia Eng.* **127**, 1118–1125 (2015)
2. Carman, P.C.: Fluid flow through granular beds. *Trans. Inst. Chem. Eng.* **15**, 150–166 (1937)
3. Ergun, S.: Fluid flow through packed columns. *Chem. Eng. Prog.* **48**, 89–94 (1952)
4. Mehta, D., Hawley, M.C.: Wall effect in packed columns. *Indus. Eng. Chem. Process Design Dev.* **8**, 280–282 (1969)
5. Mac Donald, T. F., El-Sayer, M. S., Mow, K., Dullen, F. A. L.: Flowthrough porous media: The Ergun equation revisited. *Indus. Eng. Chem. Fundamentals.* **18**, 199–208 (1979)